DYNAMICS OF SATURN'S POLAR REGIONS

DISSERTATION

Submitted for the degree of Doctor in Philosophy by

ARRATE ANTUÑANO MARTÍN

Supervisors:

Dr. Agustín Sánchez Lavega

Dr. Teresa del Río Gaztelurrutia

Grupo de Ciencias Planetarias
Departamento de Física Aplicada I
Escuela de Ingeniería de Bilbao

UNIVERSIDAD DEL PAÍS VASCO
EUSKAL HERRIKO UNIBERTSITATEA

May 2017

A mi madre.

Agradecimientos

Después de cuatro años de risas, estrés y alegrías, se cierra una bonita etapa como estudiante para dar lugar a una nueva y emocionante etapa de la vida: la de investigadora (que bien suena). Son muchas las personas que me han apoyado y ayudado durante estos cuatro años, en los que a veces se han tenido que cargar de paciencia, y que sin ellas esta tesis no habría podido salir adelante. Son a todas ellas a las que quiero dedicarles unas palabras de agradecimiento.

Me gustaría empezar dando las gracias a la razón de mi existencia, mi padres, quienes siempre han antepuesto la felicidad de mi hermano y mía a la de ellos. Gracias aita y ama por haber estado siempre ahí, apoyándome en cada decisión que he tomado y mostrándome que con esfuerzo, ilusión y paciencia se pueden conseguir grandes cosas en la vida, esta tesis es un buen ejemplo. Por supuesto, no me puedo olvidar de mi hermano, que a pesar de chincharle todo el tiempo y de ser tan diferentes, hemos disfrutado de muy buenos momentos juntos. Gracias Unai por compartir tus aficiones conmigo! Nos vemos en el agua!

También me gustaría mostrarles mi más sincero agradecimiento a mis directores de tesis Dr. Agustín Sánchez Lavega y Dra. Teresa del Río Gaztelurrutia, quienes me han dado la oportunidad de cumplir uno de mis sueños y me han hecho crecer no solo como científica, sino también como persona. Gracias por haber compartido un poco de vuestro gran conocimiento conmigo y por haberme guiado en esta aventura de la tesis, presionándome cuando hacía falta, tranquilizándome cuando los nervios podían conmigo y animándome siempre a seguir adelante. Teresa, después de muchas llamadas, emails y horas reunidas (y conversaciones sobre nuestros gatitos), por fin puedo entregarte tu primera tesis como directora! Espero que te sigan quedando ánimos para seguir dirigiendo tesises. Gracias de corazón a los dos.

Agradezco al Ministerio de Economía y Competitividad el haberme otorgado una ayuda pre-doctoral para la formación de doctores (FPI) y la ayuda a la movilidad predoctoral para la realizacin de estancias breves en centros de I+D y, cómo no, al Dr. Read y todo su grupo "Geophysical Fluid Dynamics" de la Univsersidad de Oxford por haberme dado la oportunidad de formar parte de él durante casi cuatro meses en los que he podido aprender muchísimo.

Por supuesto, no puedo olvidarme de todo el departamento de Física Apliaca I, que me han hecho sentirme como una más desde el principio. En especial, de mis compañeras de despacho Itsaso y Macarena, con quienes he tenido la suerte de com-

partir muy buenos momentos y muchas risas en estos últimos años, que habría hecho sin vosotras! De Itziar, Naiara, Santi y los chicos del despacho de al lado, Iñaki, Hao, Jon y Ander, compañeros de tertulia a la hora de comer, siempre dispuestos a echarme un cable en lo que hiciese falta, gracias compañeros de "tuppers"! Y del grupo del café de la tarde y todo el Grupo de Ciencias Planetarias.

Quisiera agradecer también a Laura y Amaia, mis amigas de la infancia, quienes me llevan soportando prácticamente toda la vida y las que me han demostrado continuamente que puedo contar con ellas para cualquier cosa, bien sea ir de paseo a despejarnos y comer unos jumpers o llorar conmigo en los momentos más dificiles o bonitos de mi vida. GRACIAS chicas!

Y por supuesto, no podía olvidarme de la persona que más me ha ayudado y apoyado en estos últimos años, esa persona que ha estado a mi lado en todo momento aguantando mis nervios, estrés y altibajos y que ha sabido escucharme y animarme perfectamente, mi marido. Gracias, gracias y mil gracias Julen.

Contents

List of Tables

List of Figures

Summary

Polar regions present singular behavior and dynamics related to the rotation rate of the planet, specially important in fast rotating planets. In particular, Saturn's polar regions are characterized by a wide variety of cloud morphologies, some of them not observed in other planets, such as the remarkable hexagonal feature located at the north polar region at 75.8° planetocentric latitude, a feature that has survived at least since 1981 and that has no equivalent at the south polar region of the planet. Other noteworthy features of Saturn's polar regions are the presence of long-lived polar vortices at both poles or the fields of compact cloud present in both polar regions.

In this dissertation, we study the dynamics of Saturn's polar regions from $\sim 60°$ to 90° latitude at cloud level, focusing on the comparison of both polar regions, the Hexagon and the relationship between the observed cloud morphology and the local and general dynamics of the area, by analyzing multi-wavelength high-resolution images captured by the Cassini ISS cameras between October 2006 and September 2014, at visible wavelengths from the the violet ($\sim$ 400 nm) to the near-infrared ($\sim 1,000$ nm). These data allow the study of the cloud morphology and horizontal motions at the highest resolution images thus far for Saturn's southern summer, northern spring and beginning of northern summer. In addition, we analyze different possible interpretations of the origin of the Hexagon.

In order to analyze the dynamics of these regions, we measure horizontal winds on continuum band (CB2) images, which sense the top of the ammonia cloud at around 600 mbar pressure, and we compute averaged zonal and meridional velocity maps together with zonal velocity profiles. Furthermore, latitude-longitude averaged relative vorticity maps and profiles of vorticity gradients are retrieved from the measured horizontal winds. Finally, using the obtained horizontal wind field and the thermal structure retrieved by Fletcher (2015) from CIRS data, we compute zonally averaged Ertel and quasi-geostrophic potential-vorticity maps for the southern summer and northern spring. Comparisons on the dynamics of both polar regions show that, overall, the horizontal wind structure of the regions is very similar. North and south polar jets reach averaged zonal velocities of $140 - 150$ ms^{-1} and present strong cyclonic relative vorticity at the pole, of the order of the Coriolis parameter, while the Hexagon jet and its counterpart in the south (which is located 5° closer to the equator than the Hexagon) are slower, reaching zonal velocity peaks of ~ 100 ms^{-1} and have a weaker relative vorticity, of the order of $\pm 6 \times 10^{-5}$ s^{-1}. Additionally, meridional gradients of the averaged ambient vorticity show that the Rayleigh-Kuo

stability criterion for a barotropic atmosphere is clearly violated at the flanks of the hexagonal jet and its counterpart in the south. Similarly, meridional gradients of the Ertel and quasi-geostrophic potential vorticity show that instabilities could develop at the flanks of the polar jets, as well as at the flanks of the Hexagon and the eastward jet in the south.

We also characterize the cloud morphology of Saturn's north polar region at different wavelengths and its temporal variability, and relate it to the general dynamics of this region, with the aim of understanding the physical processes and seasonal variations that undergo at this region. The appearance and albedo of the north polar vortex changes rapidly at cloud level, as observed between November 2012 and September 2014, however, neither the zonal velocity nor the vorticity changes during this period. Statistical analysis of the number, sizes and distribution of the compact clouds field between 77°N and 84°N does not show any seasonal variations between early spring (January 2009) and beginning of northern summer (June 2013). These clouds present typical sizes of $200-300$ km with an homogeneous meridional (North-South) and non-homogeneous zonal (East-West) distribution. Tracking of these "puffy clouds" indicate that they move with the background and that they migrate neither to the pole nor to the equator, showing a maximum estimated lifetime of $8-9$ days. Lastly, although the Hexagon has remained unchanged over the last 35 years, large transient plume-like activity, presumably of convective nature, has been observed inside its eastward jet at two different epochs, moving, overall, with the background.

Finally, we analyze different interpretations for the nature of the Hexagon. On the one hand, assuming that the velocity of the vertices of the Hexagon reflects the phase speed of a Rossby wave and taking into account the longitudinal and meridional size of a side of the Hexagon, we analyze the three-dimensional dispersion relationship of a free Rossby wave, which suggests that the Hexagon could be the manifestation of a Rossby wave trapped in a region of positive static stability of unknown extension. In addition, we perform numerical analyses in order to find the fastest growing modes of barotropic and baroclinic instabilities as another plausible mechanism for the origin of the Hexagon. In the context of the shallow water barotropic instability, the zonal wavenumber of the maximum growth rate is 6 at the north and 7 at the south for a Rossby deformation radius of $L_D = 1,000$ km, while for a baroclinic instability it is of the order of 30 for both jets.

Since the dynamics of both polar regions are very similar, this analysis provides no hints about the reasons for the absence of a long-lived hexagon in the south polar region of the planet, other than the difference in latitude of the corresponding jet. Furthermore, the longevity of the Hexagon, the large temporal stability of its zonal wind profile, and the survival to the long north polar winter, suggest that the Hexagon could be a manifestation of the meanders of deep rooted unstable jet.

Chapter 1

Introduction

Saturn is the sixth planet from the Sun and the second largest planet of the solar system. It is located at a mean distance of $1,427$ million kilometers from the Sun, 9.58 times Earth's to Sun distance. It follows an elliptical orbit of eccentricity $e = 0.0565$ (Earth's orbit eccentricity ~ 0.017) and thus, the shortest (perihelion) and largest (aphelion) distance from the star are $1,352$ million kilometers and $1,514$ million kilometers respectively. Its orbital period is $10,759.22$ Earth days, this is, 29.46 Earth years.

Saturn is a fluid planet with a mean density of 0.6 $\mathrm{g\,cm^{-3}}$ and together with Jupiter, it is part of the so called Gas Giant planets. It is a rapid rotating planet, however, as we will describe in section 1.1.4, its precise rotation period (sidereal day) is not determined yet. Due to its fast rotation period, it is the most oblate planet of the Solar System with a equatorial radius of $\sim 60,300$ km (around 9.5 times the equatorial radius of the Earth) and a polar radius of $\sim 54,300$ km (around 8.5 times the polar radius of Earth), implying an oblateness of ~ 0.1.

Saturn's rotation axis is tilted an angle of 26.7° with respect to the ecliptic, a similar angle to that of Earth (23.4°). Saturn's equatorial plane inclination, together with the presence of the rings and their shadows, result in seasonal variations on its atmosphere. Table 1.1 summarizes the most important characteristics of Saturn and compares them with the Earth's.

As the rest of the planets of the Solar System, Saturn formed from a protoplanetary disc, which evolved due to gas and dust left overs from the Sun's formation. It was formed, like all Giant Planets, beyond the frost line located at 4 AU (1 AU $\sim$ 150 million kilometers), where temperatures were low enough for icy compounds to remain solid. Compared to the metals that formed the terrestrial planets, the icy materials were more abundant and planets grew massive, capturing the lightest elements, such as hydrogen and helium.

Giant planets are conventionally divided in two groups depending on the radius, mass and density: Gas Giants (Jupiter and Saturn) and Icy Giants (Neptune and Uranus). Gas Giants are mainly composed by hydrogen and a smaller fraction of

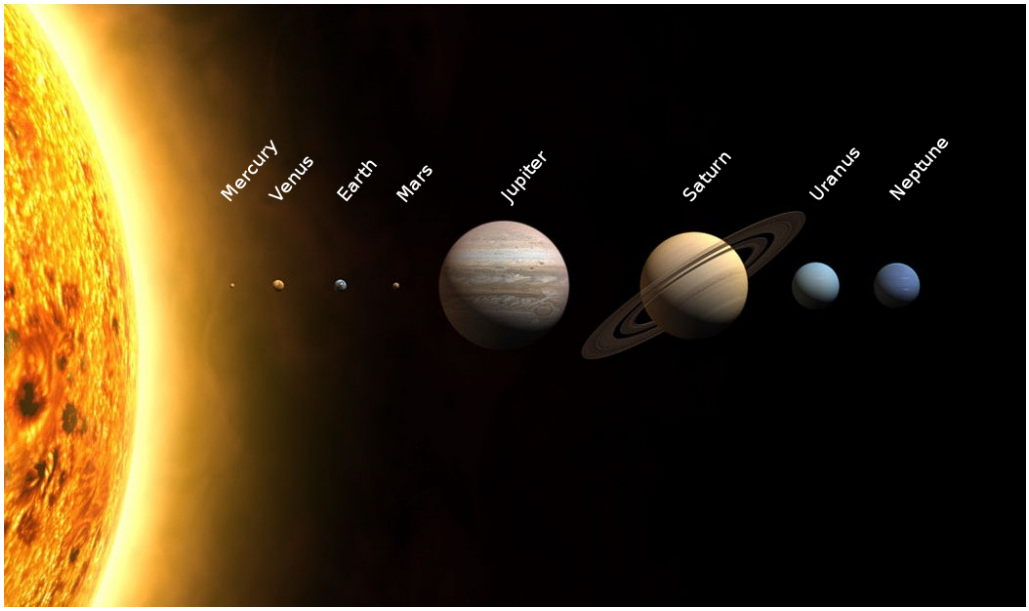

Figure 1.1: Illustration the planets of the Solar System. From left to right we found Mercury, Venus, Earth, Mars, Jupiter, Saturn, Uranus and Neptune. Distances to the Sun are not in scale.

	Earth	***Saturn***
Mass (kg)	$5.98 \cdot 10^{24}$	$5.68 \cdot 10^{26}$
Equatorial Radius (km)	6,378	60,268
Polar Radius (km)	6,356	54,364
Density (g cm^{-3})	5.51	0.69
Mean Distance to Sun ($\times 10^8$ km)	1.49	14.27
Orbital Period (Years)	1.00	29.46
Rotation Period (Hours)	23.93	10.23
Orbital Eccentricity	0.0167	0.0565
Orbital Tilt (Degrees)	23.4	26.7

Table 1.1: Main properties of Saturn and Earth. Data obtained from (Sánchez-Lavega, 2011) and NASA.

helium and they lack of a solid surface. In the case of Saturn, it may contain a solid solid rocky core. The core is surrounded by a liquid hydrogen layer, which turns into metallic hydrogen near the core due to the increase in pressure.

The icy and giant planets in the Solar System have rings orbiting around them, however, Saturn's rings are the most important and spectacular, spanning up to 282,000 kilometers with a thickness of about one kilometer. Saturn's rings are

mostly made up of water ice blocs of different sizes (from centimeters to tens of meters) and have numerous gaps between them.

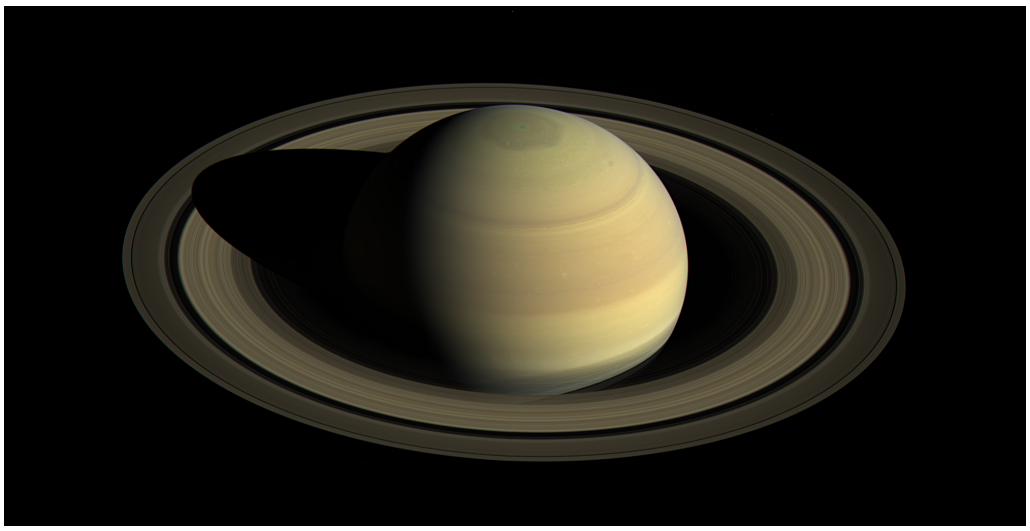

Figure 1.2: Saturn captured by Cassini in 2016. (Figure from NASA)

1.1 Saturn's Atmosphere

On terrestrial planets (Mercury, Venus, Earth and Mars), the atmosphere is defined as the layer of gases surrounding the solid surface due to the gravitational force. In the case of Saturn, which is a gaseous planet, the atmosphere is deep, extending down to $\sim$ 100 Mbar and we define the weather layer as a thin upper layer of around 600 km from 1 mbar to 10 bar pressure,where hazes and clouds of various species form. This layer corresponds to 1 % of Saturn's equatorial radius.

1.1.1 Composition

Saturn's atmosphere is mainly composed by hydrogen (85%) and helium (14%) (Sánchez-Lavega, 2011). However, as there are not *in situ* measurements on Saturn's atmosphere, estimations of the abundances of these two components vary depending on different models of Saturn's formation, evolution and interior.

Carbon, nitrogen, oxygen and sulfur are also present in Saturn at a smaller proportion combined with hydrogen creating basic compounds, such as, ammonia (NH_3), water (H_2O), methane (CH_4) and probably hydrogen sulfide (H_2S) (Fouchet et al., 2009), which probably combines with NH_3 and form NH_4SH, although it has not been detected yet. All these species are the most condensible compounds on Saturn forming clouds at different pressure levels (del Genio et al., 2009). Moreover, different photochemical products of methane and various disequilibrium species,

such as phosphine (PH_3), germane (GeH_4), arsine (AsH_3) and carbon monoxide (CO) are also found in smaller proportions above clouds (Fouchet et al., 2009).

The precise abundances of the condensible species is still an open question. Ammonia, water and the chemical compound ammonium hydrosulfide (NH_4SH, which is obtained by the combination of ammonia and hydrogen sulfide) condensate at different pressures (see section 1.1.3) making it difficult to measure the real abundances of these compounds at the interior of the planet. Various estimations of methane abundance, retrieved using different techniques, do not agree with each other. Values of the mixing ratio of these compounds from diverse periods and obtained by different techniques can be found, for example, in Fouchet et al. (2009).

1.1.2 Thermal Structure

A good knowledge of the thermal structure of a planet's atmosphere is essential to the understanding of its atmospheric dynamics. Saturn's atmospheric temperature is retrieved from two different sources: radio occultations and thermal infrared sounding. The first source gives temperatures with very high vertical resolution, but at very specific locations and the second one, provides vertical temperatures of low vertical resolution but higher spatial resolution.

The temperature-pressure profile retrieved using Cassini's Composite and Infrared Spectrometer (CIRS) in 2004 is shown in figure1.3a. The vertical temperature structure divides the atmosphere in two different regions in altitude: (i) The stratosphere, a tenuous layer at pressures lower than 80 mbar, where temperature decreases with pressure and (ii) the troposphere, the lower region of the atmosphere, with pressures higher than 80 mbar, where temperature increases with pressure. Dividing these two regions we find the tropopause at approximately 80 mbar. Below the 1 bar pressure level, the atmosphere is assumed to have an approximate adiabatic behavior, which implies that at higher pressure levels temperature profiles are determined by dynamics and convection, while higher in the atmosphere, solar heating has an important effect in temperature and dynamics.

The dependence of temperature on latitude and season shows different behaviors depending on the pressure level, as it is shown in figure1.3b. At the stratosphere the zonal temperature is highly variable due to seasonal variations, reaching values of around 160 K at the summer pole and around 130 K at the winter pole. Descending in the atmosphere, at the lower stratosphere and around the tropopause, the zonal temperature shows an smaller seasonal dependence, presenting a low latitudinal temperature gradient. At these pressure levels, the summer pole is around 20 K warmer than the winter pole. Finally, below 400 mbar seasonal effects are no longer noticeable and the temperature remains nearly constant from pole to pole, increasing from around 100 K at around 400 mbar to 130 K at 1 bar pressure (Fletcher et al., 2007).

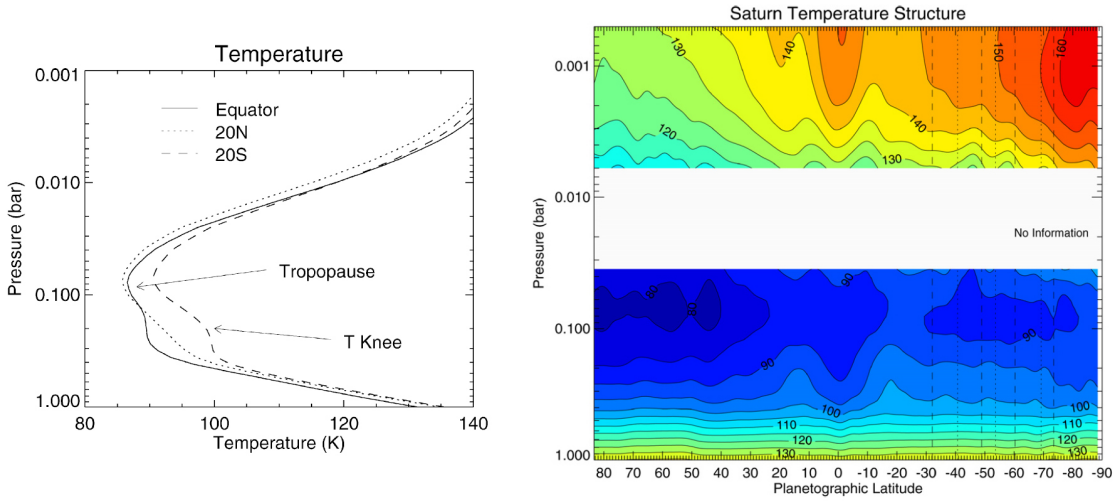

Figure 1.3: Temperature-pressure profile of Saturn's atmosphere from 1 mbar to 1 bar retrieved from Cassini CIRS in 2004 (left) and temperature map covering all latitudes from 0.5 mbar to 1 bar retrieved from Cassini CIRS during the prime mission (right). The gap between 5 and 50 mbar is due to the spectra not being sensitive to temperature at that pressure range. (Fletcher et al., 2007)

1.1.3 Weather Layer

The weather layer is defined here as the region of the atmosphere where meteorological phenomena occur, and as we will describe below, it encloses the stratosphere and troposphere down to $\sim$ 10 bar. Different types of clouds form in this region, allowing us to determine atmospheric motions associated to zonal winds, storms, vortices and other meteorological phenomena. At the troposphere, where the temperature increases with pressure, atmospheric parcels that are transported upwards encounter lower temperatures. In a pressure-temperature diagram, the altitude at which a given compound will condense is given by the point where the saturation pressure vapor curve of a compound and the temperature profile of the atmosphere cross. As different compounds condensate at diverse temperatures, clouds of different compounds will form at different pressure levels. This is illustrated in figure 1.4. In order to obtain an estimation of the height of the cloud tops, the saturation pressure vapor curve of the species can be obtained by solving the Clausius-Clapeyron equation (Sánchez-Lavega et al., 2004).

As mentioned above, the abundance of the compounds in Saturn's atmosphere it not yet fixed. This, together with the uncertainties on the vertical thermal structure, imply different results for the altitude of the top of the clouds when using different thermodynamic models.

In the case of Saturn, the main condensible gases are ammonia (NH_3), ammonium hydrosulfide (NH_4SH) and water (H_2O). A thermochemical model from Atreya and Wong (2005), which assumes oxygen (O), nitrogen (N) and sulfide (S) enrichment by a factor of five over solar composition, gives three different cloud

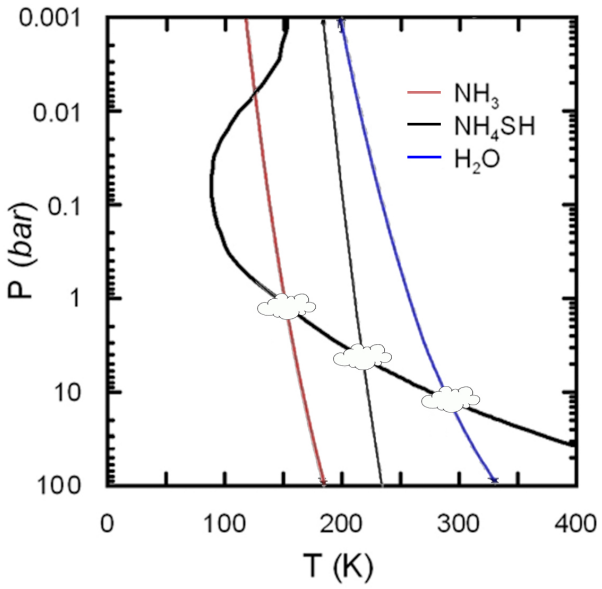

Figure 1.4: Location of the formation of the different clouds on Saturn's troposphere. The black thick solid line represents the vertical temperature profile and the red, blue and thin black lines represent the saturation pressure vapor curves of ammonia, water and ammonium hydrosulfide. (Data obtained from Sánchez-Lavega et al. (2004))

layers on Saturn's troposphere (see figure 1.5). At the top of the troposphere, the ammonia condenses forming ammonia ice clouds at temperatures between 115 K and 165 K that corresponds to 600 mbar (top) and $1.5 - 2$ bar (base). This cloud layer is the highest one and it is the only one visible at near-infrared and visible wavelengths, where clouds are observed bright. Moving into higher pressures, the base of solid NH_4SH ice cloud layer is found at $5.5 - 6$ bar (235 K), and that of water ice is located at $9 - 10$ bar (235 K). Similar results are obtained from a simpler thermodynamical model by Sánchez-Lavega et al. (2004), shown in figure 1.4.

1.1.4 Atmospheric Dynamics

In the study of atmospheric dynamics in a planet without a solid surface, like Saturn, the reference system for motions and the rotation period of their interior cannot be measured directly, since regions at different latitudes of the atmosphere rotate at different rates. In the case of Saturn, three diverse reference systems have been introduced. The first two, named System I and System II, at based in the motion of the atmosphere at equatorial and non-equatorial latitudes, respectively, and give rotation periods of 10 hours and 14 minutes in System I and 10 hours 39 minutes in System II. System III, however, is based on measurements from Voyager flybys of the periodicity in Saturn Kilometric Radiation (SKR), which is assumed to be related to Saturn's magnetic field, and thus, reflect the rotation of Saturn's interior. The mean rotation period in this system is 10 hours 39 minutes and 24

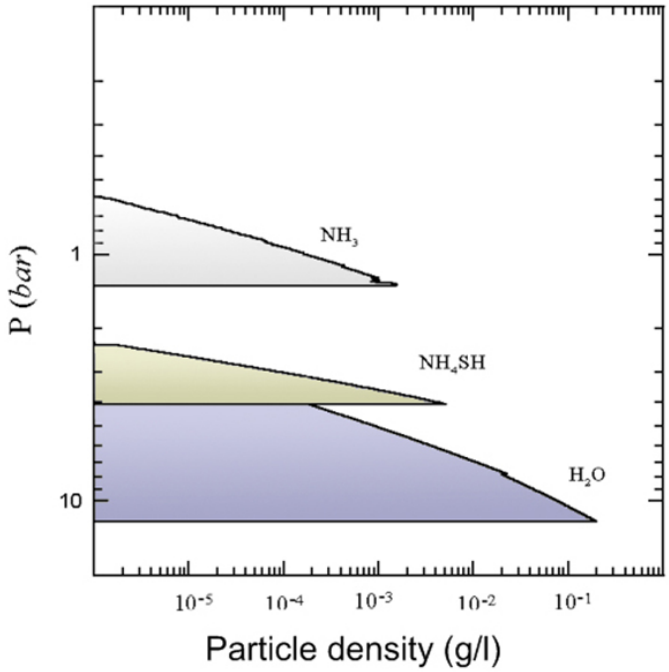

Figure 1.5: Vertical locations of the condensed clouds on Saturn's troposphere. (Data obtained from Sánchez-Lavega et al. (2004))

seconds (Desch and Kaiser, 1981; Seidelmann et al., 2007). So far, this is taken as the standard rotation period of Saturn (Davies et al., 1995; Archinal et al., 2011).

However, the actual value of Saturn's rotation period is still an open question. During the last 30 years, measurements of the modulation of the SKR showed variations of 1% (Galopeau and Lecacheux, 2000; Gurnett, 2005; Kurth et al., 2007). Moreover, during the Cassini era, SKR has displayed two different periodicities (Kurth et al., 2008), one for each hemisphere, that differ 15 minutes from each other (Gurnett et al., 2009). Since it is unlikely that the rotation rate of the planet's interior has changed in such a short period of time, the fact that the periodicities of the SKR reflect the rotation period of Saturn has been questioned. For that reason, other methods to determine the rotation rate of the planet have been proposed, based on Saturn's gravitational field (Anderson and Schubert, 2007) and on the stability of the potential vorticity of zonal jet streams (Read et al., 2009b), leading to a rotation period of 10 hours 34 minutes and 10 hours and 32 minutes, respectively. Finally, Sánchez-Lavega et al. suggested that the rotation period of the hexagon of 10 hours 39 minutes 23.01 seconds could represent the internal rotation period of Saturn (Sánchez-Lavega et al., 2014). Since this is still an open problem, on this dissertation all winds are measured related to System III.

Furthermore, as Saturn is an oblate spheroid (with two radius R_e and R_p) due to its rapid rotation, two different latitude systems are defined: planetocentric latitude and planetographic latitude. The planetocentric latitude, ϕ_{pc}, is the angle from the

equatorial plane to a line that connects the planet's center and the surface point, while planetographic latitude, ϕ_{pg}, is the angle from the equatorial plane to the line perpendicular to the surface point. See figure 1.6. Both latitude systems are related by the next equation:

$$\tan \phi_{pg} = \left(\frac{R_e}{R_p}\right)^2 \tan \phi_{pc} \tag{1.1}$$

(Sánchez-Lavega, 2011). In this equation, R_e and R_p are the equatorial and polar radius respectively. All latitudes in this dissertation are planetocentric latitudes.

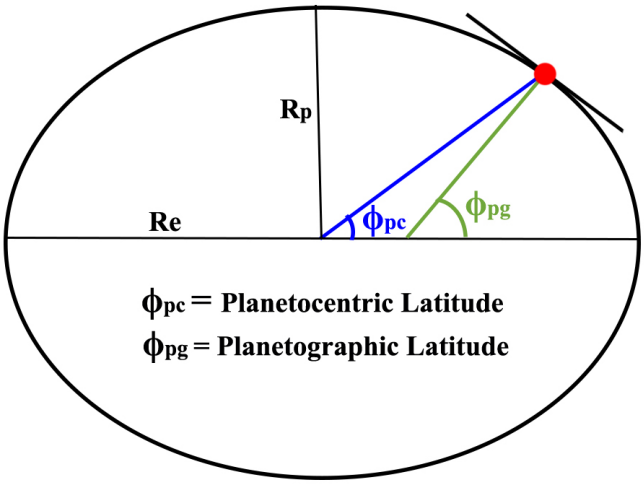

Figure 1.6: An illustration of planetocentric and planetographic latitudes. R_e and R_p represent the equatorial and polar radius respectively.

Saturn is a rapid rotating planet, and its atmosphere presents enduring east-west jets at different latitudes, from the equator to the poles. Due to their large length scale and the rapid rotation of the planet, the Rossby number, $R_o = U/fL$ (where U is the horizontal velocity, $f = 2\Omega \sin \phi$ is the Coriolis parameter and L is the horizontal length scale) is smaller than one away form the equator. Thus, large scale winds are in geostrophic balance, which implies that the horizontal pressure gradient and the Coriolis force are balanced. In this case, the rotation rate dominates the nonlinear advection term and thus, horizontal velocities verify

$$fu \approx -\frac{1}{\rho}\frac{\partial P}{\partial y} \tag{1.2}$$

$$fv \approx \frac{1}{\rho}\frac{\partial P}{\partial x} \tag{1.3}$$

where, u and v are the zonal and meridional velocities, ρ is the density and P is the pressure (Vallis, 2006; Sánchez-Lavega, 2011). A geostrophic wind term is defined

as follows

$$\vec{V_g} = \hat{k} \times \frac{1}{\rho f} \nabla P \tag{1.4}$$

(Sánchez-Lavega, 2011). In the case of Saturn, $u \approx u_g$ and $v \approx v_g$ except at the equatorial latitudes.

First measurements of the motion of the top clouds on Saturn's atmosphere were not carried out until the Voyagers captured the first high resolution images of Saturn in the flybys of 1981 and 1982 (Smith et al., 1981, 1982; Sánchez-Lavega et al., 2000). Afterward, they were measured again using images captured by the Hubble Space Telescope (HST) in the late 90's and early 2000's (Sánchez-Lavega, 2002a; Sánchez-Lavega et al., 2003, 2004). Finally, the arrival of Cassini to Saturn allowed to measure winds at very high resolution (Porco et al., 2005; Vasavada et al., 2006; del Genio et al., 2007; Sánchez-Lavega et al., 2007; Choi et al., 2009; García-Melendo et al., 2010, 2011; del Genio and Barbara, 2012; Sayanagi et al., 2013a,b, 2014; Antuñano et al., 2015; Sayanagi et al., 2017).

Saturn's zonal wind profile obtained by measuring the motion of features at the top of the ammonia clouds, is shown in figure 1.7. It alternates eastward (prograde) and westward (retrograde) jets from the equator to the poles, but it is not symmetric. Eastward jets on Saturn are stronger than westward jets, which are very weak, reaching maximum velocities of ~ -25 m s^{-1} (García-Melendo et al., 2011). Furthermore, some of these retrograde jets are eastward minimas as they do not reach negative velocities.

Most Saturn's jets are zonal, with averaged motions following the latitudinal circle. However, the eastward jet located at 75.8°N meanders in latitude and presents a hexagonal shape when viewed from above the north pole (Godfrey, 1988).

Saturn's most remarkable jet is the equatorial eastward jet, which extends around 70° in latitude from $\sim$ 35°N to $\sim$ 35°S. Its peak velocity, from around 10°N to 10°S, experiences temporal variability at the top clouds and haze, ranging between $\sim$ 380 m s^{-1} and $\sim$ 450 m s^{-1} in the last $\sim$ 35 years (Sánchez-Lavega et al., 2000; Sánchez-Lavega et al., 2003, 2007; García-Melendo et al., 2011). Moreover, it also presents an intense vertical wind shear (Sánchez-Lavega et al., 2016b). The reason of these variations is yet unknown but it is likely related to seasonal variations, which are only noticeable at the equator, where ring-shadowing intensifies seasonal effects.

Other eastward jets on Saturn are less intense, showing peak velocities of $\sim$ 100 m s^{-1} (located at $\sim$ 70°S,$\sim$ 56°N, $\sim$ 61°N and $\sim$ 75°N), of $130 - 140$ m s^{-1} (at $\sim$ 55.5°S,$\sim$ 42°S and $\sim$ 42°N) and of around 150 m s^{-1} at the polar jets placed at 88.5° north and south (García-Melendo et al., 2011; Antuñano et al., 2015). These jets are stable in time and have remained unchanged over the last 35 years (García-Melendo et al., 2011). Figure 1.7 shows the zonal velocity profile at different epochs.

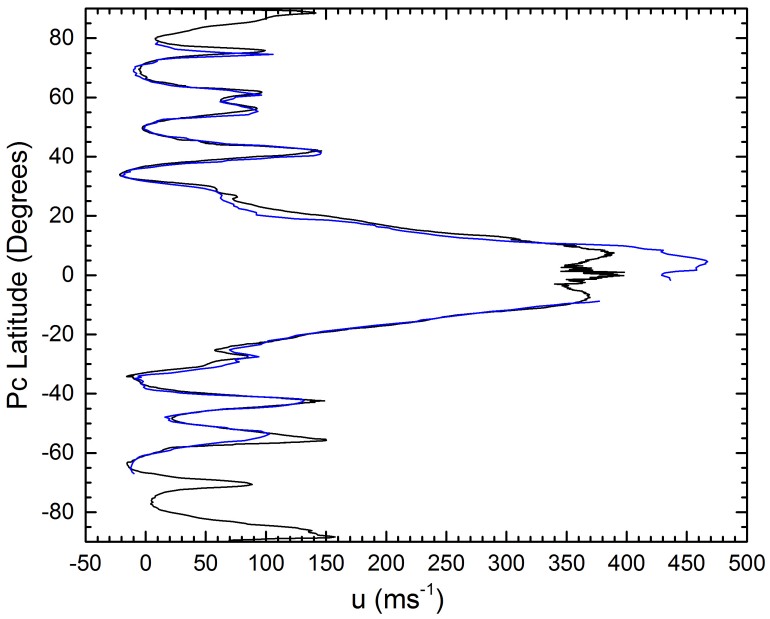

Figure 1.7: Zonal wind profile from Cassini ISS images (black line) between 2004 and 2013 and from Voyager flybys (blue line). (Data obtained from Sánchez-Lavega et al. (2000), García-Melendo et al. (2011) and Antuñano et al. (2015))

So far, two different kind of hypothesis have been introduced in order to explain the origins of the jets found on Giant Planets: the *"shallow forcing"* and the *"deep forcing"* theories. They differ form each other on the way the jets are driven. In the first case, jets are formed from momentum transfer in a thin outer layer of the atmosphere, due to instabilities such as baroclinic, or to convection. Deep forcing theories are driven by internal heat and convection coupled to the rapid rotation of the planet (Vasavada and Showman, 2005; del Genio et al., 2009; Sánchez-Lavega et al., 2017).

Shallow forcing models assume that, although jets are formed in a thin outer layer, the circulation of the atmosphere is localized at the weather layer down to $\sim$ 10 bar or deeper, down to $\sim$ 100 bar (Showman et al., 2006). These models are basically adaptations of the terrestrial geophysical fluid dynamics models, as Earth's atmosphere represents a very thin layer compared to Earth's radius. In these models, thermal radiation heats the weather layer, creating meridional temperature gradients from the equator to the poles. This, together with the β-effect created by the rapid rotation of Saturn, are responsible of the formation of jets. The models are able to reproduce some of the mid and high latitude jets and some of their features, showing that turbulence could explain some of the observed structures in the upper troposphere. However, these models do not reproduce accurately the structure of the jets found on Saturn, such as the presence of an intense eastward jet at the equator.

Deep forcing models are based on the assumption of a nearly barotropic interior, heated from internal energy sources. Proudman theorem (Taylor, 1923), implies that when a rotating deep and barotropic fluid is perturbed due to a solid core or internal heat source, there are no gradients on the velocity field in the direction of the rotation axis, and the flow forms columns parallel to this axis. Numerical models, based on these ideas, can explain the formation of the intense equatorial jet on Saturn and maybe some of the jets located at high latitudes.

So far, both scenarios are able to reproduce the presence of jets and vortices on Saturn's atmosphere, but the formation of these structures is yet an open question. Moreover, models that mix both scenarios are also being considered (Vasavada and Showman, 2005).

1.1.5 Meteorological Features

Saturn's atmosphere, when observed in visible and near-infrared wavelengths, presents many different cloud structures inmersed between the east-west jets mentioned above. The origin, evolution, life-times and dimensions of these features are very different from one to another. Here we describe various types of cloud structures as classified by Sánchez-Lavega et al. (2017) and we introduce the most remarkable features of each type.

- **Vortices**. These are usually elliptical ovals observed brighter or darker than their surroundings when seen at visible wavelengths. They present anticyclonic or cyclonic vorticity depending on their location and they are usually long-lived features with typical sizes smaller than $3,000$ km. One notable example of a vortex on Saturn is the so-called **North Polar Spot (NPS)**, an elliptical anticyclone of around $10,000 \times 5,000$ km present at around 73°N that survived at least from 1981 to 1995 (Godfrey, 1988; Caldwell et al., 1993; Sánchez-Lavega et al., 1993, 1997). This vortex is shown in figure 1.8d. Cyclones (del Río-Gaztelurrutia et al., 2010) and anticyclones, as the one formed following the GWS in 1990 (Sayanagi et al., 2014) are other notorious examples.

- **Convective storms**. These are bright features that evolve rapidly in a short period of time of the order of days by moist-convection (Ingersoll et al., 1984; Dyudina et al., 2007). A particular case of convective storms are the major outbreaks so-called **Great White Storms (GWS)**, which evolve into planetary-scale disturbances changing the appearance of a latitudinal region of the atmosphere. GWSs appear with an approximate periodicity of 30 years and the two latest and better studied events occurred at equatorial and mid latitudes on Saturn's atmosphere in 1990 and 2010-2011, respectively (Barnet et al., 1992; Sánchez-Lavega, 1994; Sánchez-Lavega et al., 2011; Fletcher et al., 2011; Sánchez-Lavega et al., 2012; Fletcher et al., 2012; Sayanagi et al., 2013a; Sánchez-Lavega et al., 2016a). The GWS from 2010-2011 encircled the whole planet at mid-latitudes, without changing significantly the horizontal wind

structure (Sánchez-Lavega et al., 2011, 2012; Sayanagi et al., 2013a). Figure 1.8a, shows the head of the GWS from 2010.

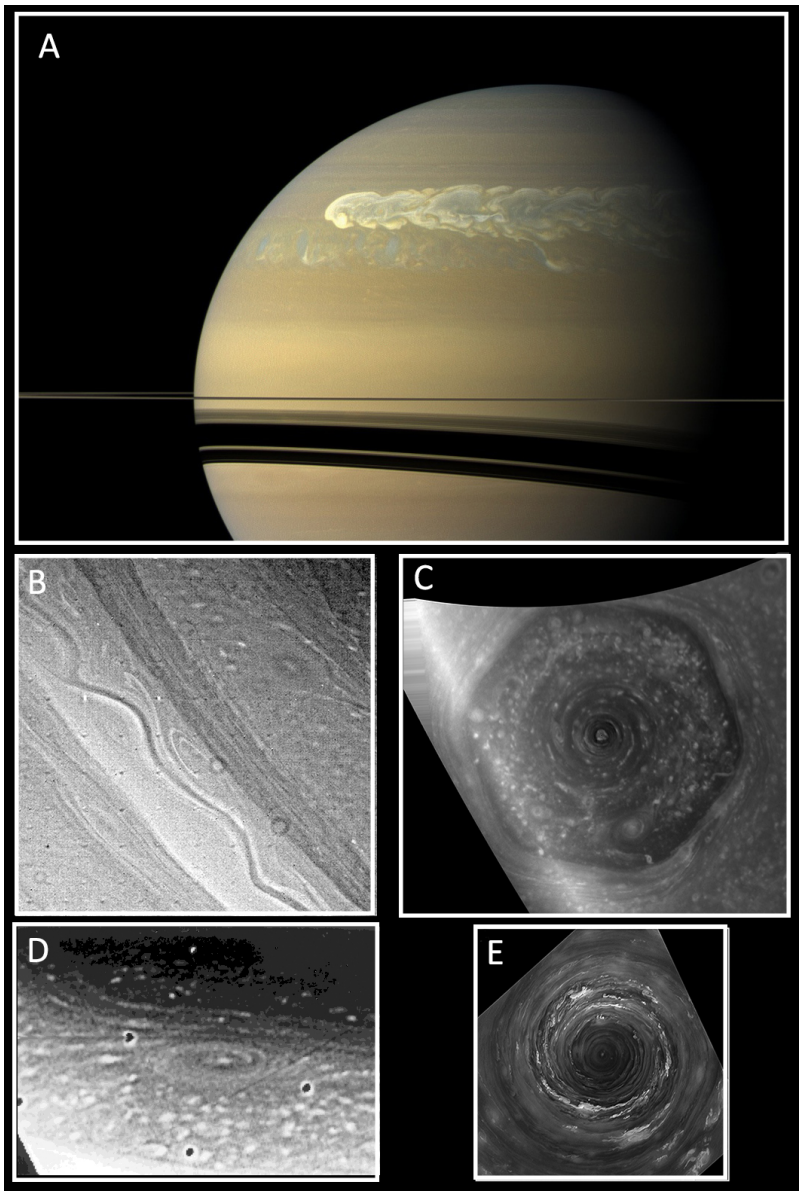

Figure 1.8: Different meteorological features found on Saturn's atmosphere: Great White Storm captured by Cassini ISS cameras on 22 July 2011 (A), the Ribbon captureb by the Voyager II flyby on 23 August 1981 (B), the Hexagon and its fast eastward jet captured by Cassini ISS with CB2 filter on 22 June 2013 (C), the North Polar Spot captured by the Voyager II flyby on 23 August 1981 (D) and the North Polar Vortex captured by Cassini ISS NAC camera using CB2 filter on 14 June 2013 (E). Figure built using images obtained from NASA/JPL (A), PIA01378 image from NASA (B) and from Sánchez-Lavega et al. (1997).

- **Wave patterns**. On Saturn's northern hemisphere, there are two singular features that present a wave pattern: (i) **the Ribbon** and (ii) **the Hexagon**.

The Ribbon is a long-lived wavy feature discovered on Voyager images located at the eastward jet at 41°N (Smith et al., 1982; Sromovsky et al., 1983) and it remains present in Cassini images, although with a different morphology. It encircles the planet moving at the same velocity as its background, $\sim 140\ \mathrm{m\,s^{-1}}$ (Sromovsky et al., 1983; Sánchez-Lavega, 2002b), and it has been interpreted as a baroclinic dynamic instability in the jet (Godfrey and Moore, 1986; Sayanagi et al., 2010). The Hexagon, is also a long-lived stable feature discovered on Voyager images at ~ 75°N (Godfrey, 1988). This feature is a singular structure as it encloses a fast eastward jet of around $100\ \mathrm{m\,s^{-1}}$ (Godfrey, 1988; Sánchez-Lavega et al., 1993; Caldwell et al., 1993; Baines et al., 2009; Antuñano et al., 2015). However, its vertices, instead of following the background velocity, remain almost fixed to Saturn's interior (Sánchez-Lavega et al., 2014). A detailed study of the Hexagon dynamics and cloud-morphology is given in chapters 3 and 4, since it is one of the objectives of this dissertation. The Ribbon and the Hexagon are shown in figure 1.8b and 1.8c .

- **Polar vortices**. Saturn presents two long-lived and stable cyclones, one on each pole. They are almost circular and cover latitudes from the poles to 88.5° (Sánchez-Lavega et al., 2006; Dyudina et al., 2008; Baines et al., 2009; Antuñano et al., 2015; Sayanagi et al., 2017). Their horizontal wind structure and cloud morphology are described in chapters 3 and 4, since it is part of the research of this study. Figure 1.8e, shows the north polar vortex captured by Cassini ISS NAC camera.

1.2 Saturn's Observations: History

Saturn has been known since the prehistoric times and it is the most distant of the five planets visible to the naked eye. Ancient Greeks named it after the god of agriculture, Kronos. Later, Romans named the god and the planet Saturn (or Saturnus), the Roman equivalent of Kronos. Saturn was also given different names in other cultures, for example, Shani in the Hindu culture, Shabbathai to the ancient Hebrews or "earth star" in ancient China and Japan.

Galileo Galilei was the first to observe Saturn directly with a telescope in 1610 and using his telescope he discovered Saturn's rings. However, due to the low resolution of the telescope, he thought that these rings were two moons located at each side very close to the planet. Few years later, he concluded that the rings were some sort of "arms". As a result of the improvements on telescopes' optics, the Dutch astronomer Christiaan Huygens deduced in 1659, that what Galileo saw was actually a solid disk-like ring around Saturn. In addition, he discovered Saturn's first moon, Titan. Few years later, in 1675, Jean-Dominique Cassini discovered a gap dividing the disc in two rings (called the Cassini gap). He also discovered four more moons: Iapetus, Rhea, Tethys, and Dione. Further significant discoveries were not made until the 18th and 19th century, when in 1789 William Herschel discovered Mimas and Enceladus, two distant moons. Almost a century later, James E. Keeler discovered in 1895, using spectroscopy techniques, that the rings were made

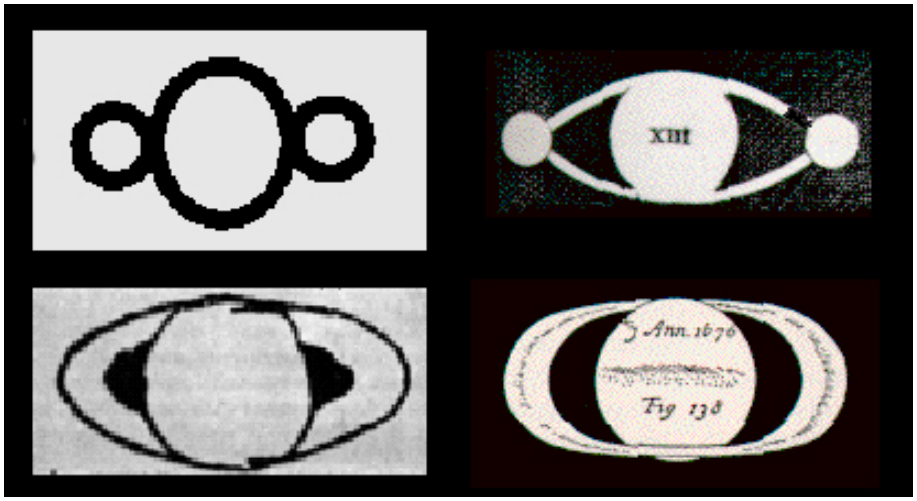

Figure 1.9: Diagrams of Saturn and its rings over the 17th century by Galileo Galilei in 1610 (*top left*) and 1616 (*bottom left*),Christiaan Huygens in 1659 (*top right*) and Jean-Dominique Cassini in 1675 (*bottom right*).

up of small objects orbiting around Saturn at different rates. During the early 20th century, in 1944, it was confirmed that Titan had a thick atmosphere, not present in any other moon of the solar system.

As it is illustrated in figure 1.10, before the 20th century, visual drawings were used to analyze and characterize the observations. However, at the beginning of the 20th photography started to develop, allowing to image and characterize by spectroscopy the cloud morphology of the planets. Finally, in the late 20th century, large improvements on adaptive optics and the creation of the CCD, made a big step on the image resolution of ground-based telescopes. At the same time, space explorations of the outer planets started to take place providing unprecedented data. The new data provided by both sources enabled a fast development on the knowledge of Saturn's atmosphere, composition and rings structure.

1.2.1 Early Space Exploration

Since the late 70's Saturn has been explored by different unmanned spacecrafts. The first three missions sent to study this planet, its rings and its moons were flybys and they took place between September 1979 and August 1981. Below we describe these missions.

The first mission to explore Saturn and its rings during a flyby in 1979 was the Pioneer 11. It was part of the American series of unmanned missions designed for planetary exploration. It was launched in April 1973, and after its flyby of Jupiter in December 1974, it headed to Saturn and passed by it at a distance of 21,000 kilometers (Northrop et al., 1980). This spacecraft was targeted to pass through Saturn ring plane in order to test the route for the Voyagers I and II that were heading to Saturn at that time, but it was finally canceled.

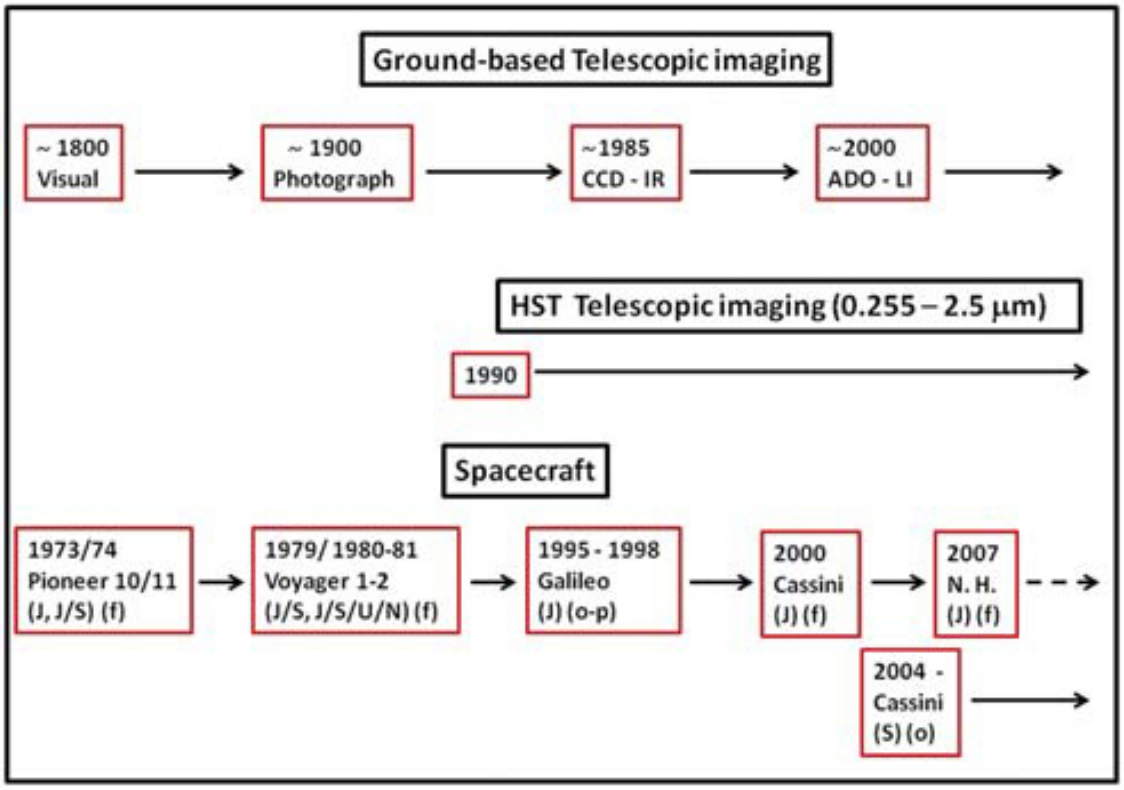

Figure 1.10: Diagrams of the observations history of the giant planets. Acronyms: Giant planets initials (J,S,U,N); CCD (Charge Coupled Detectors digital), ADO (Adaptative Optics), LI (Lucky Imaging), HST (Hubble Space Telescope), N.H. (New Horizons), Spacecraft trajectories (f=flyby; o=orbit; p=probe). (Figure from Sánchez-Lavega et al. (2017)).

Pioneer 11, imaged Saturn's rings and various moons in detail for the first time, some of them from a very close distance (like the moon Janus that was imaged from 2,500 km distance), using an imaging photopolarimeter. In these images, Saturn's rings looked dark while gaps looked bright, contrary to what it is observed from Earth.

It also discovered a new moon and an undiscovered ring. Moreover, using an infrared radiometer, it found that although Titan has a thick atmosphere its surface is too cold for life to grow. It also gave the first detailed results of the high stratosphere of Saturn, showing that is is warmer than the lower stratosphere (Kliore et al., 1980a,b). In addition, the two different magnetometers onboard traced Saturn's magnetosphere and discovered that its magnetic field is surprisingly aligned with its rotation axis (Smith et al., 1980b,a; Acuña and Ness, 1980), unlike other planets and stars. Figure 1.11 shows Saturn and its moon Titan captured by the Pioneer 11 and Voyager II flyby.

The next space missions to reach Saturn were the American unmanned Voyager I and II spacecrafts. They were launch in September 1977 and August 1977, re-

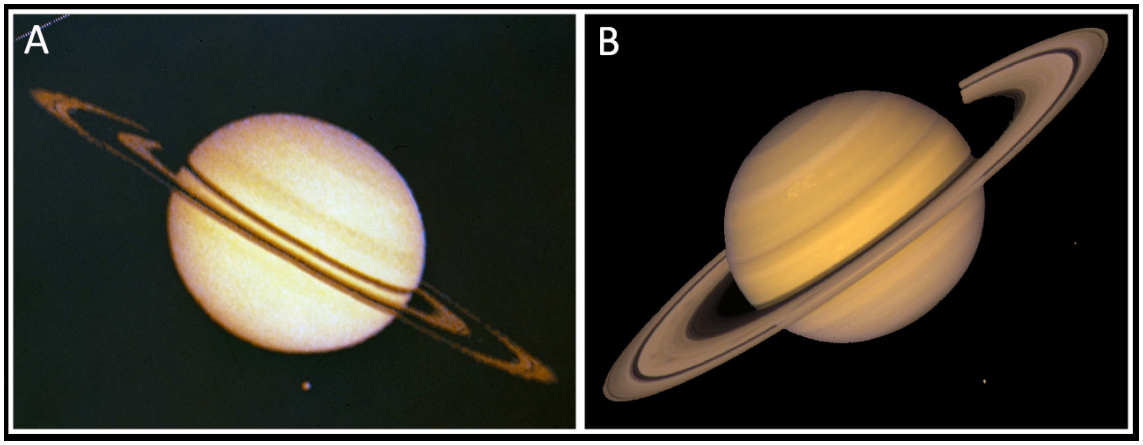

Figure 1.11: Comparison of the image resolution of Saturn between the Pioneer 11 and Voyager II. Figure A is a RGB composition of Saturn and its largest moon Titan captured by Pioneer 11 at 2.84 million kilometers from Saturn and Figure B is a RGB composition of Saturn captured by Voyager in 1981. (Figures from NASA).

spectively, from Cape Canaveral. Their mission was planned to last around 5 years and its main objective was to expand the exploration of Jupiter, Saturn and their moons. Twelve years after they were launched, their mission was expanded to extend the exploration of the Solar System beyond the outer planets to its outer limits.

After Jupiter flybys in March 1979, the Voyager I spacecraft encountered Saturn in November 1980, nine months before its twin Voyager II, in a nearly equatorial flyby orbit. Both voyagers provided detailed new information of Saturn's atmosphere, rings and moons, that improved to a great extent our knowledge of the Saturnian system.

Both probes carried among others, an Imaging Science System (ISS), consisting of two cameras with different field of views and filters, which obtained unprecedented images of Saturn's atmosphere and rings (Smith et al., 1981, 1982). The vast number of images taken by these cameras showed for the first time some of the phenomena that we have described in the previous section, such as vortices, jets and different atmospheric disturbances. Among others, they captured the Hexagon (Godfrey, 1988) and "the Ribbon" (Smith et al., 1982; Sromovsky et al., 1983). Furthermore, they also imaged the most intense and widest jet stream of all the planets in our solar system, Saturn's equatorial prograde jet (Smith et al., 1981, 1982; Ingersoll et al., 1984; Sánchez-Lavega et al., 2000).

The Voyagers also detected helium for the first time and gave, although inaccurately, the mixing ratio of helium relative to hydrogen using data from the Radio Science System (RSS) and the Infrared Interferometer Spectrometer (IRIS) (Conrath et al., 1984; Conrath and Gautier, 2000). These findings marked a big step in the study of Saturn's temperature, allowing the retrieval of temperatures up to 700 mbar (pressure at Earth's surface is 1 bar) from the spatially resolved spec-

tra obtained by IRIS (Hanel et al., 1981, 1982). These instruments also played an important role in the investigation of aurora emissions at high latitudes, detected unambiguously for the first time by the Voyagers (Broadfoot et al., 1981; Sandel and Broadfoot, 1981).

1.2.2 Current Missions

After these flybys, Saturn's space exploration had to wait until April 1990, when a NASA and ESA joint project put the Hubble Space Telescope (HST) in orbit around the Earth at about 593 km above sea-level. Its main objective is to capture high-resolution images and accurate spectra of planets, stars and galaxies, from infrared to ultraviolet wavelengths, without any distortion from Earth's atmosphere.

First images obtained by this telescope, showed a spherical aberration in the telescope's primary mirror and after the servicing mission finished in 1994, the HST started to capture high-resolution images. The HST is still operational and allows the detection of discrete features on Saturn larger than 300 km. This was an important improvement, since at that epoch, ground-based telescopes could not detect features smaller than $1,000$ km (del Genio et al., 2009). Figure 1.12, shows the HST captured in 2009 by the servicing mission team.

HST telescope has contributed with important discoveries of Saturn's atmosphere and has allowed a long-term study of some of its features. It captured for the first time high-resolution multi-wavelength images of a GWS, the equatorial Great White Spot (GWS) of 1990 (Barnet et al., 1992; Westphal et al., 1992; Sánchez-Lavega et al., 1993) and a large major feature in 1994 (Sánchez-Lavega et al., 1996). It also re-observed the NPS, the Hexagon and the Ribbon between 10 and 14 years after they were captured by the Voyagers, showing that they are long-lived features (Caldwell et al., 1993; Sánchez-Lavega et al., 1997; Sánchez-Lavega, 2002b). Furthermore, it discovered that although a fast eastward jet is also present in the south polar region, there is no equivalent hexagonal feature in the south hemisphere (Sánchez-Lavega, 2002a). Additionally, the changing structure of the equatorial jet was also revealed in detail (Sánchez-Lavega et al., 2003). Since 1990, the HST has made more than 1.3 million observations of stars, planets and galaxies and it has become one of the most productive scientific instruments ever. Due to its perfect conditions, the mission has been extended until 30 June 2021.

The knowledge of Saturn, its moons and its rings improved significantly with the arrival in 2004 of the first orbiter around Saturn. The American unmanned spacecraft Cassini, launched in October 1997, carries 12 different instruments, which have provided unprecedented spatial and temporal high resolution data. A detailed description of this mission, the spacecraft and its instruments is given in chapter 2.

Since the arrival to Saturn in July 2004, a vast number of discoveries and new studies have been reported. Here, we summarize some of them, focusing on Saturn's atmospheric phenomena and dynamics.

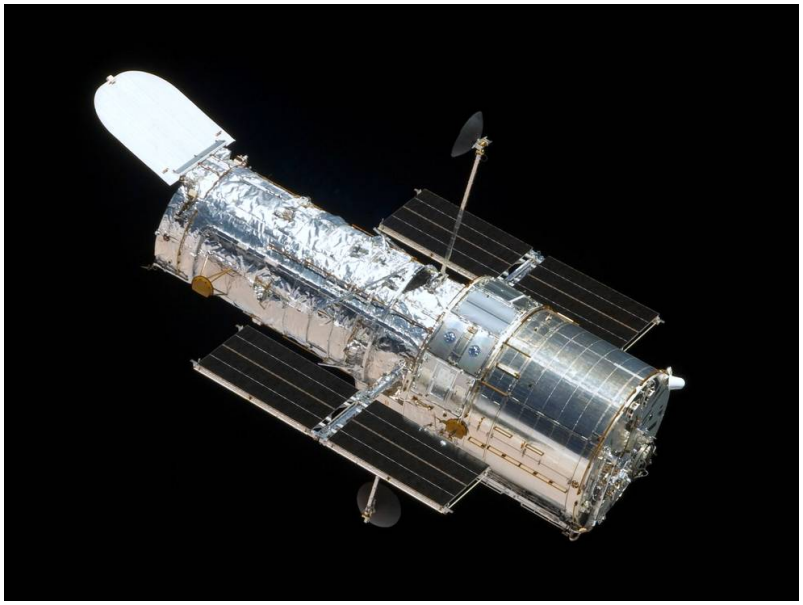

Figure 1.12: Image of the Hubble Space Telescope captured in 2009 during the fourth servicing mission. (Figure from NASA).

High-resolution images of Saturn's atmosphere, captured by Cassini ISS cameras (Porco et al., 2004) over the last 14 years, have allowed an accurate study of the horizontal wind structure and its temporal variability, showing that all jets on Saturn, except the equatorial jet, remain stable over the years (García-Melendo et al., 2011). They have also captured dramatic images of Saturn's polar regions, showing the Hexagon, around 30 years after its discovery, in great detail (Antuñano et al., 2015, 2017) and indicating the presence of two circular polar vortices, one at each pole (Sánchez-Lavega et al., 2006; Fletcher et al., 2007; Dyudina et al., 2008; Baines et al., 2009; Antuñano et al., 2015; Sayanagi et al., 2017).

The thermal structure of the upper troposphere and stratosphere has been studied by temperature retrievals from CIRS data (Fletcher et al., 2007). The results show significant seasonal variations at the stratosphere near the poles, while very small meridional temperature gradients are observed at the lower stratosphere or upper troposphere (Fletcher et al., 2007, 2015).

The Great White Storm (GWS) that erupted at mid latitudes in 2010 was captured by different instruments on-board Cassini, which allowed for the first time a very high-resolution study of one of the most remarkable phenomena in Saturn. ISS cameras captured the GWS storm at different wavelengths and showed impressive images of the disturbances that affected the whole latitudinal band from around 20°N to 42°N (Fischer et al., 2011; García-Melendo et al., 2013; Sayanagi et al., 2013a). During the storm, temperatures at the stratosphere, retrieved from CIRS data, increased around 80 K (Fletcher et al., 2011), being the largest temperature increase ever measured. Moreover, lightning events were observed at optical and radio wavelengths at the head and perturbed region of the GWS (Dyudina et al.,

2013). Finally, VIMS instrument found that, during the GWS, some compounds were transported upward to the upper troposphere, showing some compounds, like water ice, placed at altitudes never observed before (Sromovsky et al., 2013). A review is given in Sánchez-Lavega et al. (2017).

Cassini's measurements of the Kilometric radio emissions (SKR) using the radio and plasma wave instrument differ from the measurements of the Voyager era, and reveal a rotation period 8 minutes longer (Gurnett, 2005; Kurth et al., 2007, 2008). Moreover, they showed that the SKR periodicity of the northern and southern hemispheres are different and that seem to change with seasons (Kurth et al., 2008; Gurnett et al., 2009), implying that the periodicity of the SKR is not a good indicator of the period of Saturn's interior (see the discussion on Saturn's rotation period in section 1.1.4).

1.3 Goals of This Thesis

As described above, the arrival of Cassini spacecraft to Saturn provided a large number of unprecedented high-resolution data, which allowed unveiling some of Saturn's mysteries, but also opened new debates. So far, there are still many unanswered questions, such as: Has Saturn a solid core at its interior? What is the rotation period of Saturn? What is the origin of Saturn's jets and how do they maintain? What triggers and marks the cycle of major GWS storms? How did the polar vortices and the Hexagon originate? Why is there a Hexagonal feature in the north polar region and not in the south? This thesis is devoted to the study of the dynamics of the polar regions, and the following topics are addressed:

- We study and compare the dynamics of Saturn's polar regions using Cassini ISS high-resolution images. For this purpose, we obtain horizontal wind and vorticity maps from 70° (north and south) to the pole. In addition, we compute averaged vorticity and potential vorticity maps of both polar regions. These data are essential to the analysis the stability of the jets found at Saturn's polar regions.
- We characterize the cloud morphology of the polar regions and relate it to the horizontal wind and vorticity profiles, in order to understand the different physical processes that originate the observed atmospheric dynamics. With this aim, we analyze the different features at various wavelengths, analyze their temporal and seasonal variability and compare them with the average dynamics of the regions where they appear.
- We analyze the Hexagon and its dynamics in depth. To this end, we compute horizontal winds and vorticity profiles of the hexagonal jet and we characterize its meandering.
- We study the behavior and growing modes for barotropic and baroclinic instabilities for the hexagonal jet, and explore its behavior in terms of a Rossby wave.

This thesis is organized as follows:

- Chapter 2 describes the observations used in this dissertation and details the instrument characteristics. Moreover, the database, image-processing and wind measurement methods are provided.
- Chapter 3 describes the general averaged dynamics of the polar regions. Horizontal winds and vorticity maps at cloud level are presented, and the zonal averaged velocity, vorticity and vorticity gradients are calculated, extending the knowledge of the region from previous works.
- Chapter 4 details the cloud morphology and temporal variability of meteorological features of the north polar region, such as the hexagon, different vortices, the puffy cloud field and the polar vortex, relating it to the dynamics of this region.
- In chapter 5, different interpretations of the origin of the meandering of the hexagonal jet are explored. In particular, we consider the possibility that the Hexagon is a manifestation of a deep unstable jet or due to a barotropic or baroclinic instability of the jet.
- Finally, chapter 6 summarizes the general conclusions of this thesis and presents possible lines of future work.

Chapter 2

Observations and Methodology

In this chapter, we introduce the Cassini mission and detail the ISS instrument characteristics, such as its cameras, fields of view and filters (section 2.1). Moreover, we describe the image selection software and the database, detailing the information found on each image (section 2.2).

Since ISS images must be processed in order to be used for scientific purposes, we also introduce in this chapter different image processing techniques and the image calibration software (section 2.3), together with navigation techniques and the creation of polar projections (section 2.4). Finally, we describe different methods to measure winds (section 2.5) needed to obtain the horizontal wind structure on Saturn's polar regions.

2.1 Observations

In this dissertation, we analyze the cloud morphology and dynamics of Saturn's polar regions using very high-resolution images captured by the Imaging Science Subsystem (ISS) on-board the Cassini spacecraft, at different wavelengths ranging from the near infra-red ($\sim$ 1000 nm) to violet ($\sim$ 400 nm), between October 2006 and September 2014.

2.1.1 Cassini Mission

The Cassini-Huygens mission is a joint NASA, European Space Agency (ESA) and the Italian Space Agency (ASI) mission. It is one of the most ambitious interplanetary missions ever sent into space and it consists of two modules: (i) an orbiter (Cassini spacecraft) and (ii) a probe (Huygens). They were launched together in October 15 1997 from Cape Canaveral. After seven years of journey, both the orbiter an the probe reached Saturn in July 2004, becoming the first spacecraft ever put into orbit around and outer planet. Almost half a year later, in January 2005, Huygens probe descended with a parachute to the surface of Saturn's largest moon, Titan, obtaining detailed information of its atmospheric composition and thermal and wind

structures, becoming the probe that had landed at the furthest distance from Earth.

The main scientific objective of Cassini is to study Saturn system in detail. For that purpose, the scientific objectives include the study of Saturn, its rings, its icy moons, Titan and the magnetosphere. Here we list some of the objectives of the so-called **"Prime Mission"**:

- Study Saturn's atmosphere by analyzing its horizontal motions, its vertical structure and the daily and seasonal variations.
- Determine the deep structure and rotation of Saturn.
- Study the configurations of the rings, their dynamics and their composition.
- Study Titan's atmosphere by determining the abundances of compounds, the gas distributions, the thermal structure and the horizontal winds.
- Analyze the surface geology, composition and internal structure of icy satellites.
- Study the dynamics of the plasma in the magnetosphere and determine the interaction between the magnetosphere and the satellites.

This mission lasted four years, where Cassini performed 75 orbits around Saturn and 44 flybys of Titan, collecting a great amount of new data. These first orbits and flybys as illustrated in figure 2.1.

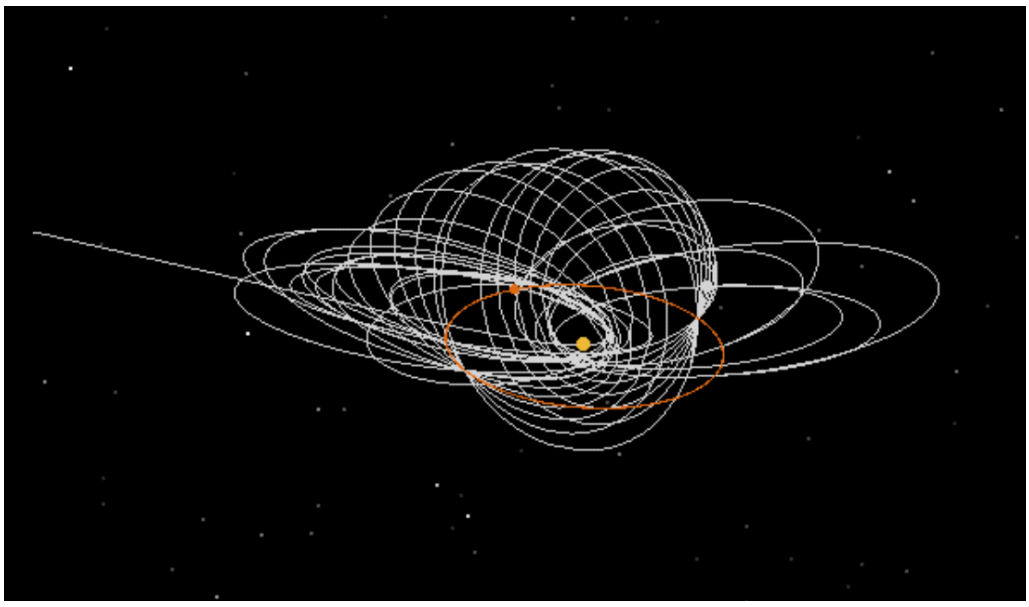

Figure 2.1: An illustration of Cassini's orbits during its Prime Mission. (Figure from NASA/JPL-Caltech)

Due to the large number of discoveries it had achieved and the perfect condition of its instruments, the mission was extended until 2010. The objectives of

this extension, called **"Equinox Mission"**, were modified in order to answer new questions. The main objectives of this new mission were focused on determining seasonal variations on Saturn's and Titan's atmosphere, their composition, thermal structure and winds, as well as variations on the icy satellites and Saturn's rings.

During this extended mission Cassini completed 65 new orbits around Saturn, 27 Titan flybys and 7 Enceladus flybys. At the end of this period, the mission was again extended, starting the so called **"Solstice Mission"**, which lasted until 2016. During this new extended mission it performed 155 orbits around Saturn, 54 flybys of Titan and 11 flybys of Enceladus. These new orbits are shown in figure 2.2. The objectives of this last mission were to study, for the first time, seasonal and temporal changes over a full-seasonal period and continue investigating the discoveries made in the earlier phases.

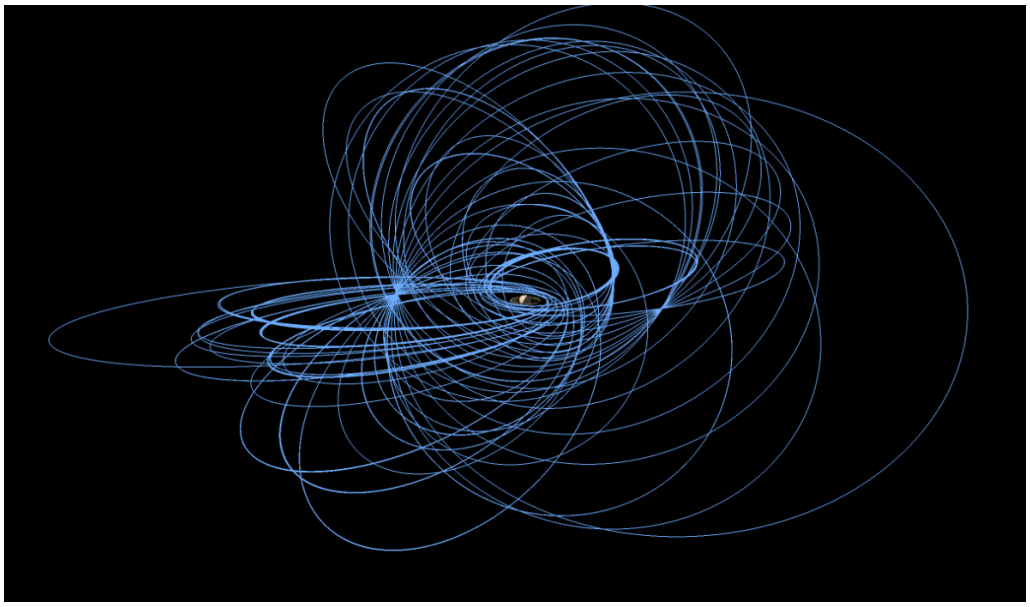

Figure 2.2: An illustration of Cassini's orbits during its Solstice Mission. (Figure from NASA/JPL-Caltech)

Finally, Cassini mission will finish its life with the so-called **"Grand Finale"** mission (Edgington and Spilker, 2016), starting in late 2016. In this final and hazardous phase, Cassini will get extremely close to the planet rings, allowing Cassini to obtain unprecedented information and the closest images ever captured of Saturn's rings and clouds. At the times of this writing, it has performed several polar orbits passing through the narrow F gap and is now orbiting Saturn in high eccentricity orbits that at their closest approach pass between the planet and its closest ring. These extraordinary orbits will also allow to create detailed maps of Saturn's magnetic and gravity fields. After 22 such orbits, Cassini will fall into Saturn's atmosphere on September 15, 2017. Figure 2.3 shows Cassini orbits during the Grand Finale mission.

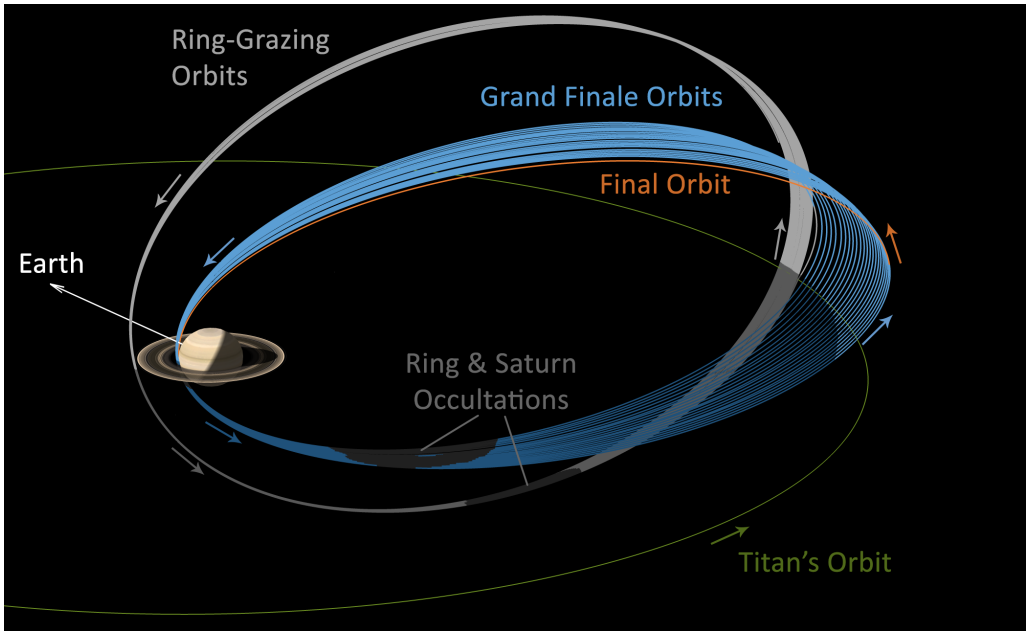

Figure 2.3: An illustration of Cassini's orbits during the Grand Finale. (Figure from NASA/JPL-Caltech)

In order to accomplish all these objectives, Cassini is equipped with 12 instruments, which can be divided in three different categories: (i) Optical remote sensing instruments, which study the Saturnian system in different regions of the electromagnetic spectrum; (ii) Microwave remote sensing instruments used to determine the mass of the moons and ring particles sizes and (iii) in situ instruments used to study the dust, plasma and magnetic field. Here we summarize the main characteristics of these instruments.

- **Composite Infrared Spectrometer (CIRS)** (Flasar et al., 2004). It is a Fourier Transform Spectrometer (FTS) that measures thermal radiation at wavelengths between 1 mm and 7 μm with spectral resolutions between 0.5 cm^{-1} and 15.5 cm^{-1}. It allows to retrieve 3D maps of temperature and gas composition from the upper troposphere to the upper stratosphere.

- **Visible and Infrared Mapping Spectrometer (VIMS)** (Brown et al., 2004). This imaging spectrometer is formed by two different cameras each of them providing images and spectra in different channels. One of them captures images in visible wavelengths from 0.35 μm to 1.07 μm, while the second captures images in infrared wavelengths between 0.85 μm and 5.1 μm. This instrument is designed to measure reflected and emitted radiation and therefore, determine the composition and thermal structure of Saturn's upper to middle troposphere.

- **Ultraviolet Imaging Spectrograph (UVIS)** (Esposito et al., 2004). This instrument consists of four telescopes that study Saturn's rings and atmosphere at ultraviolet wavelengths: (i) two medium-resolution camera-spectrographs,

which cover the ultraviolet wavelengths in two different channels (from 56 nm to 118 nm and between 110 nm and 190 nm); (ii) a sensitive High Speed Photometer (HSP) and (iii) a Hydrogen Deuterium Absorption Cell (HDAC). All of these instruments can perform simultaneous observations.

- **Imaging Science Subsystem (ISS)** (Porco et al., 2004). This instrument is formed by two high-resolution cameras: (i) the Wide Angle Camera (WAC) and (ii) the Narrow Angle Camera (NAC). They obtain high-resolution images at wavelengths between the ultraviolet ($\sim$ 260 nm) and the near-infrared ($\sim$ 1000 nm). We describe this instrument in greater detail in section 2.1.2.

- **Cassini Plasma Spectrometer (CAPS)** (Young et al., 2004). This spectrometer has three different sensors: (i) an Electron Spectrometer (ELS), which measures the flux of electrons; (ii) the Ion Beam Spectrometer (IBS), which measures the flux of positively charged ions and (iii) the Ion Mass Spectrometer (IMS), which measures the flux of positively charged atomic and molecular ions. The instrument is designed to analyze the composition, density, flow, velocity and temperature of Saturn's magnetosphere.

- **Cosmic Dust Analyzer (CDA)** (Srama et al., 2004). This instrument has two detectors that detect dust grains with masses between 10^{-19} and 10^{-9} kg. It is used to study both the interplanetary dust and dust in Saturn surrounding region.

- **Ion and Neutral Mass Spectrometer (INMS)** (Waite et al., 2004). This mass spectrometer is used to study the composition and structure of positively charged ions and neutral particles in Saturn's magnetosphere, rings and Titan's atmosphere.

- **Dual Technique Magnetometer (MAG)** (Dougherty et al., 2004). This instrument provides information of the direction and strength of the planet's magnetic field. It is mainly used to study Saturn's interior and magnetosphere, as well as, the interior of Saturn's satellites. It consists of a flux-gate magnetometer (FGM) and a vector helium magnetometer.

- **Magnetospheric Imaging Instrument (MIMI)** (Krimigis et al., 2004). This instrument images the neutral and charged particles of the magnetosphere and it also provides in-situ measurements of these populations. It is used to study the structure and dynamics of Saturn's magnetosphere and its interactions with Saturn's atmosphere, Titan and the icy-satellites.

- **Radio and Plasma Wave Science (RPWS)** (Gurnett et al., 2004). It is designed to study the radio emissions, plasma waves and dust in Saturn's magnetosphere, which give us information of the relationship between Saturn and its moons.

- **Radar** (Elachi et al., 2004). This is a multi-mode 13.8 GHz sensor that was built to study Titan surface. It sends radio waves to Titan's atmosphere and detects the reflected radio waves in order to provide information of Titan orography, such as lakes, mountains or dunes.

- **Radio Science Subsystem (RSS)** (Kliore et al., 2004). This subsystem has two different components, one of them mounted in Cassini and the other one on Earth. It is mainly used to study Saturn's atmosphere composition, Saturn's ring structure or Saturn's moons by analyzing the variation on the radio waves sent by the onboard system due to encounters with Saturn's atmosphere, rings or satellites.

2.1.2 Cassini ISS

This instrument is especially designed to investigate the three-dimensional cloud structure and meteorology of Saturn's and Titan's atmospheres and to determine the composition and structure of the rings system.

The instrument is formed by two parallel cameras attached to the main body of the spacecraft (Porco et al., 2004). One of the cameras, named the Narrow Angle Camera (NAC), is a reflecting telescope with a focal length of 2,000 mm ($f/10.5$) with a field of view (FOV) of $0.35° \times 0.35°$ and an image scale of ~ 6 μrad/pixel. The second camera is the Wide Angle Camera (WAC). This is a refractor telescope with a focal length ten times smaller than that of the NAC (200 mm or $f/3.5$) and with a field of view and image scale ten times larger ($3.5° \times 3.5°$ and ~ 60 μrad/pixel, respectively). Both cameras are able to capture images simultaneously, providing large sets of different resolution images of specific features.

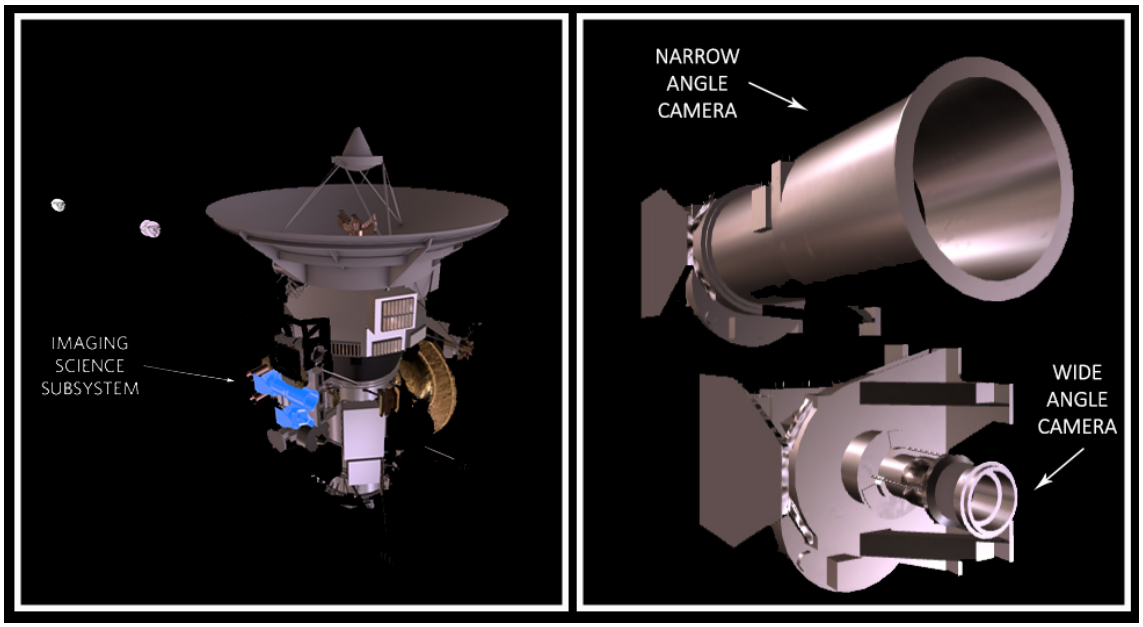

Figure 2.4: Location of the Imaging Science System (ISS) onboard Cassini orbiter (left) and the ISS instrument (right). (Figure from NASA JPL)

Both cameras have Charge-Coupled Device (CCD) detectors of 1024×1024 array of pixels, each pixel of 12 μm side. In addition, both cameras are provided with two

filter wheels that contain different filters. These wheels can be moved separately allowing multiple filter combinations. They can rotate up to two filters per second in the case of the WAC and three filters per second in the case of the NAC.

Filter	$\lambda_{\mathbf{eff,NAC}}$ ***(nm)***	$\lambda_{\mathbf{eff,WAC}}$ ***(nm)***
UV1	264	-
UV2	306	-
UV3	343	-
VIO	-	420
BL2	441	-
BL1	455	463
GRN	569	568
MT1	619	-
CB1	619	-
CB1a	635	-
CB1b	603	-
RED	649	647
HAL	656	656
MT2	727	728
CB2	750	752
IR1	750	740
IR2	861	852
MT3	889	890
CB3	938	939
IR3	928	917
IR4	1001	1000
IR5	-	1027
CL1	651	634
CL2	651	634
P0	633	-
P60	633	-
P120	633	-
IRP0	738	705
IRP90	-	705

Table 2.1: NAC and WAC filter characteristics. λ_{eff} represents the effective wavelength. (Porco et al., 2004)

The number of filters on these wheels is different for each camera. The narrow angle camera has 24 filters in total, 12 on each wheel. They range from the near-ultraviolet to the near-infrared, form 200 nm to 1100 nm. However, the wide angle camera carries 18 filters (9 on each wheel) covering spectral ranges from violet to near-infrared, from 420 nm to 1127 nm. Common filters mounted on both cameras are: (i) seven broad-band filters covering the spectral range from blue to near-infrared (BL1, GRN, RED, IR1, IR2, IR3 and IR4); (ii) two clear filters (CL1 and CL2); (iii) two methane absorption band filters (MT2 and MT3) and two continuum band filters (CB2 and CB3). These filters allow vertical sounding of the

atmosphere as different wavelengths sense different altitudes. Moreover, a narrow band $H\alpha$ filter (HAL) of 656 nm is also mounted on both cameras. Information of all filters is given in table 2.1.

These cameras provide images of the Saturnian system with the highest resolution achieved so far, and they can detect features as small as a few tens of kilometers. The highest image resolution of Saturn's polar regions used in this dissertation, a NAC image of the south polar vortex, has a resolution of 2.06 km/pixel. On the other hand, the highest resolution of a NAC image of the north polar region is 2.19 km/pixel. In the case of the WAC, the highest resolution of images showing the entire north and south polar regions are 44.0 km/pixel and 25.7 km/pixel, respectively.

2.2 Database

After a period of proprietary use of nine months to one year, Cassini ISS images are released to the scientific community and can be retrieved from NASA Planetary Data System (PDS). These images are published in volumes named Cassini Orbiter ISS (COISS) that contain all the information needed for the subsequent processing of the images, such as date and time, ephemerides, filters, target and all the necessary geometric information between the spacecraft and the planet. All this information is given in .IMG file extension and ASCII-formatted text labels files.

In order to visualize and select the desired image of a COISS, we use PVOL++ software (Hueso et al., 2010a) created by a student of our group. This software basically takes all the information from the complex COISS files and generates a simpler .xml file with the information included in both .IMG and ASCII-formatted text labels.

In this dissertation, we have used in total 87 images, covering dates from October 2006 to September 2014. Eleven of these images are used to study the south polar region, from November 2006 to December 2008, when the south hemisphere was illuminated by sunlight. The rest, 76 images, are analyzed to study the north polar region and the Hexagon from January 2009 to September 2014. Most of the images used, 60, are taken using CB2 or CB3 filters since those filters show the cloud morphology with the highest contrast. However, we also use images captured at other wavelengths in order to analyze the cloud morphology at different pressure levels: Twelve images were taken using red, green and blue color filters (4 images each), 10 with methane band filter (MT2) and 5 images with ultraviolet and violet filters (UV2, UV3 and VIO). A summary of all images used and their configurations is shown in Table 2.2.

COISS	*Year*	*Number of images*	*Filter*	*Resolution at the Pole (km/pixel)*	*Studied Region*
2026	2006	4	CB2	25.7 - 29.5	South
2047	2008	2	CB2, RED	2.06 - 2.4	South
2050	2008	5	CB2	77.1 - 103	South
2052	2009	5	CB2	83.2 - 91.0	North
2078	2012	8	CB2, MT2, RED, GRN, BL2, UV3	3.2 - 33.1	North
2080	2013	2	CB2	133.4 - 140.9	North
2081	2013	1	CB2	47.4	North
2083	2013	22	CB2, MT2, RED, GRN, BL2, UV3	4.21 - 77.1	North
2084	2013	10	CB2, CB3, MT2, VIO	182.0 - 184.0	North
2086	2013	4	CB2	~ 110	North
2088	2014	4	CB2	190.5 - 265.0	North
2090	2014	11	CB2, MT2, RED, GRN, BL2, UV3	~ 22	North
2091	2014	9	CB2, MT2, RED, GRN, BL2, UV2	~ 26	North

Table 2.2: Brief summary of the selected images for this study, their configuration and the studied region.

2.3 Calibration

ISS cameras, as every instrument, have several sources of noise (Porco et al., 2004; West et al., 2010). Some of the noise is introduced by (i) changes in the flat field produced by dust spec, which form artificial ring-like structures in the images; (ii) by radiation coming from the sensor and other components, which introduce thermal noise and (iii) the readout process and frequency of the CCD, which introduce coherent horizontal or vertical noise in the images. Thus, all images must be calibrated to remove this noise before making scientific measurements.

In order to calibrate ISS images, we use Cassini Imaging Science Subsystem Calibration software (CISSCAL) (Porco et al., 2004), which is a graphical interface written in the Interactive Data Language (IDL) that reads VICAR format files. This software performs the next steps: Converts the 8-bit images into 12-bit images, corrects the uneven bit-weighting, removes the coherent horizontal and vertical noise, the dust-rings, flat field and the thermal noise by subtracting the dark frames obtained with the shutter closed and the subtraction of the bias, corrects the non-linearity of the CCD response and converts the Data Numbers (DN) into flux units. In this last step we use the I/F option, which normalizes the image intensity with the solar flux on Saturn.

Examples of different noise and the respective calibrated images are shown in figure 2.5, where the left panels present Cassini ISS images before the calibration, displaying some common types of noise, such as coherent vertical noise, ring-like structures and white pixels, and images on the right show these images after calibration, with the noise corrected, showing the importance of image calibration on ISS images.

2.4 Navigation and Polar Projections

Once we select the images and calibrate them, we need to navigate them in order to give a value of latitude and longitude of the planet to each pixel of the image. We navigate ISS images using the Planetary Laboratory for Image Analysis (PLIA) (Hueso et al., 2010b), a software written in IDL.

Navigation is performed in two steps. Each point in the image is associated to a vector in space, with coordinates in the reference system of the camera, easily calculated once sample, line and focal distance are known. Then, the intersection of the prolongation of this vector with the ellipsoid of the planets is calculated. In order to do that, we need to know the distance between the spacecraft and the planet and rotate the camera coordinate system into the planet coordinate system by calculating the rotation matrix (Hueso et al., 2010b). Figure 2.6 illustrates the relationship between the two reference systems (Porco et al., 2004).

Plia software provides two different navigation subroutines. The first one, based in the VICAR code (implemented by C. Barnet), reads the ephemerides informa-

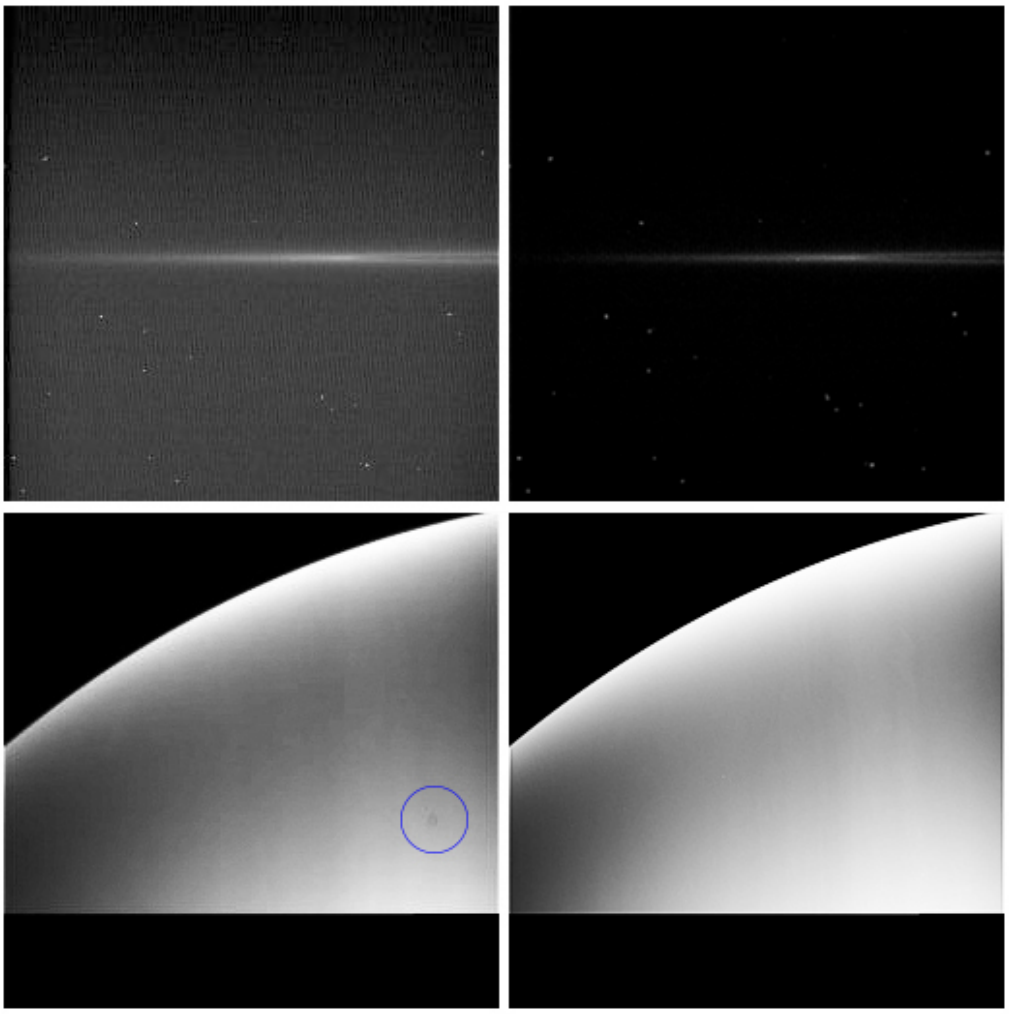

Figure 2.5: Two examples of noisy images before and after the calibration. The left panels show and ISS NAC raw images with horizontal and vertical coherence noise (top) and dust-ring noise (bottom) and the right panels show the same images after calibrating it with CISSCAL software.

tion stored at the image labels, in particular the distance to the planet center, and, in order to compute the rotation matrix, the North Azimuth Angle and the sub-spacecraft longitude and latitude (longitude and latitude that are beneath the spacecraft). The second subroutine uses the Spacecraft Planet Instrument C-matrix Event (SPICE) kernels (Acton, 1996) provided by NASA's Navigation and Ancillary Information Facility (NAIF) to compute those magnitudes and the rotation matrix. Most of images in this dissertation are navigated using the SPICE subroutine.

Small uncertainties on the time or position of Cassini, introduce significant error in the navigation. This error decreases with distance and thus, high-resolution images taken from a close distance to Saturn present larger navigation uncertainties. We have seen that in most cases, navigation uncertainties vary from one to few pixels in WAC high-resolution images, while for NAC it ranges between 10 and a

few tens of pixels.

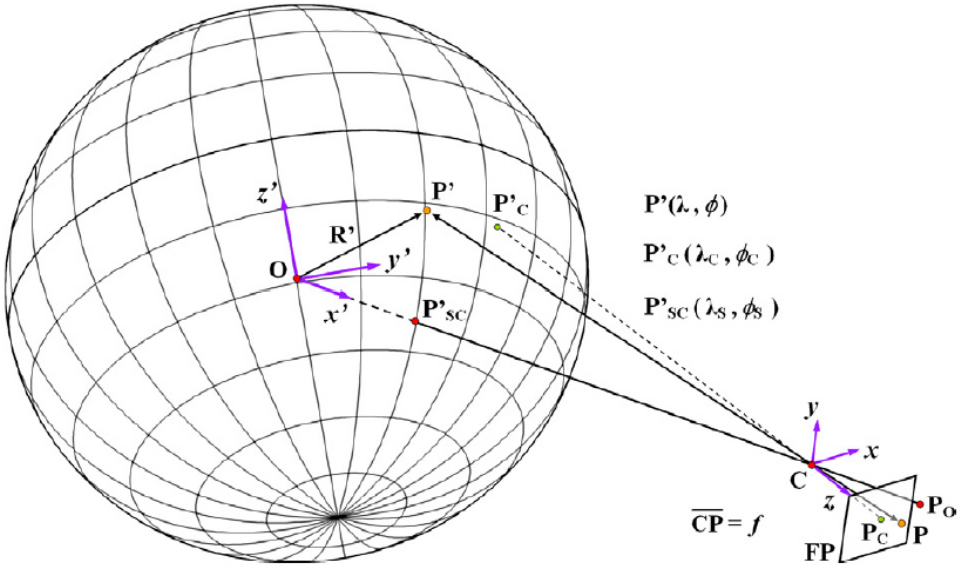

Figure 2.6: Geometry of the transformation between the coordinate system of the camera (X, Y, Z) and of the planet (X', Y', Z'). (Hueso et al., 2010b)

We use two different navigation correction techniques depending on the image. The first technique consists in fitting the limb or adjusting the position of the poles when they are visible in the images. However, in some images neither the limb nor the poles are visible or the adjustment of the pole is not trivial due to the high-resolution of the image, as happens often in NAC images. In these cases, we profit from the well known stability of zonal winds (García-Melendo et al., 2011) and we correct the navigation of image pairs manually by measuring the winds and adjusting by trial and error the navigation until the zonal wind profile of the region fits the well-known zonal velocity profile. We have applied this last navigation correction technique in all NAC and most of the WAC images used in this dissertation. Figure 2.7 illustrates how the inaccuracy of the navigation affects the retrieved zonal velocity profile and how a correction of the navigation can be performed this way.

Once the image is navigated, we polar project it onto a plane using the software PLIA. This software creates an azimuthally equidistant polar projection (Snyder, 1987), where all the meridians are equally spaced angularly and latitudes are equidistant concentric circles. This kind of projection distorts the image, with the pole at the center of the image being the only undistorted region, and therefore, it is adequate for the representation of high-latitudes. In our case, at the Hexagon's location ($\sim 75°$), the distortion introduced by this projection is around 1% in area, while at around 60° it increases up to 5% (Antuñano et al., 2015).

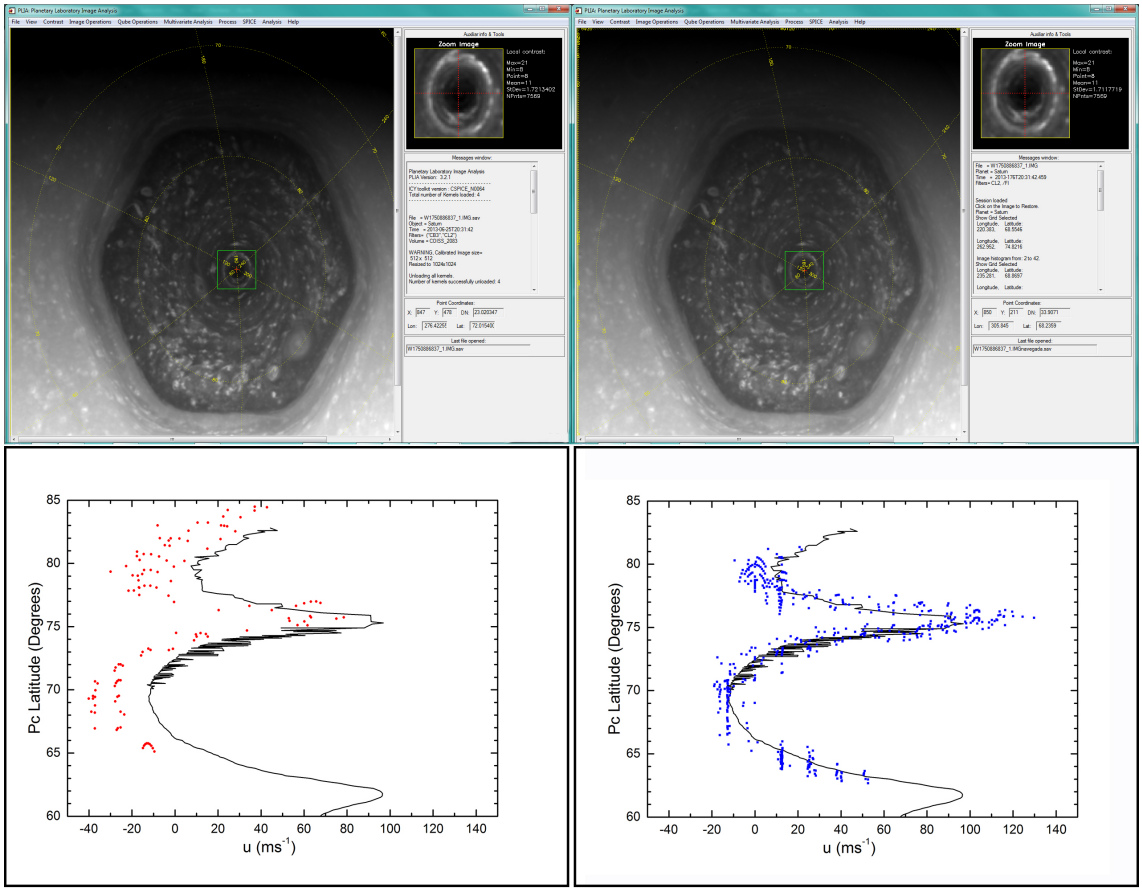

Figure 2.7: Top figures show the navigation without any corrections (left) and the corrected navigation (right). Bottom graphs show the zonal wind profiles obtained using wrong navigated image pairs (red dots, left) and image pairs with the navigation corrected 2 pixels in longitude (blue squares, rigth). The black solid lines represents the zonal wind profile from García-Melendo et al. (2011)

In this dissertation, we have built polar projections covering different latitudes and with different resolutions depending on the region under study. In order to analyze the cloud morphology and dynamics of the hexagon, its counterpart in the south, the singular vortices and the "puffy clouds" found at the north polar region, we have used polar projections from 60° (north and south) to the pole with meridional resolutions of 0.05 °/pixel and from 70°N to the pole with meridional resolution of 0.02 °/pixel. For the study of the north polar vortex, we build four polar projections with the aim of analyzing on the one hand, the polar vortex in great detail and on the other hand, the polar vortex together with its surroundings: (i) from 77° to the pole with meridional resolution of 0.01 °/pixel; (ii) from 85° to the pole with meridional resolution of 0.01 °/pixel, (iii) from 85° to the pole with meridional resolution of 0.005 °/pixel and (iv) from 87° to the pole with meridional resolution of 0.005 °/pixel. Finally, with the aim of studying the south polar vortex we have used polar projections from −85° to the pole with a meridional resolution of 0.02 °/pixel.

2.5 Wind Measurements

In order to obtain the horizontal wind structure, we assume that the small bright clouds behave as passive tracers following the wind flow. In this case, the velocity is obtained by measuring the difference in longitude and latitude of a feature over a known period of time. This way, we are able to compute its zonal and meridional velocities, using equation 2.1 and 2.2, respectively.

$$u = \frac{-2\pi R(\phi_{pc})\cos(\phi_{pc})}{360}\frac{\Delta\lambda}{\Delta t} \tag{2.1}$$

$$v = \frac{-2\pi R(\phi_{pc})}{360}\frac{\Delta\phi_{pc}}{\Delta t} \tag{2.2}$$

(Sánchez-Lavega, 2011), where $\Delta\lambda$ is the difference in longitude, ϕ_{pc} is the latitude (both $\Delta\lambda$ and ϕ_{pc} measured in degrees) and $R(\phi_{pc})$ is the radius of the planet at latitude ϕ_{pc}, defined by equation 2.3:

$$R(\phi_{pc}) = \frac{R_e R_p}{\sqrt{R_e^2 \sin^2\phi_{pc} + R_p^2 \cos^2\phi_{pc}}}. \tag{2.3}$$

In our case, we use the next useful approximation:

$$R(\phi_{pc}) = R_e\left(1 - f_{ep}\sin^2\phi_{pc}\right) \tag{2.4}$$

(Sánchez-Lavega, 2011), where $f_{ep} = \frac{(R_e - R_p)}{R_p}$ is the oblateness of the planet, where R_e and R_p are the equatorial and polar radius, respectively. In the case of Saturn the oblateness is 0.098. As mentioned in chapter 1, all winds in this dissertation are measured with respect to system III (τ = 10h 39min 24s or $\Omega = 810.7939°$/day).

The estimated error of these measurements depends mainly on the size of the pixel of each image (resolution of the image) and the time interval of the image pairs, and if no other error sources are present, the estimated minimum measurement uncertainty would be given by :

$$\sigma_u = \frac{Image\,resolution}{\Delta t} \tag{2.5}$$

Thus, higher resolution images and longer time intervals would, in principle, introduce smaller uncertainties. In our case, the estimated error is proportional to equation 2.5 since various errors introduce estimated uncertainties greater than a pixel. Here we provide a description of the errors introduced by different sources. The first source that we must take into account is the navigation error. As mentioned above, in images where the limb is not visible, which is the case of most of the studied images in this dissertation, we must adjust the navigation to the center of the polar vortex, where the estimated navigation uncertainty introduced is less

than two pixels in WAC images, but it could be as large as 20 pixels in high resolution NAC images (see figure 2.7). Another important source of error comes from the size of the boxes used in the correlation algorithm (described in section 2.5.2), where small boxes, which in principle minimize the error, could complicate the right identification of features. Finally, an identification error is also introduced in visual cloud tracking related to the pointing accuracy of the researcher and to the image resolution, as lower resolution images would introduce larger pointing errors. In our case, the uncertainty in pointing ranges between half a pixel and 2-3 pixels.

Overall, wind measurement uncertainties, taking into account all the described sources, is less than 10 $\mathrm{m\,s^{-1}}$ in most of the studied regions, except at the core of the Hexagon and the polar jets where uncertainties are of the order of $15-20$ $\mathrm{m\,s^{-1}}$.

In the next sections we describe two different velocity measurements techniques used in order to obtain the horizontal wind structure of Saturn's polar regions and their singular features.

2.5.1 Cloud Tracking

In this technique, the experimenter identifies visually features present in two or more images, and determines their longitude and latitude pointing manually to them. In general, this technique is preferably used in image pairs separated by one Saturnian rotation (~ 10 h) that show the same region of the planet. However, we must take into account that in some occasions the cloud morphology varies rapidly and long time intervals between images complicate the identification of features.

In our case, we have used this technique mainly to study the dynamics of the north and south polar vortex. At these latitudes, clouds move fast and vary significantly even in the time scale of minutes and thus, a time interval between images of 10 hours does not allow identification of features. Therefore, we have analyzed image pairs (mainly NAC images, but also some WAC images) separated by approximately 40-88 minutes, as larger time intervals complicate the identification of features and shorter time intervals introduce larger errors. Local movements of singular vortices and of the plume-like feature are also obtained by this method.

Finally, cloud tracking is specially interesting when a particular feature can be followed in a larger number of images over a longer period of time. In this case, the location (longitude and latitude) of a cloud feature is measured at different times and the velocity is deduced from equations 2.1 and 2.2, where the drift (degrees per unit time) can be deduced using a linear regression of all data. We have used this method to study the long-term displacements of singular vortices.

2.5.2 Bi-dimensional Brightness Correlation Algorithm

The second technique we use is a semi-automatic two-dimensional brightness correlation algorithm, implemented in the Particle Image Correlation Velocimetry (PICV2) (Hueso et al., 2009), written in IDL.

This software uses a pair of images and information about their time to return wind vectors by analyzing a region of the first image, using boxes of a chosen size and looking for an equivalent region in the second image. In order to find this equivalent region, the algorithm searches for a region where the correlation function is maximized. A very important characteristic of the algorithm is that it enables the user to compute the vectors semi-automatically by allowing the experimenter to ignore, correct or validate the proposed equivalent region. This is a necessary tool to compute wind vectors at the poles, where an automatic correlation algorithm introduces many spurious vectors due to rapid changes in the morphology.

The interfaces of this algorithm are shown in figure 2.8. The first interface displays the image pair, showing the selected region on the left image and drawing the wind vectors in the right image once they are obtained. For each wind measurement a second window is opened and this second interface is the validation window, where a bi-dimensional correlation map, the correlation factor and both the selected and the proposed equivalent regions are shown.

Due to the fast evolution of clouds, this algorithm is adequate for image pairs separated by $\sim$ 120 minutes or less. However, a more averaged wind profile could be also obtained using this algorithm in images separated by 10 h. Finally, since the algorithm work in polar projections and does not implement rotation of the features, the efficiency of this algorithm decreases at the polar vortices, where cloud rotations are significant.

In this dissertation we use this algorithm to obtain wind vectors in mainly WAC, but also in some NAC image pairs separated by less than 120 minutes with three different size boxes configuration:

- A correlation box of 23×23 pixels and 25×25 pixels in 0.05°/pixel meridional resolution polar projection (one pixel $\sim$ 50 km) from 60° north and south to the pole, respectively, with a search area on the correlation algorithm of 40×40 pixels in image pairs separated by $90 - 105$ minutes. This configuration is used in order to obtain the horizontal wind field of the north polar region (figures 3.4 and 3.5 in chapter 3).

- 50×50 pixels box in polar projections of meridional resolutions 0.01°/pixel (one pixel $\sim$ 10 km) and 0.02°/pixel (one pixel $\sim$ 20 km) from 85° to the pole north and south, respectively, with a search area of 80×80 pixels in image pairs separated by $40 - 88$ minutes, used to analyze the horizontal wind structure of the polar vortices (figures 3.4 and 3.5 in chapter 3).

- 50×50 pixels box in polar projections from 77°N to the pole of meridional

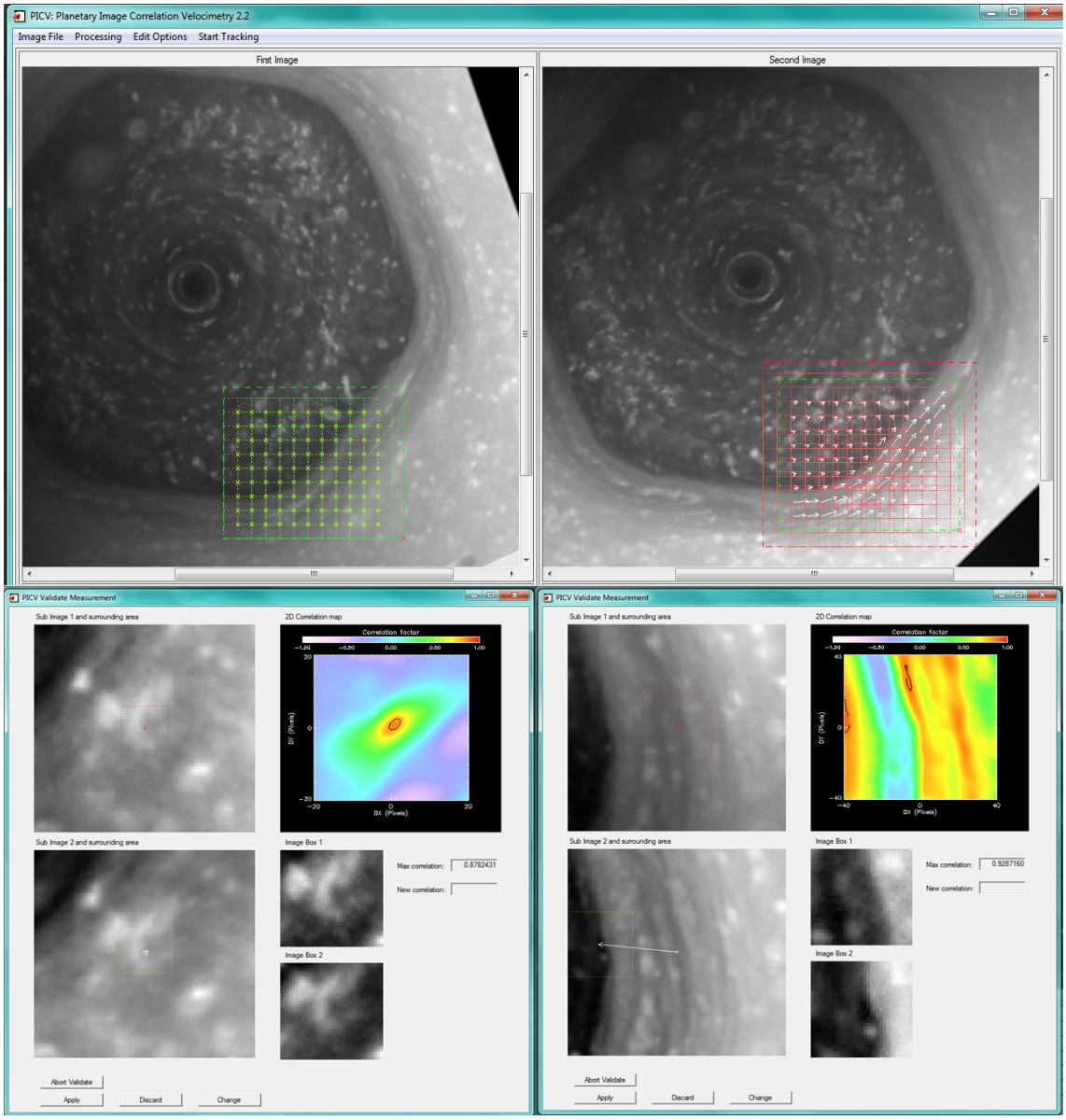

Figure 2.8: Screen-shots of the interface of the bi-dimensional brightness correlation software. Top figures shows the image pair that is being measured. The green box is the selected region by the experimenter. The small crosses represent the location of the wind measurements and the obtained wind vectors are shown with white arrows in the right image. Bottom figures shows a validation window for a well proposed correlation (left) and a spurious correlation (right).

resolution $0.01°/pixel$, with a search area of 80×80 pixels in images separated by $38-46$ minutes, in order to study the temporal variability of the horizontal wind field of the North Polar Vortex (figure 4.18 in chapter 4).

- 60×60 pixels boxes in $0.02°/pixel$ resolution polar projection from 70°N to the pole, with a search area of 80×80 pixels in images separated by $89-126$ minutes, used to study the dynamics of the plume-like feature inside the

hexagon jet (figures 4.6 in chapter 4).

The size of the boxes have been chosen to be large enough to allow the experimenter to validate the correlation, as too small boxes make visualization of the features difficult and introduce noise in the measurement. On the other hand, the larger the boxes, the fewer vectors are obtained, with the corresponding loss of information of small perturbations that may be present and thus, larger boxes lead to a more averaged wind field. Finally, the resolution of the winds presented in this dissertation is is related to half the side of the correlation box.

Chapter 3

Winds and Potential Vorticity in the Polar Regions

The polar regions of Giant Planets are singular in their dynamics as their behavior is highly conditioned by the rotation of the planet, since Coriolis force becomes specially important at high latitudes.

In particular, Saturn's polar regions display a large number of different cloud morphologies at cloud level, as shown in figure 3.1. The most remarkable feature, already mentioned in chapter 1, is the presence of a long-lived hexagonal wave that encloses a fast eastward jet. Moreover, there is a long-lived strong and stable polar vortex at each pole of the planet. Finally, unlike other latitudes, both polar regions are covered by bright compact clouds fields when observed at the continuum band wavelengths. All this features, and their temporal evolution and temporal variation will be studied in chapter 4.2.2. But in order to understand the general circulation on Saturn's atmosphere and how all these singular features originated, evolved and maintain at the polar regions, it is important to characterize first the general dynamics of these regions at cloud level.

This was not possible until the Voyager I and II captured the first high-resolution images of Saturn. Although the spacecrafts performed almost equatorial flybys, Godfrey (1988) was able to measure for the first time motions of clouds at the north polar region up to 84°N. These measurements showed the fast eastward jet of 120 ms^{-1} located at around 75°N enclosed by the hexagonal feature. After the Voyager flybys, further measurements on Saturn's polar regions had to wait until the Hubble Space Telescope (HST) imaged the south polar region between 1997 and 2002. Using these images, Sánchez-Lavega (2002a), obtained the first zonal wind measurements of this region up to 78°S and discovered a new eastward jet of around 100 $m\,s^{-1}$ at 70°S. Wind measurements of higher latitudes were performed using HST and Cassini ISS images from 2004, where Sánchez-Lavega et al. (2006) discovered a polar vortex with an intense eastward jet at around 88°S with a peak velocity of 160 $m\,s^{-1}$. Furthermore, during the first years of the Cassini mission, Dyudina et al. (2008) measured the zonal velocity of the South Polar Vortex using higher resolution images captured in October 2006. A year later, Baines et al.

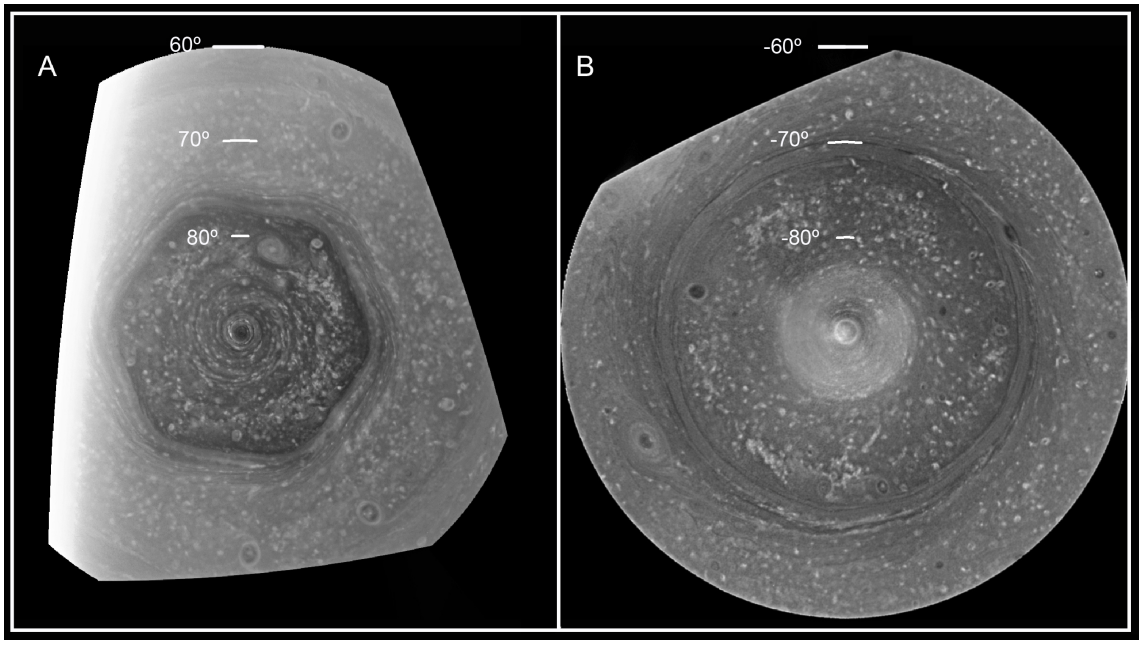

Figure 3.1: Two polar projection from 60° to 90° of the north polar region(a) and south polar region (b) captured with the Wide Angle Camera using CB2 filter on 14 June 2013 and 3 December 2008, respectively. (Figure from Antuñano et al. (2015))

(2009) found a similar polar vortex at the north polar region in VIMS images captured at 5 μm wavelength when this region was not yet illuminated by sunligth. After Saturn's equinox in 2009, the north polar region started to be illuminated and García-Melendo et al. (2011) updated Saturn's zonal wind profile up to 83°N and to 90°S in higher resolution, obtaining consistent results with previous measurements.

By relating the zonally averaged temperature profiles to the horizontal wind field, Read et al. (2009a) presented the first Ertel and quasi-geostrophic potential vorticity maps of Saturn's upper troposphere and upper stratosphere from 90°S to 80°N between 500 mbar and 1 mbar. In their study, they used the zonal mean profile of the north hemisphere from the voyagers flyby (Godfrey, 1988; Sánchez-Lavega et al., 2000) and of the south hemisphere from the HST and Cassini (Sánchez-Lavega, 2002a; Vasavada et al., 2006) and combined them with the temperature profiles retrieved from Cassini CIRS (Fletcher et al., 2007). Their results show a step-like variation with latitude in horizontal pressure surfaces from the upper troposphere to the upper stratosphere in both potential vorticities. Furthermore, they discovered that the the Rayleigh-Kuo stability criterion for a barotropic atmosphere and the Charney-Stern stability criterion for a baroclinic atmosphere were clearly violated at some latitudes.

Fletcher et al. (2016) compared the seasonal evolution of the quasi-geostrophic potential vorticity gradients for a third of a Saturnian year from the northern winter to northern spring (2004-2014) over all latitudes, finding that the potential vorticity gradients, and thus the potential vorticity, did not change at equatorial latitudes,

while a significant change was observed at mid latitudes, particularly at around 45°N, during the epoch under study.

In this study, we analyze the dynamics of both north and south polar regions, presenting zonal and meridional wind maps, zonal mean profiles and relative vorticity maps from June 2013 (north) and October 2006 and December 2008 (south). We present the two dimensional velocity field at cloud level of the north and south polar regions up to 89.9°N and 89.5°S, respectively, obtained using high-resolution images, in order to compare the horizontal dynamics of both polar regions at this level. Moreover, combining these results with the temperature profiles retrieved from CIRS data from June 2013 and December 2008 (Fletcher et al., 2015), we also present the zonally averaged Ertel potential vorticity maps up to the north pole, update both Ertel and quasi-geostrophic potential vorticity maps for both polar regions from 63.5° to the poles from the upper troposphere (500 mbar) to the upper stratosphere (1 mbar) and finally, we discuss the Rayleigh-Kuo and Charney-Stern stability criterion of these regions. This way, we complete the results of previous works extending measurements to regions closer to the pole and analyzing dynamical magnitudes at different Saturn's seasons.

3.1 Observations

In this study we use Cassini ISS WAC and NAC high-resolution images captured using continuum band filters, CB2 and CB3. From the vast number of available images, we searched for image pairs that cover the entire polar regions at similar epochs. In total 23 different images (7 NAC images of the polar vortices and 16 WAC images covering latitudes from at least 60° to the pole) are measured from four different epochs: (i) five WAC image pairs and two NAC image pairs from 14 and 25 June 2013, used to study the north polar region; (ii) four WAC image pairs from July 2008, (iii) four WAC pairs from December 2008 and (iv) two NAC image pairs from October 2006 used to analyze the south polar region. The maximum time interval between the two images of the WAC is 133 minutes, however, most image pairs are separated by $90 - 105$ minutes. In the case of the NAC images, pairs are separated by $40 - 88$ minutes. Table 3.1 summarizes the most relevant information of the images used.

All image pairs were measured using the semi-automatic brightness correlation software, validating, ignoring or changing each vector manually. Moreover, apart from this software, cloud tracking is also used in NAC images in order to verify the velocity obtained by the brightness correlation software and obtain extra vectors at the polar vortices, where the fast rotation of the features reduces the efficiency of the correlator.

In total we obtained 14,910 wind vectors for the north polar region and 7,925 for the south polar region. The distribution of measurements is irregular and in the best cases there are 600 vectors at the north polar region and 300 vectors at

COISS	*Date*	*Time*	*Camera*	*Filter*	*Resolution at the Pole (km/pixel)*	*Studied Region*
2026	11/10/2006	19:35:10	WAC	CB2	25.7	South
2026	11/10/2006	20:14:19	WAC	CB2	26.1	South
2026	11/10/2006	21:51:15	WAC	CB2	29.5	South
2026	11/10/2006	22:02:06	WAC	CB2	29.5	South
2047	14/07/2008	18:20:20	NAC	CB2	2.06	South
2047	14/07/2008	19:22:02	NAC	RED	2.40	South
2050	03/12/2008	18:09:09	WAC	CB2	77.1	South
2050	03/12/2008	19:43:09	WAC	CB2	83.2	South
2050	03/12/2008	21:17:10	WAC	CB2	90.0	South
2050	03/12/2008	22:51:10	WAC	CB2	98.0	South
2050	04/12/2008	00:25:10	WAC	CB2	103	South
2083	14/06/2013	08:36:26	NAC	CB2	5.27	North
2083	14/06/2013	09:56:33	NAC	CB3	11.0	North
2083	14/06/2013	12:06:55	NAC	CB2	5.83	North
2083	14/06/2013	12:47:41	NAC	CB3	11.9	North
2083	14/06/2013	08:36:26	WAC	CB2	52.7	North
2083	14/06/2013	10:02:00	WAC	CB2	55.1	North
2083	14/06/2013	14:58:03	WAC	CB2	64.2	North
2083	14/06/2013	16:23:37	WAC	CB2	66.5	North
2083	25/06/2013	20:31:39	WAC	CB3	86.0	North
2083	25/06/2013	22:43:45	WAC	CB2	44.0	North
2083	25/06/2013	22:44:33	WAC	CB3	88.1	North
2083	26/06/2013	00:57:21	WAC	CB3	91.4	North

Table 3.1: Selected images for this study, their configuration and the studied region.

the south in an area of $6,000$ km^2. This difference in the number of the total wind vectors and density between the north and south polar regions is due to the better viewing conditions of images of the north polar region. Figure 3.2 shows the density of wind vectors obtained at the north and south polar regions. The resolution of winds mentioned below is 0.5° between 60° and 85° north and south and 0.25° and 0.5° between 85° and 90° north and south, respectively.

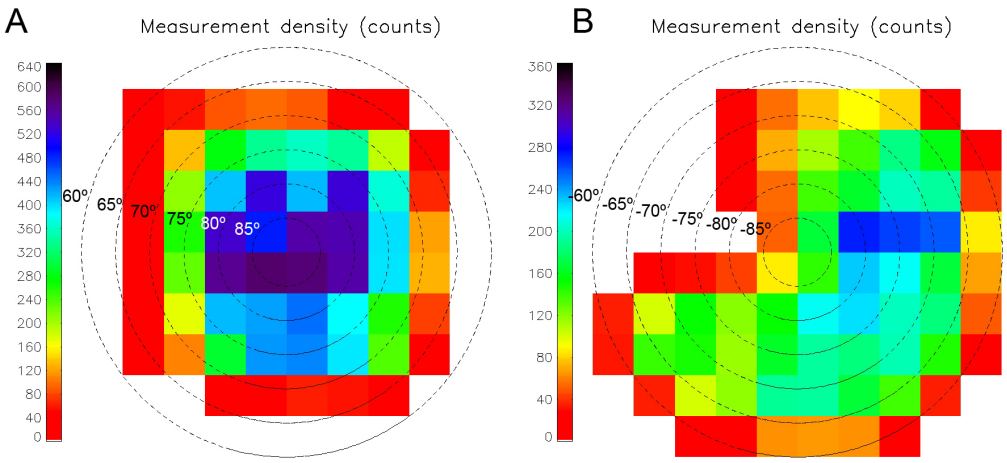

Figure 3.2: Measurement density maps of wind vectors, showing the number of vectors in 6° latitude square bins of the north polar regions (a) and the south (b). Note that the scale in both figures is different. (Figure from Antuñano et al. (2015))

It is important to mention that the results we present are obtained using all the data described here and therefore, as all measurements are not from the same exact date, the results shown are averaged wind velocities and vorticity. However, in the case of the two particular vortices located at 80.6°N and the South Polar Vortex (SPS) located at 66.1°S, wind vectors were measured in image pairs of a single day (14 June 2013 and 3 December 2008, respectively) and thus, wind velocities and vorticity of these two features are not averaged winds, but instantaneous winds.

The estimated error of individual measurements is $5 - 10$ m s^{-1} at most latitudes, except at the center of the eastward jets where the estimated error could be as large as $15 - 20$ m s^{-1}. A description of different error sources and the estimated uncertainties that they introduce in our wind measurements is given in chapter 2.5 .

3.2 Bi-dimensional Wind Velocities

The large density of measurements we obtained prevents the representation of individual vectors and their dimensions in a reasonably-size figure. With the aim of

achieving a clearer representation of the horizontal wind fields, we have interpolated our results into a regular grid, which allows us to represent the wind field at different resolutions.

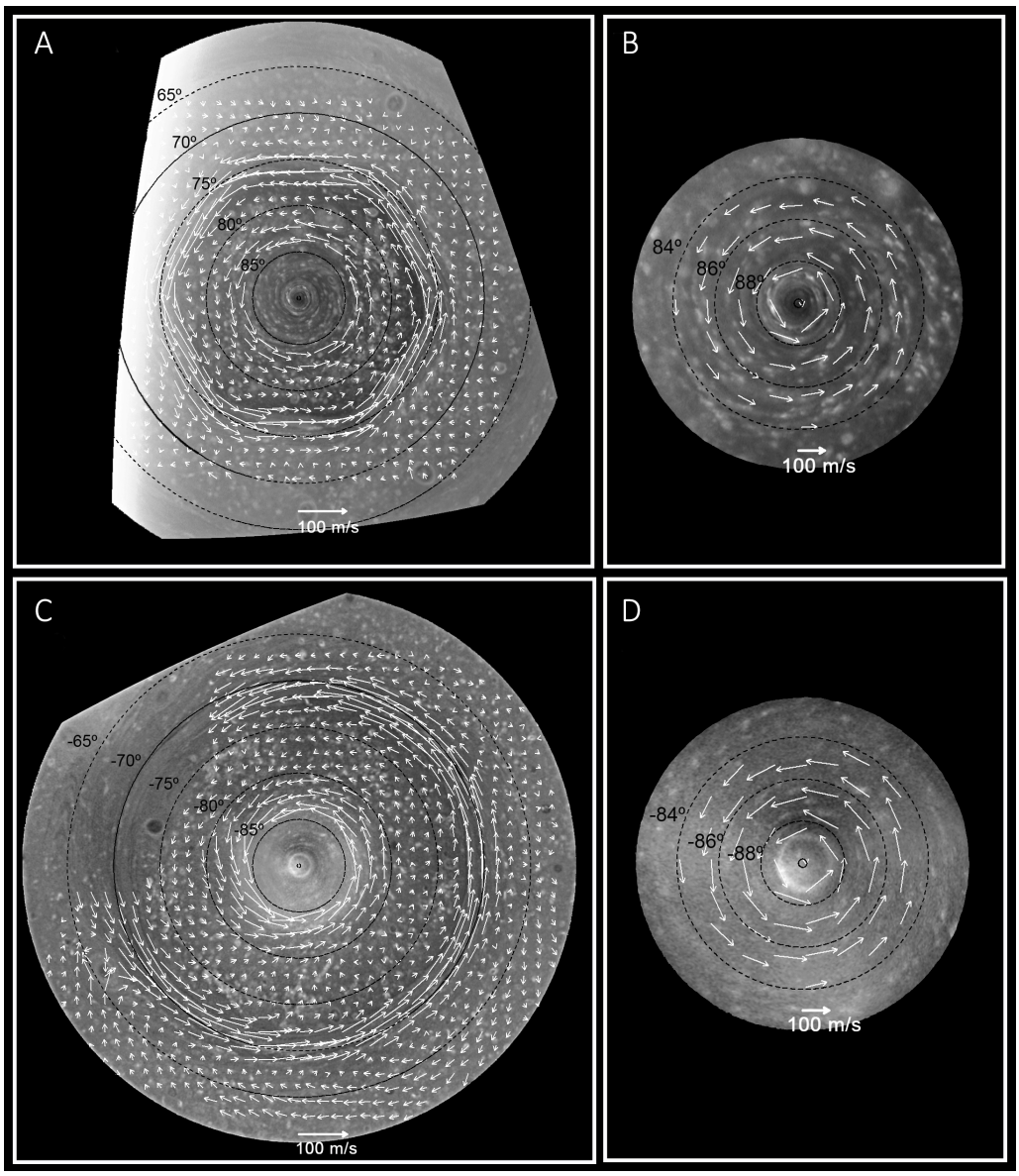

Figure 3.3: Averaged horizontal wind vectors at the north and south polar regions from 60° to 83° (a and c, respectively) and from 83° to 90° north (b) and south (d). Note the scale difference between left and right panels. (Figure from Antuñano et al. (2015)).

The singularity of spherical coordinates at the pole hinders the process of interpolation, and to overcome this difficulty, we introduce a new cartesian X-Y coordinate system in the plane of the polar projection, related to the spherical coordinates by

$$X = (90 - \phi)\cos\lambda \tag{3.1}$$

$$Y = (90 - \phi) \sin \lambda \tag{3.2}$$

(Garate-Lopez et al., 2013), where ϕ is the latitude and λ the longitude. Then we build a regular X-Y grid by interpolating our data, first using the Delaunay triangulation method in a 285 km X-Y grid (which corresponds to $\sim 0.3°$ in latitude) and then, evaluating the measured wind vectors in this new grid by a bi-linear interpolation. Finally, in order to obtain a smoothed wind field, we smooth the interpolated wind vectors on a spatial resolution of $\sim 1.2°$ in latitude (around $1,147$ km) using the nearest edge point method. The results are shown in figure 3.3, where only one every 25 vectors is plotted on top of a polar projection from 60° to the pole, north and south.

In this representation, the general horizontal circulation of the two polar regions can be seen clearly, showing a similar behavior at both hemispheres. Four intense eastward jets can be distinguished at different latitudes: (i) the hexagonal jet located at around 75.8°N, (ii) the strong polar jet at 88.5° (note the difference in the vector scale), (iii) an eastward jet at 70.4°S that does not depart from a pure zonal jet and (iv) another intense eastward jet at 88.5°S. In the north polar region, the meandering of the hexagonal jet is also clearly seen.

Focusing on the components of the wind field, zonal and meridional velocity contour maps can be obtained. We represent them in figure 3.4 and figure 3.5.

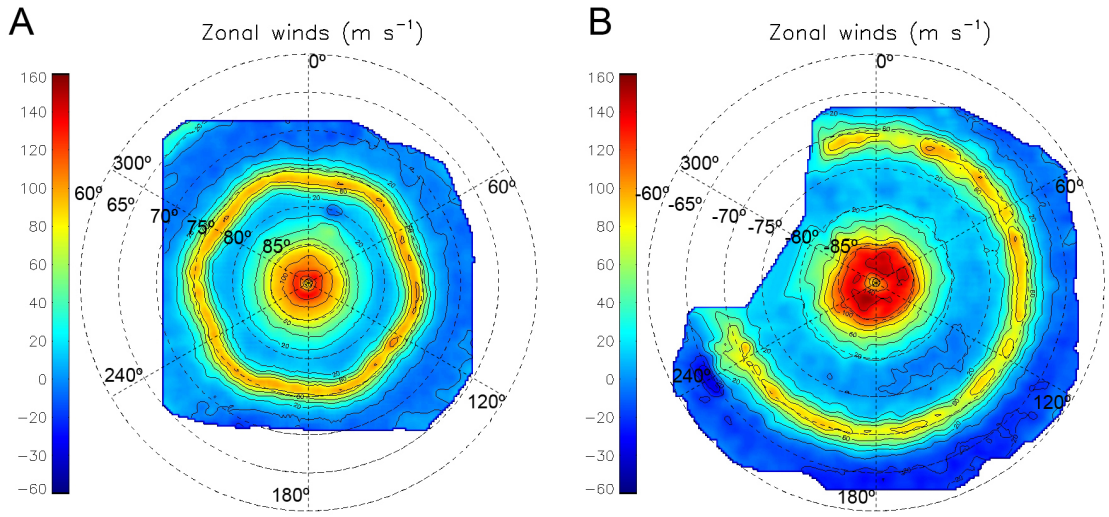

Figure 3.4: Zonal wind velocity map of the north (a) and south (b) polar regions. The zonal wind velocities mapped here are averaged over all epoch measured. (Figure from Antuñano et al. (2015))

Zonal wind velocity maps of the north and south polar regions show once again that the overall zonal winds in both regions are very similar. We see that the hexagonal eastward jet and the eastward jet at 70.4°S (which we will refer as the Hexagon's counterpart) reach average peak velocities of around 100 $\mathrm{m\,s^{-1}}$, while both polar jets are more intense, with average peak velocities of around 140 $\mathrm{m\,s^{-1}}$. However, some important differences are observed in these maps. The most notable one is the difference between the shape of the eastward jet enclosed by the Hexagon and that of the jet at 70.4°S, showing that while the eastward jet located at 75.8°N meanders in latitude, its counterpart does not depart from a zonal jet. Moreover, the difference in latitude (one is 5° closer to the pole than the other) is also significant. Finally, the south polar jet seems to be wider and faster than the one in the north.

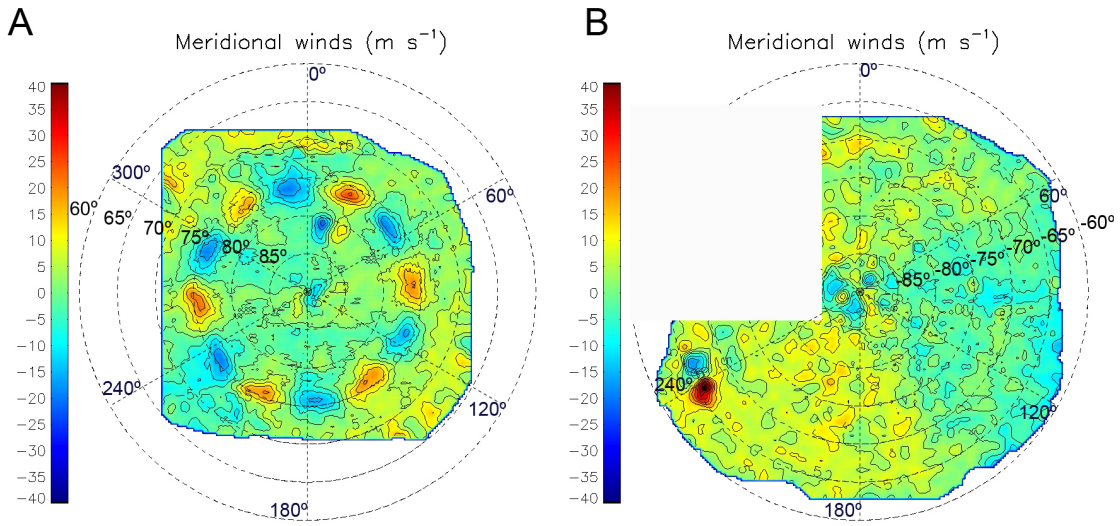

Figure 3.5: Meridional wind velocity map of the north (a) and south (b) polar regions. The meridional wind velocities mapped here are averaged over all epoch measured except for the vortex at 80°N and the South Polar Spot (SPS) at 66°S that were measured in a single day (14 June 2013 and 3 December 2008, respectively). (Figure from Antuñano et al. (2015))

Comparison of the meridional velocity maps of both polar regions reflects the differences due to the hexagonal jet. The red and blue blobs present in the north polar region are a signal of the meandering motion of the Hexagon jet, where positive values represent northward movements and negative values represent equatoward displacement. Gaps of zero meridional velocities between the red and blue blobs indicate the location of vertices and the center of the sides of the Hexagon, where the motion is essentially zonal. This distribution of meridional velocity reflects the motion, northward from a vertex to the center of the side and equatoward from there to the next vertex, with maximum meridional velocities of the order of ± 28 $\mathrm{m\,s^{-1}}$. However, in the south polar region there are no significant departures from zonal motion, as expected in a zonal jet. These maps show also the presence of two large anticyclones, located at 80.6°N and at 66.1°S (named the South Polar Spot (SPS)

due to the similarity to the North Polar Spot (NPS) described in chapter 1) with meridional velocities of 15 $\mathrm{m\,s^{-1}}$ and 35 $\mathrm{m\,s^{-1}}$, respectively. The estimated velocity error in these maps is of the order of 10 $\mathrm{m\,s^{-1}}$ and thus, the overall velocity gradient seen in the southern meridional velocity map is not significant.

3.3 Zonal Wind Profiles

We compute zonal mean velocity profiles of the north and south polar regions by averaging all the wind vectors at a particular latitudinal band. These averages are performed with different resolutions, due to the lower density of measured wind vectors in the south. In the case of the north polar region, we average winds in intervals of 0.2° latitude using moving bins of 0.4° for latitudes up to 89°N and in intervals of 0.1° with moving bins of 0.2° at higher latitudes. At the south, however, we average winds in intervals of 0.3° latitude using bins of 0.6° for latitudes between 60°S and 89°S and in intervals of 0.1° with moving bins of 0.2° at higher latitudes. We use moving bins in order to compute a smoother zonal wind profile as every vector lies in two different bins. These profiles are shown in figure 3.6.

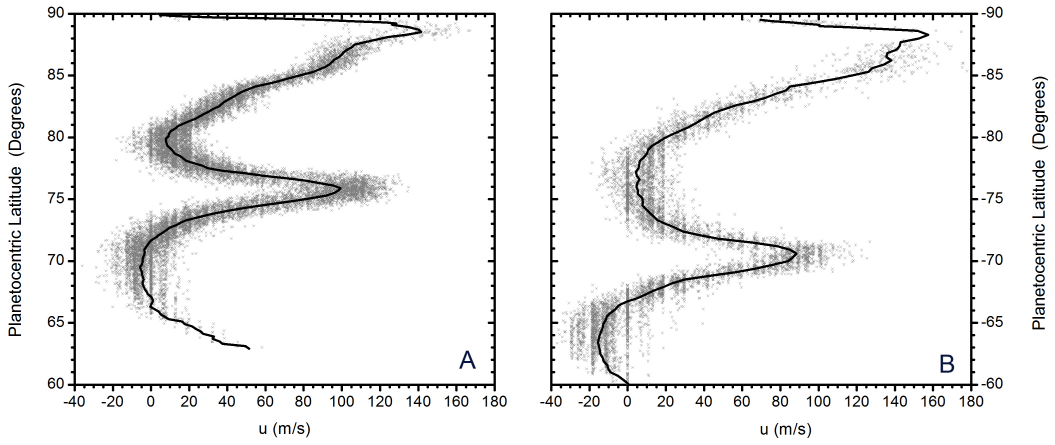

Figure 3.6: Zonal wind profiles (solid line) and all the measured zonal vectors (grey points) of the north (A) and south (B) polar regions. (Figure from Antuñano et al. (2015))

Consistently with the results in the previous section, the zonal wind profiles of both polar regions are very similar. These profiles show that the Hexagon jet reaches maximum velocities of $u = 104 \pm 15$ $\mathrm{m\,s^{-1}}$, while its counterpart in the south is slower, reaching peak velocities of $u = 87 \pm 20$ $\mathrm{m\,s^{-1}}$. The polar jets, which show a large asymmetry in shape, are more intense, reaching peak velocities of $u = 140 \pm 15$ $\mathrm{m\,s^{-1}}$ in the north and $u = 157 \pm 12$ $\mathrm{m\,s^{-1}}$ in the south. Although both polar jets reach their maximum velocity at the same latitude and decay in an

essentially linear way in their poleward flank, the southern polar jet is wider, with its Full Width at Half Maximum (FWHM) $5.9 \pm 0.1°$, $1.4°$ larger than the FWHM of the north polar jet. Moreover, the $5°$ difference in latitude of the quasi-symmetric hexagonal jet and its counterpart in the south is clearly seen in these zonal wind profiles.

The standard deviation in each latitudinal bin varies from less than 5 $\mathrm{m\,s^{-1}}$ for the westward jets to 20 $\mathrm{m\,s^{-1}}$ for the polar and the Hexagon jet. The large standard deviation at the polar jets is due to the small number of vectors obtained, because of the high variability of their cloud morphology. In the case of the Hexagon jet, the averaged zonal wind profile we present was obtained ignoring its meandering motion and as expected, this introduces a larger standard deviation. In next chapter (4), we show the zonal velocity profile of the Hexagon jet taking into account its meandering motion.

3.4 Vorticity and Vorticity Gradients

The vorticity describes the tendency of a fluid to rotate or spin due to its wind structure and it is an important magnitude in the understanding of the dynamics of a fluid. This magnitude is defined by the curl of the velocity:

$$\vec{\omega} = \bigtriangledown \times \vec{u} \tag{3.3}$$

(Sánchez-Lavega, 2011). In atmospheric science, we are concerned about the vertical component of this magnitude as it provides essential information on the rotation due to the horizontal motions of the flow. When calculated in the rotating system of the planet, it is called relative vorticity, and its vertical component is given in spherical coordinates by the following expression

$$\xi(\lambda, \phi) = \frac{1}{R(\phi)\cos\phi}\frac{\partial v}{\partial \lambda} - \frac{1}{R(\phi)}\frac{\partial u}{\partial \phi} + \frac{u}{R(\phi)}\tan\phi \tag{3.4}$$

where u and v are the zonal and meridional velocities, λ is the longitude, ϕ is the latitude and $R(\phi)$ is the planetary radius at that latitude (defined in 2.3). In this coordinates, relative vorticity presents a singularity at the pole, where the tangent of the latitude becomes infinite, making the last term of the relative vorticity equation (3.4), this is

$$\frac{u}{R}\tan(\phi) \tag{3.5}$$

usually ignored, relevant. In order to avoid this problem and to compute relative vorticity maps up to the poles, we use the "cartesian" coordinates defined in previous section. This introduces an error in the computation of the vorticity that becomes larger at lower latitudes. In our case, at the lowest latitude of $65°$, the

error is approximately of 1%. We then calculate the derivatives using finite differences in the interpolated and smoothed wind data obtained to compute the zonal and meridional velocity maps (see section 3.2), this time smoothing the vector field on a spatial resolution of 1.5° using the nearest edge point method. Figure 3.7 shows the relative vorticity maps of the north and south polar regions.

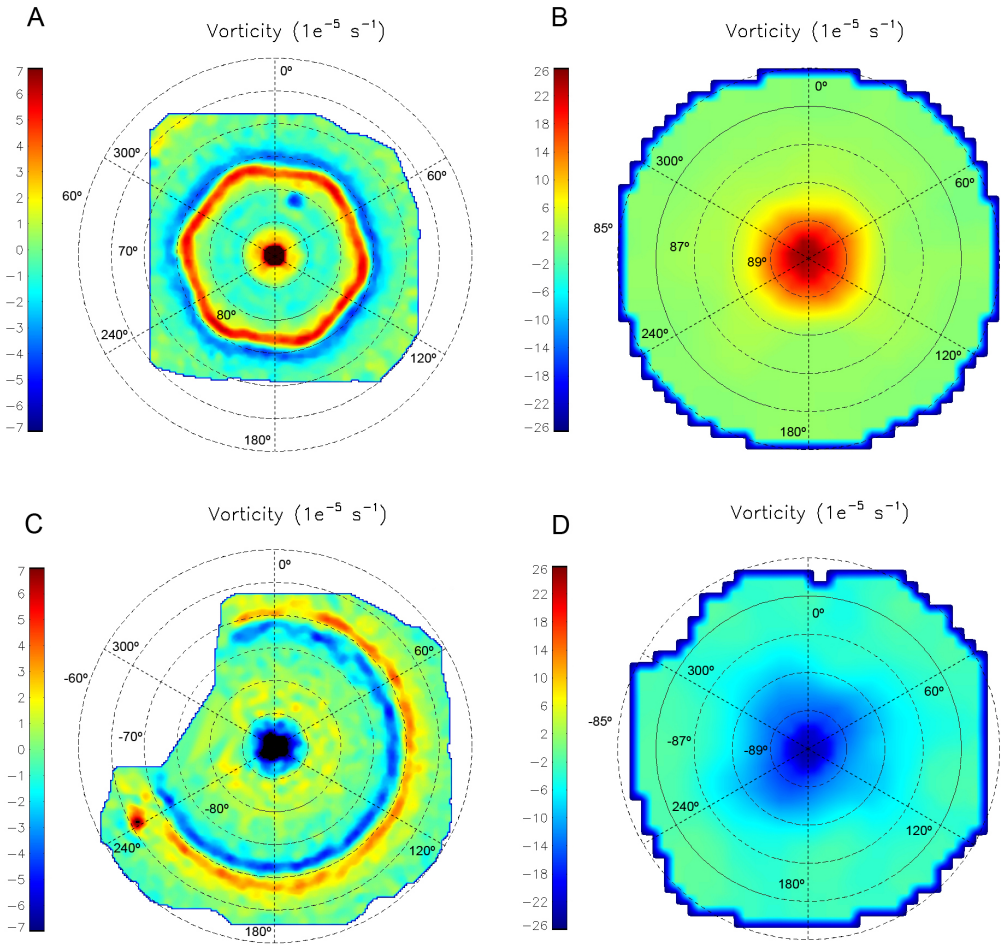

Figure 3.7: Vorticity maps of the north and south polar regions from 60° to the pole (A and C, respectively) and from 83° to the pole (B and D, respectively). The uncertainties on the relative vorticity, obtained by introducing random perturbations added to the horizontal winds, are of the order of $\sim 1 \times 10^{-5}$.

These maps show that the relative vorticity of both polar regions are very similar. In the case of the north polar region (figure 3.7a), the Hexagon is clearly observed as a jet stream of vorticity of $\sim \pm 6 \pm 1 \times 10^{-5}$ s^{-1} indicating that the Hexagon is not a vortex street (a series of spots of alternating vorticity on the flanks of the jets). Figure 3.7c, shows that the eastward jet at 70.4°S presents similar vorticity peak. The vorticity of these two jets is approximately 1/10th of the Coriolis parameter (defined as $f = 2\Omega \sin\phi$, where Ω is the planetary angular velocity and ϕ is the latitude). The polar cyclonic vortices present strong vorticity of around

$\sim 25 \pm 1 \times 10^{-5}$ s^{-1}, which is of the order of the Coriolis parameter at the poles, $|f| = 3.27 \times 10^{-4}$ s^{-1}. These vorticity maps show also the anticyclonic vortex at 80.6°N and the SPS at 66.1° with interpolated vorticity of -5 ± 1 x 10^{-5} s^{-1} and -7 ± 1 x 10^{-5} s^{-1}, respectively. The thick blue line around the vorticity map is an artifact in the outer boundary of our representation and does not represent real vorticity.

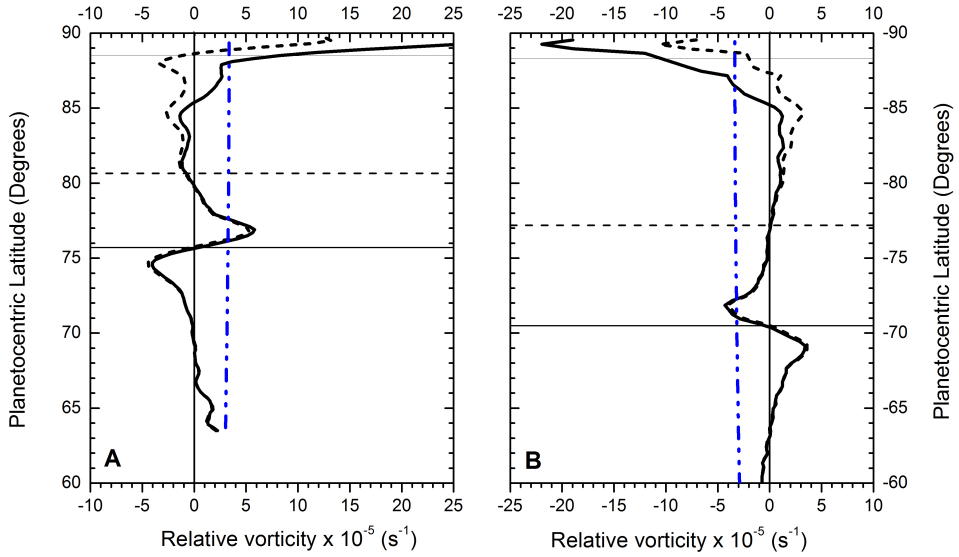

Figure 3.8: Meridional derivative of zonal velocity $-\partial\bar{u}/\partial y$ (black dashed line), meridional profile of relative vorticity (black solid line) and Coriolis parameter (blue dash-dotted line) for the north (A) and for the south (B) polar regions. The dashed horizontal line represents the peak of the westward jets, while the horizontal solid lines represent the location of the eastward jets.

Usually, at mid and equatorial latitudes the relative vorticity given in equation 3.4, is approximated to the meridional gradient of the zonal velocity, $-\partial u/\partial y$, due to the approximately zonal character of the flow outside singular vortices. However, even in zonal flows, this approximation of the relative vorticity is not valid at the poles, since the term 3.5 in equation 3.4 becomes important at latitudes higher than 80° and dominant for latitudes higher than 85°. The importance of the term 3.5 at high latitudes is shown in figure 3.8, where we compare the actual relative vorticity $-\partial u/\partial y + \frac{u}{R(\phi)} \tan\phi$ and the meridional gradient of the zonal velocity $-\partial u/\partial y$.

In the case of the jet associated to the Hexagon and the corresponding jet in the south at 70.4°S, the relative vorticity is clearly dominated by the meridional derivative of zonal velocity ($-\partial\bar{u}/\partial y$), which peak value is $\pm 5 \pm 1$ x 10^{-5} s^{-1} at the Hexagon and $\pm 4 \pm 1$ x 10^{-5} s^{-1} at its counterpart in the south and thus, the standard analysis usually applied to mid latitudes is still valid.

Finally, the meridional gradient of the vertical component of the vorticity is an

essential magnitude in the understanding of atmospheric dynamics as it provides information on the instability of the flow. In the case of a barotropic atmosphere, Rayleigh-Kuo criterion indicates that a necessary, but not sufficient, condition for a zonal jet to become unstable is that $\beta - \partial\bar{u}^2/\partial y^2 > 0$ (Sánchez-Lavega, 2011) at the studied domain. In order to analyze the instability of the jets of the polar regions, we compare the vorticity gradients and the planetary vorticity gradient, $\beta = df/dy = 2\Omega\cos\phi/R(\phi)$ (Sánchez-Lavega, 2011). The results are shown in figure 3.9, where we can appreciate that the β parameter is of the order of 1.5×10^{-12} $\mathrm{m^{-1}s^{-1}}$, two orders of magnitude smaller than the ambient vorticity at the Hexagon jet and its counterpart in the south. Furthermore, we see that the Rayleigh-Kuo criterion is satisfied at the two flanks of the Hexagon jet and of the eastward jet at 70.4°S.

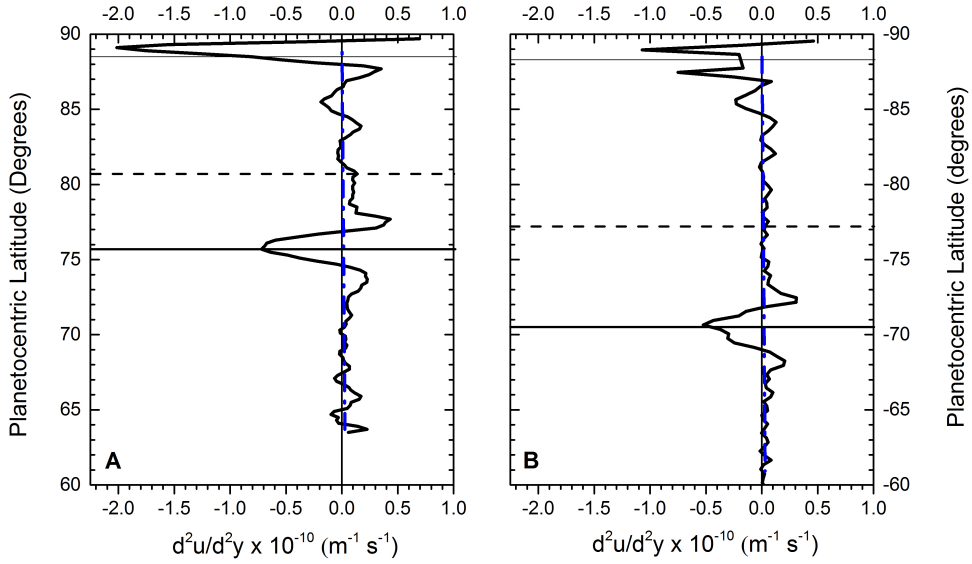

Figure 3.9: Vorticity gradients (black solid line) and β parameter (blue dashed line) for the north (A) and south (B) polar regions. Horizontal solid and dashed lines represents the peak of the eastward and westward jets, respectively.

3.5 Potential Vorticity and Potential Vorticity Gradients

Up to this point, we have concetrated on the dynamics at cloud level, without taking into account the vertical structure of the atmosphere. The relative vorticity described above is of particular importance as it is a basic ingredient of one of the most relevant dynamical magnitudes in the study of planetary atmospheres, the potential vorticity. Here, we consider two versions of this magnitude, the Ertel's potential vorticity (EPV) and the quasi-geostrophic potential vorticity (QGPV).

Other essential ingredient necessary to compute these potential vorticities, is the knowledge of the vertical temperature structure of the atmosphere. In our study we use the zonally averaged temperature profiles from December 2008 (southern summer) and June 2013 (northern spring) retrieved from CIRS data by Fletcher et al. (2015), which present maximum spatial resolutions of 2° latitude and a vertical resolution that varies with pressure, ranging from $1 - 10$ mbar at the stratosphere to $10 - 50$ mbar at the upper troposphere.

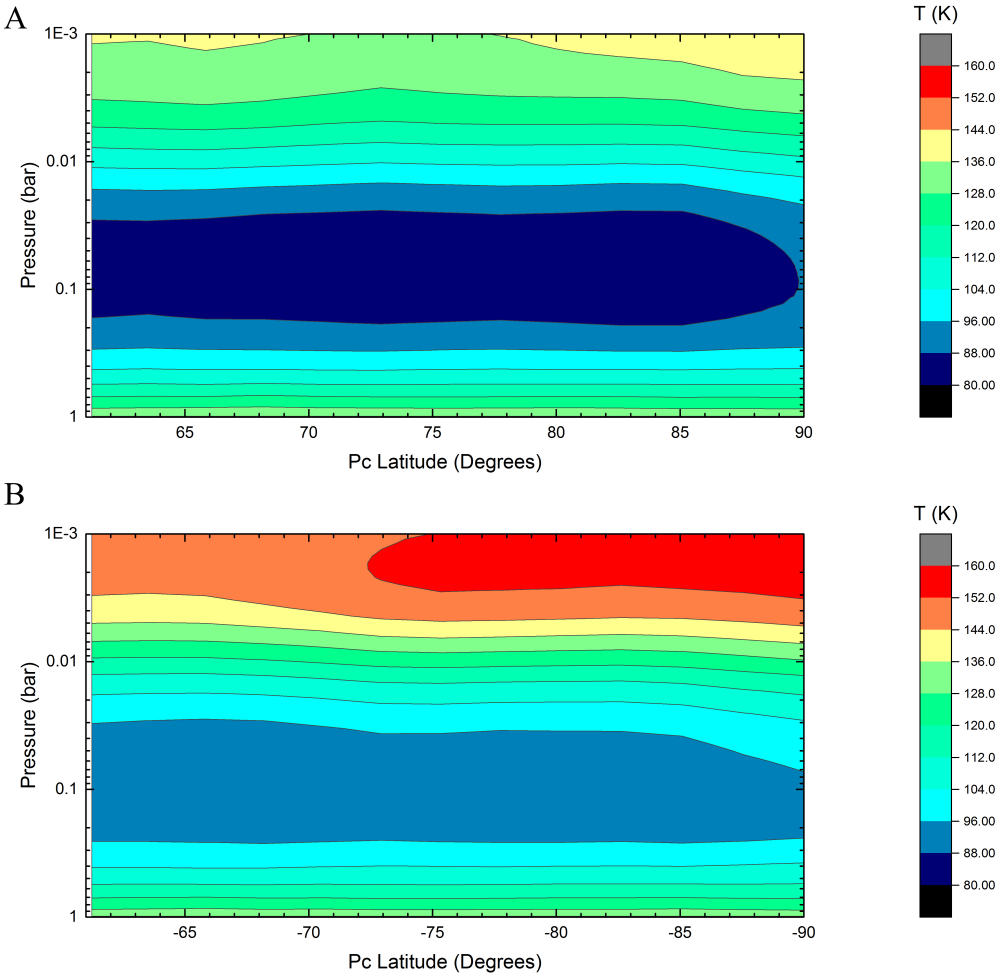

Figure 3.10: Zonal mean temperature maps from 61° to 90° for the north polar regions from June 2013 (A) and south polar regions from December 2008 (B). (Data obtained from Fletcher et al. (2015))

As it can be seen in figure 3.10, in both hemispheres the temperature at the upper troposphere between 1 bar and $\sim$ 100 mbar remains almost constant with latitude, within the estimated uncertainties, while at the stratosphere, the temperature increases slightly to the poles. In addition, above 600 mbar the south polar region seems to be warmer than the north polar region, this temperature difference ranging between less than 10 K at the upper troposphere to around 20 K at the upper stratosphere. This is probably due to seasonal differences between the north

and south polar regions at the epochs under study, as a long-term study of the temperatures (Fletcher et al., 2015) has shown that the north polar region is getting warmer as it approaches the summer. These maps do not show any special feature at the latitude of the Hexagon, nor any significant difference at those latitudes between the north and the south.

As the temperature data used in this study (Fletcher et al., 2015) is not obtained in a regular grid, all maps presented in these section are built creating a regular latitude-pressure grid of 21×21 points size by interpolating our data, first using a Delaunay triangulation method in 1.5° latitude $\times 1.4$ dB in $\log P/P_0$ pressure and then, evaluating the data in this new grid by a linear interpolation.

3.5.1 Zonally Averaged Ertel Potential Vorticity

Hoskins et al. (1985) demonstrated that a dynamical fluid can be described by the distribution of the isentropic potential vorticity and the mass under the isentropic surfaces. In a frictionless and adiabatic atmosphere, the change of absolute vorticity ($\omega = \xi_\theta + f$, where ξ_θ is the relative vorticity evaluated in an isentropic surface and f is the Coriolis parameter) is related to the change of the vertical gradient of isentropic surfaces ($\partial\theta/\partial P$, where θ is the potential temperature defined below and P is the pressure), that is, to the stratification of the flow. This relationship is given by the isentropic potential vorticity (or Ertel's potential vorticity), which is conserved ($dq_E/dt = 0$) under the mentioned conditions. Ertel potential vorticity is defined by

$$q_E = \frac{(2\mathbf{\Omega} + \nabla \times \mathbf{u}) \cdot \nabla\theta}{\rho} \simeq -g\,(f + \xi_\theta)\,\frac{\partial\theta}{\partial P} \tag{3.6}$$

(Sánchez-Lavega, 2011) where Ω is the planetary angular velocity, g is the gravity and ρ is the density.

In order to determine Ertel's potential vorticity at different levels of Saturn's polar atmosphere, we need to determine the potential temperature and its vertical gradient, and the relative vorticity at different heights.

The first two quantities will be deduced from the vertical temperature of Fletcher et al. (2015). On the other hand, since we do not have direct information about velocity at different heights, we will use the thermal wind equation to extrapolate the relative vorticity, measured at cloud level, to other heights.

Potential Temperature

The potential temperature determines the temperature of a parcel at pressure P and temperature T would have when moved to a reference pressure P_0 under adiabatic conditions (i.e. it does not heat or cool down). Assuming perfect gas law behavior and that the specific heat capacity depends only on pressure and density,

the potential temperature can be calculated as

$$\theta = T\left(\frac{P_0}{P}\right)^{R^*/C_p} \tag{3.7}$$

where R^* is the specific gas constant and c_p is the specific heat capacity at constant pressure. The specific gas constant in Saturn is $\frac{R}{\bar{\mu}} = 3.885\ \mathrm{Jg^{-1}K^{-1}}$, where $R = 8.3143\ \mathrm{Jmol^{-1}K^{-1}}$ is the ideal gas constant and $\bar{\mu} = 2.14\ \mathrm{g\,mol^{-1}}$ is the mean molecular weight of Saturn's atmosphere.

One issue in the case of the outer planets' atmospheres, is that the specific heat is not only a function of pressure and density, but it also depends on the hydrogen orto-para fraction and temperature, and therefore, 3.7 is not longer valid. In particular, we have used the so-called "normal" specific heat, which is a metastable distribution of hydrogen-helium with no orto-para exchange with the assumed mole-fraction of molecular hydrogen (H_2) of $X_{orto-H_2} = 0.75$ (Conrath and Gierasch, 1984). Following Epele et al. (2007), we can approximate the specific heat capacity in the range we are interested in by a series of powers in T, where the coefficients are empirically adjusted. In the case of Saturn's polar regions, we approximate the "normal" specific heat capacity between 80 K and 160 K by a third order polynomial:

$$C_p/R^* \sim A + B\,T + C\,T^2 + D\,T^3 \tag{3.8}$$

where A = 2.517755, B = $-0.006530\ \mathrm{K^{-1}}$, C = $1,195531 \times 10^{-4}\ \mathrm{K^{-2}}$ and D = $-3,504449 \times 10{-}7\mathrm{K^{-3}}$.

This temperature dependency of the specific heat capacity results in a more complex relation between the potential temperature of the adiabatic trajectory and the pressure level reference (Epele et al., 2007). However, one can define a new magnitude τ, with physical dimensions of temperature as

$$C_p(T)\,\frac{\delta T}{T} = C_p^0\,\frac{\delta \tau}{\tau} \tag{3.9}$$

(Epele et al., 2007), where the relation between T and τ is obtained by integration of 3.9:

$$\tau = T_0\left(\frac{T}{T_0}\right)^{A/C_p^0} \exp\left(\frac{B}{A}(T - T_0) + \frac{C}{2A}(T^2 - T_0^2) + \frac{D}{3A}(T^3 - T_0^3)\right). \tag{3.10}$$

This way, the problem can be treated in the same way as in the case of the ideal perfect gas, but using the "extended" potential temperature:

$$\tilde{\tau} = \tau\left(\frac{p}{p_0}\right)^{-\kappa^0} \tag{3.11}$$

(Epele et al., 2007), where $\kappa^0 = R^*/C_p^0$ with $C_p^0 = C_p(T_0)$ and $T_0 = \tau(T_0)$. In this study, we use $P_0 = 0.987$ bar and $T_0 = 134$ K as reference values.

The general definition of the potential vorticity states that in the case o a non-barotropic fluid θ could be any conserved scalar quantity that is a function of density and pressure only. Therefore, the new "extended" potential temperature $\tilde{\tau}$ can be safely used in the study of the potential vorticity and therefore, equation 3.6 becomes:

$$q_E \simeq -g\,(f + \xi_{\tilde{\tau}})\,\frac{\partial \tilde{\tau}}{\partial P}. \tag{3.12}$$

The "extended" potential temperature maps for Saturn's north and south polar regions from 63.5° to 90° retrieved by using the temperature maps of Fletcher et al. (2015) are shown in figure 3.11. As it can be noticed, the behavior of the potential temperature is similar at both polar regions, and isentropic surfaces essentially follow isobaric surfaces, with a rapid variation for pressures above 60 mbar. The potential temperatures reaches values of $\sim 1,400$ K and $\sim 1,550$ K at the upper stratosphere at ~ 1 mbar in the north and south, respectively, and decreases rapidly to ~ 230 K at around $50 - 60$ mbar in both polar regions. Below this altitude, the potential temperature varies more slowly, reaching ~ 130 K around 1 bar.

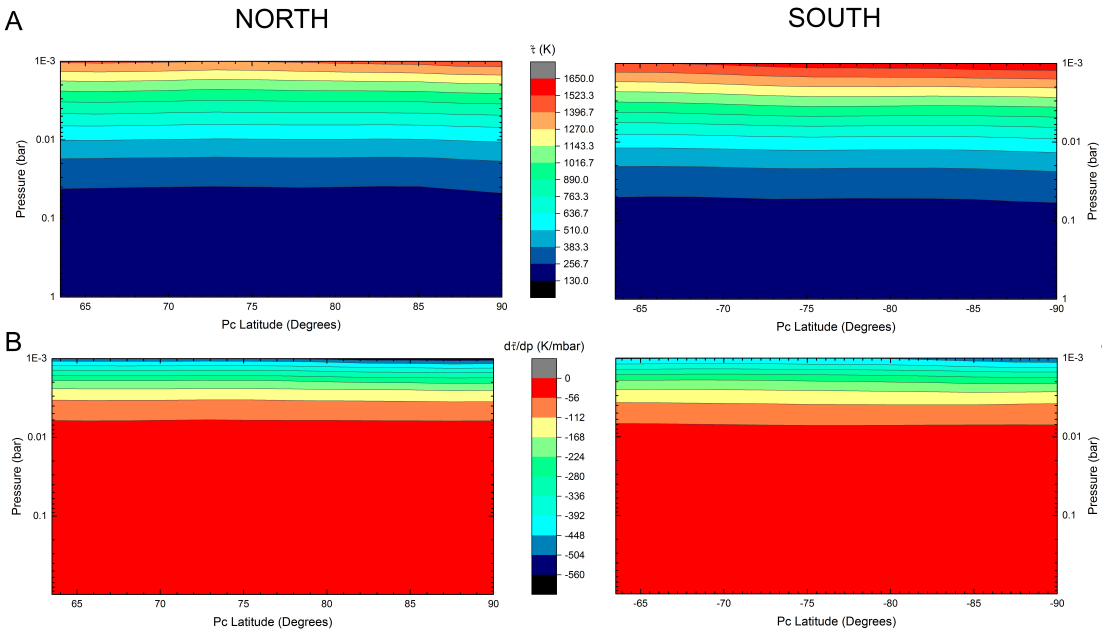

Figure 3.11: Zonal mean "extended" potential temperature maps from 63.5° to 90° (A) for the north polar regions from June 2013 (left) and south polar regions from December 2008 (right) and their vertical gradients (B).

The magnitude needed for the computation of potential vorticity (see equation 3.6) is the vertical gradient of "extended" potential temperature, which provides information on the static stability of the atmosphere (Sánchez-Lavega, 2011):

$$\frac{\mathrm{d}\tilde{\tau}}{\mathrm{d}P} < 0 \rightarrow \text{statically stable}$$
$$\frac{\mathrm{d}\tilde{\tau}}{\mathrm{d}P} = 0 \rightarrow \text{statically neutral}$$
$$\frac{\mathrm{d}\tilde{\tau}}{\mathrm{d}P} > 0 \rightarrow \text{statically unstable}$$

Figure 3.11b, shows a stratified and statically stable ($\frac{\mathrm{d}\tilde{\tau}}{\mathrm{d}P} < 0$) atmosphere in Saturn from the upper troposphere (500 mbar) to the upper stratosphere (1 mbar). The vertical gradient of potential temperature varies strongly with height, ranging from around $-560\ \mathrm{K\,mbar^{-1}}$ at the upper stratosphere to less than $-10\ \mathrm{K\,mbar^{-1}}$ at the upper troposphere and once again, we do not detect any special behavior at the latitude of the Hexagon.

Thermal Wind

In an atmosphere in hydrostatic and geostrophic balance, the vertical structure of the horizontal wind field is directly related to the horizontal temperature gradient by the so-called thermal wind equation,

$$\frac{\partial u}{\partial \ln(P)} = \frac{R^*}{f}\left(\frac{\partial T}{\partial y}\right) \tag{3.13}$$

(Sánchez-Lavega, 2011), where f is the Coriolis parameter $2\Omega \sin\phi$ and y is the meridional coordinate. Thus, from the knowledge of the pressure-latitude temperature profiles and the horizontal wind field at cloud level as a reference, the thermal zonal wind profile at different pressure levels can be deduced upon integrating equation 3.13. In our case, we assume that the cloud level at which we have measured the zonal and meridional velocities corresponds, at the polar regions, to a pressure level of 500 mbar ($\bar{\tilde{\tau}} = 137$ K) (Pérez-Hoyos et al., 2005; Sanz-Requena et al., 2017).

In order to obtain smooth distributions and evaluate the zonal wind profile with the same latitudinal resolution than the thermal structure, we have first binned the zonal wind profile in 0.5° latitude at the reference pressure level (500 mbar) and then, we have used values of the smoothed zonal wind profile separated by 2° latitude (maximum resolution of the zonally averaged temperature profiles). This smoothing of the zonal velocity profile, leads to slower zonal winds at the reference pressure and thus, to a smaller value of the relative vorticity than the one presented in the previous section.

Figure 3.12a and figure 3.13a, show the obtained zonally averaged vertical windshear of the north and south polar regions respectively, at different altitudes between 500 mbar and 1 mbar. The results show that at the troposphere (below

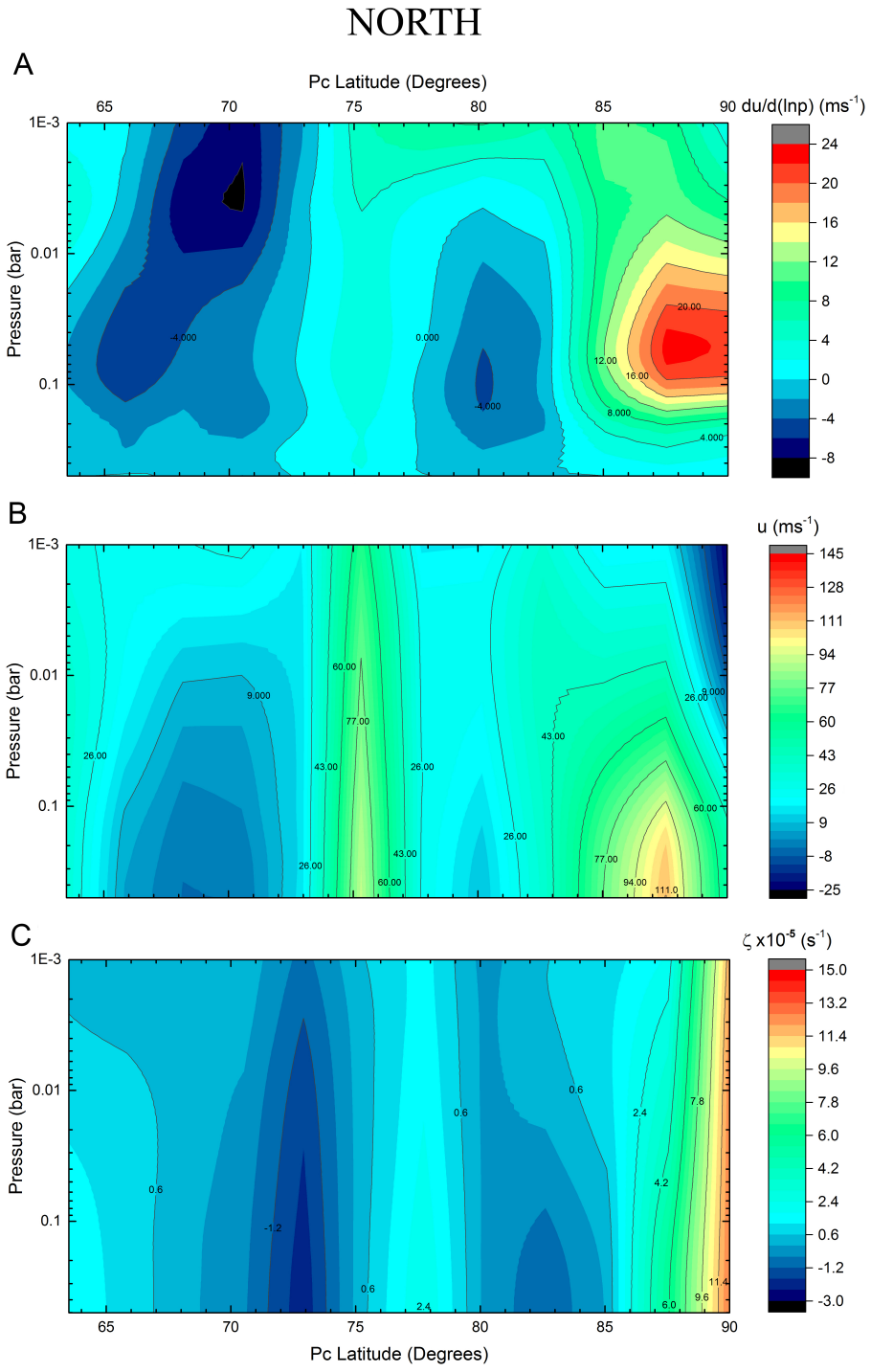

Figure 3.12: Pressure-latitude thermal wind maps (A), integrated zonal mean velocity maps (B) and relative vorticity maps (C) from 63.5° to the pole for the north polar region for June 2013.

100 mbar), both polar regions present a very small vertical wind shear, raging from $|\frac{du}{d\ln(p)}| = 4$ m s^{-1} to $|\frac{du}{d\ln(p)}| = -4$ m s^{-1} ($du/dz \sim \pm 0.1$ m s^{-1}/km, assuming a mean

scale height of $H \sim 40$ km) between 63.5° and 85° and between twice to three times that value at higher latitudes, while at the stratosphere the vertical wind shear reaches values of around $|\frac{du}{d\ln(p)}| = 15\ \mathrm{m\,s^{-1}}$ ($du/dz \sim -0.37\ \mathrm{m\,s^{-1}/km}$) or less at the south polar region and a maximum of $|\frac{du}{d\ln(p)}| = 24\ \mathrm{m\,s^{-1}}$ ($du/dz \sim -0.6\ \mathrm{m\,s^{-1}/km}$) at the north. This is a consequence of the fact that at the troposphere the atmosphere is nearly barotropic at latitudes equatoward 85°, while it becomes more baroclinic at the poles (latitudes higher than 85°) and at the stratosphere, as shown in figures 3.12b and figure 3.13b. In addition, overall, westward jets present positive vertical wind-shear (the zonal velocity of the jets becomes less negative with altitude), while eastward jets have negative wind-shear (they become slower with altitude).

Once we know the behavior of the vertical gradient of the potential temperature and the wind-shear over the region under study, we need to compute the relative vorticity maps in isentropic surfaces. However, for atmospheres with large Richardson number, $Ri = N^2/(\partial u/\partial z)^2$ (where $N^2 = \frac{g}{T}\left(-\frac{P}{H}\frac{dT}{dP} + \frac{g}{C_P}\right)$ is the Brunt-Väisälä frequency and $H = R^*T/g$ is the scale height), the relative vorticity evaluated in pressure surfaces can be safely used. At Saturn's polar regions, $Ri \sim 10^5$ and therefore, we can compute the relative vorticity using equation 3.4 and then, interpolate it into zonal mean constant potential temperature surfaces.

However, as mentioned in the previous section, the term 3.5 in 3.4 has a singularity at the pole and it cannot be ignored at latitudes above 80°. Therefore, we use equation 3.4 between 63.5° and 88.5°, where we do not find any singularity. At higher latitudes, we deal with the singularity in 3.5 by writing it in terms of the colatitude and using the fact that at those very high latitudes, the zonal velocity is approximately proportional to the colatitude

$$\frac{u}{R}\tan(\phi) = \frac{1}{R}\frac{a(\pi/2-\phi)}{\tan(\pi/2-\phi)} \sim -\frac{a}{R} \tag{3.14}$$

where a is the slope of the zonal velocity profile between 90° and 88.5° north ($a = 5345.7\ \mathrm{m\,s^{-1}rad^{-1}}$) and south ($a = 6113.5\ \mathrm{m\,s^{-1}rad^{-1}}$) and R is the radius of Saturn at those latitudes. The results are shown in figure 3.12c and figure 3.13c, where it can be observed that the values of the relative vorticity at cloud level are smaller than the ones presented in the previous section, as expected from the smoothing of the winds.

Zonally Averaged Ertel Potential Vorticity: Results

In order to compute the Ertel potential vorticity, we interpolate the obtained relative vorticity, using spline interpolation (we have checked that a linear interpolation gives identical results), in surfaces of meridionally averaged potential temperature. Finally, as $d\tilde{\tau}/dP$ varies strongly with height and in order to be able to compare the Ertel potential vorticity and the quasi-geostrophic potential vorticity, we fol-

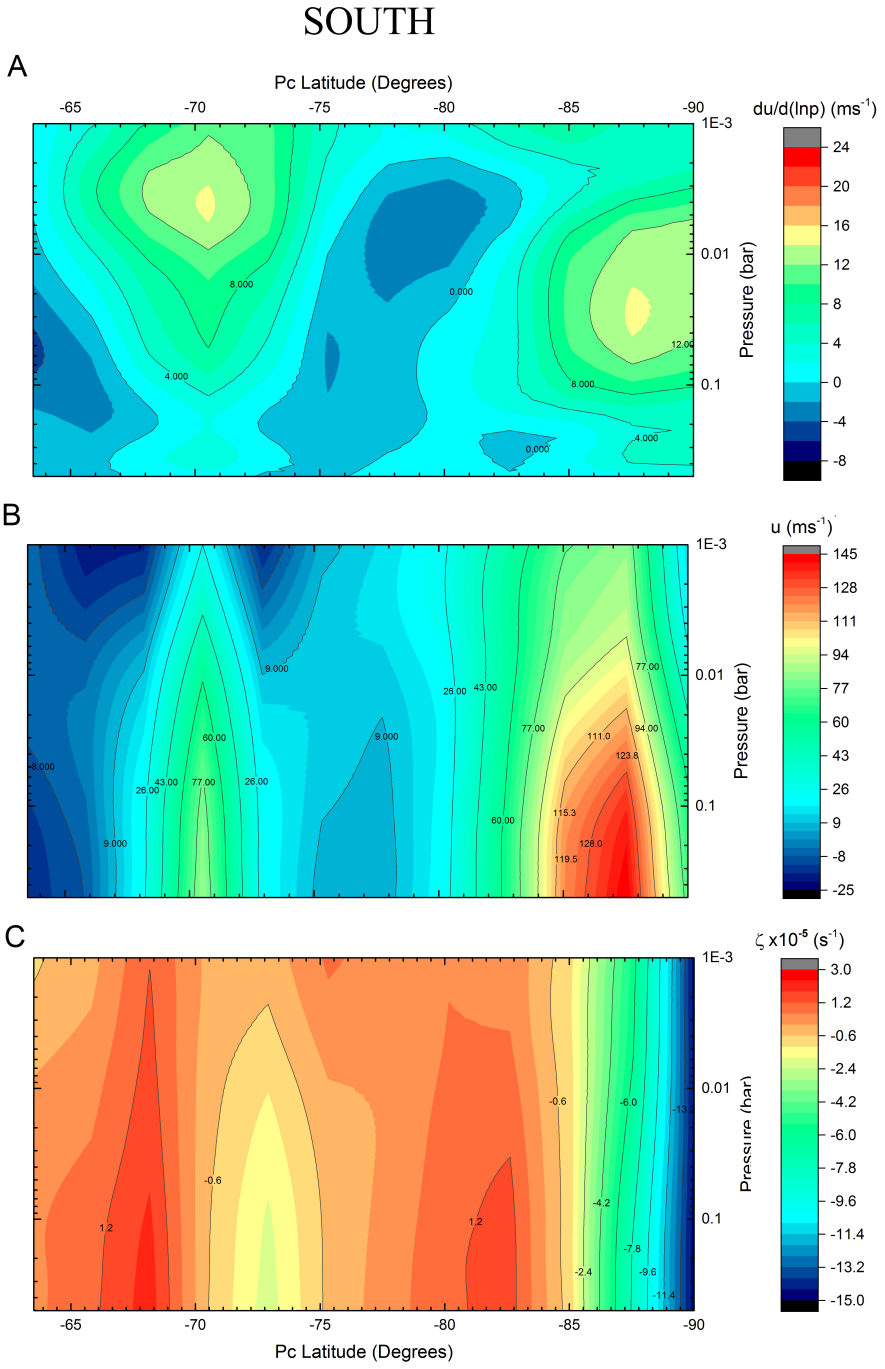

Figure 3.13: Pressure-latitude thermal wind maps (A), integrated zonal mean velocity maps (B) and relative vorticity maps (C) from 63.5° to the pole for the south polar region for December 2008.

low Read et al. (2009b) in normalizing the zonal mean Ertel potential vorticity by dividing it by $-g < d\tilde{\tau}/dp >$, where <> indicate the horizontal mean value on area-weighting for all latitudes.

The results are shown in figure 3.14, where the normalized Ertel potential vorticity (q_E), which now has the same units as relative vorticity, is represented for Saturn's north and south polar regions. These maps show that at all levels EPV presents negative values at the south polar region and positive values at the north, instead of following the sign of the relative vorticity. This is due to the dominance of the Coriolis parameter (f), which is everywhere an order of magnitude larger than the smoothed relative vorticity, but at the pole, where the relative vorticity is of the order of magnitude of f. Overall, the south polar region presents larger absolute values of the normalized potential vorticity, ranging from -2.7×10^{-4} s^{-1} to -7.5×10^{-4} s^{-1} at the south and from 1.9×10^{-4} s^{-1} to 5.0×10^{-4} s^{-1} at the north. The maximum absolute value of the Ertel potential vorticity is obtained at around the pole and $\tilde{\tau} \sim 100 - 200$ K in both hemispheres.

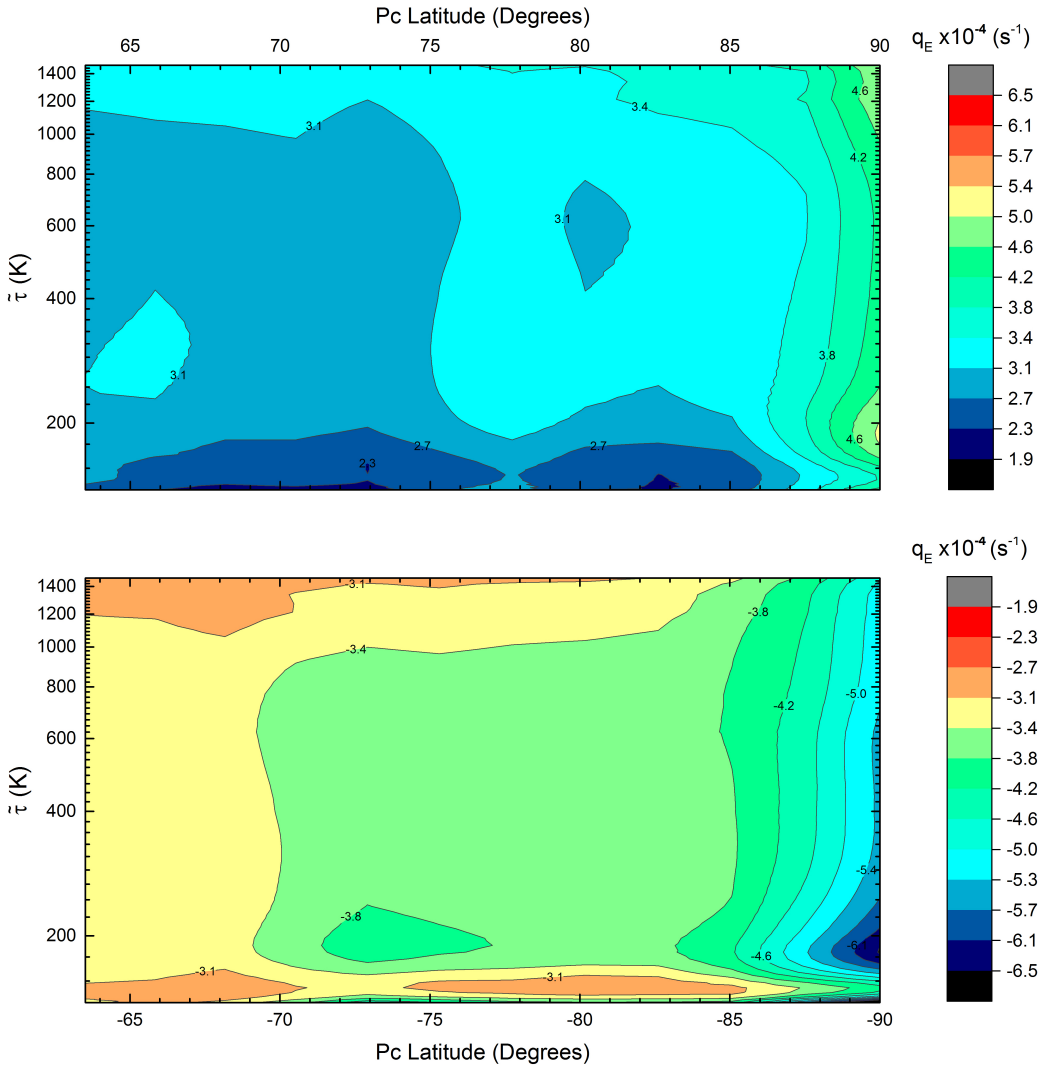

Figure 3.14: Normalized and zonally averaged Ertel potential vorticity maps from 63.5° to the pole for the north polar region for June 2013 (top) and south polar region for December 2008 (bottom).

Meridional gradients of the normalized Ertel potential vorticity provide information of the stability of the flow. Seasonal variations on the meridional gradients of the Ertel potential vorticity, and therefore on the stability of the flow, must come from seasonal changes in the thermal structure at the upper troposphere and lower stratosphere since, in the case of Saturn, it has been shown that the zonal jets have remained unchanged over the last 35 years. Computed meridional gradients of the normalized Ertel potential vorticity for the northern spring and southern summer (June 2013 and October/December 2008, respectively) are shown in figure 3.15. The results indicate that at the studied epochs, dq_E/dy changes sign, indicating that thermodynamic instability could develop, at the flanks of the Hexagon and the eastward jet at 70.4°S, as well as at the flank equatoward the peak velocity of the polar vortices. The changes on the sign of dq_E/dy are stronger at the lower flank of both north and south polar jets below 200 K, indicating that these jets are more unstable at this region.

Although these results show the general behavior of the approximated Ertel potential vorticity and its meridional gradient, it is important to note that these values should be taken with caution, as these magnitudes depend on differentiated velocity and temperature fields and therefore, propagation of the measurement uncertainties on the horizontal wind field and on the retrieved zonally averaged temperature must be taken into account. This is not a trivial task, first of all because errors in different variables are correlated and secondly, because of the uncertainties related to numerical differentiation.

3.5.2 Quasi-Geostrophic Potential Vorticity

The quasi-geostrophic potential vorticity is a valid approximation of the potential vorticity in rapid rotating fluids, where the wind can be approximated to the geostrophic wind, and it is obtained by linearizing the Ertel potential vorticity (equation 3.6) by assuming a linear perturbation on the temperature

$$T = T_s(P) + T_d(\lambda, \phi, P, t) \tag{3.15}$$

where T_s is the horizontal mean temperature (Pedlosky, 1987) and introducing the geostrophic wind in the equation of motion. The quasi-geostrophic potential vorticity is given by

$$q_g = (f + \zeta_g) - f \frac{\partial}{\partial p} \left(\frac{1}{s^2} \frac{d\theta}{dP} \right) \tag{3.16}$$

(Vallis, 2006), where $d\theta/dP = -RT_d/P$ is the geopotential and $s(p)$ is the static stability defined as

$$s^2 = -\frac{1}{\rho\theta} \frac{d\theta_0}{dP} \tag{3.17}$$

where $\theta_0(P)$ is a reference profile of the potential temperature and $\rho = P/(R^*T)$ is the density.

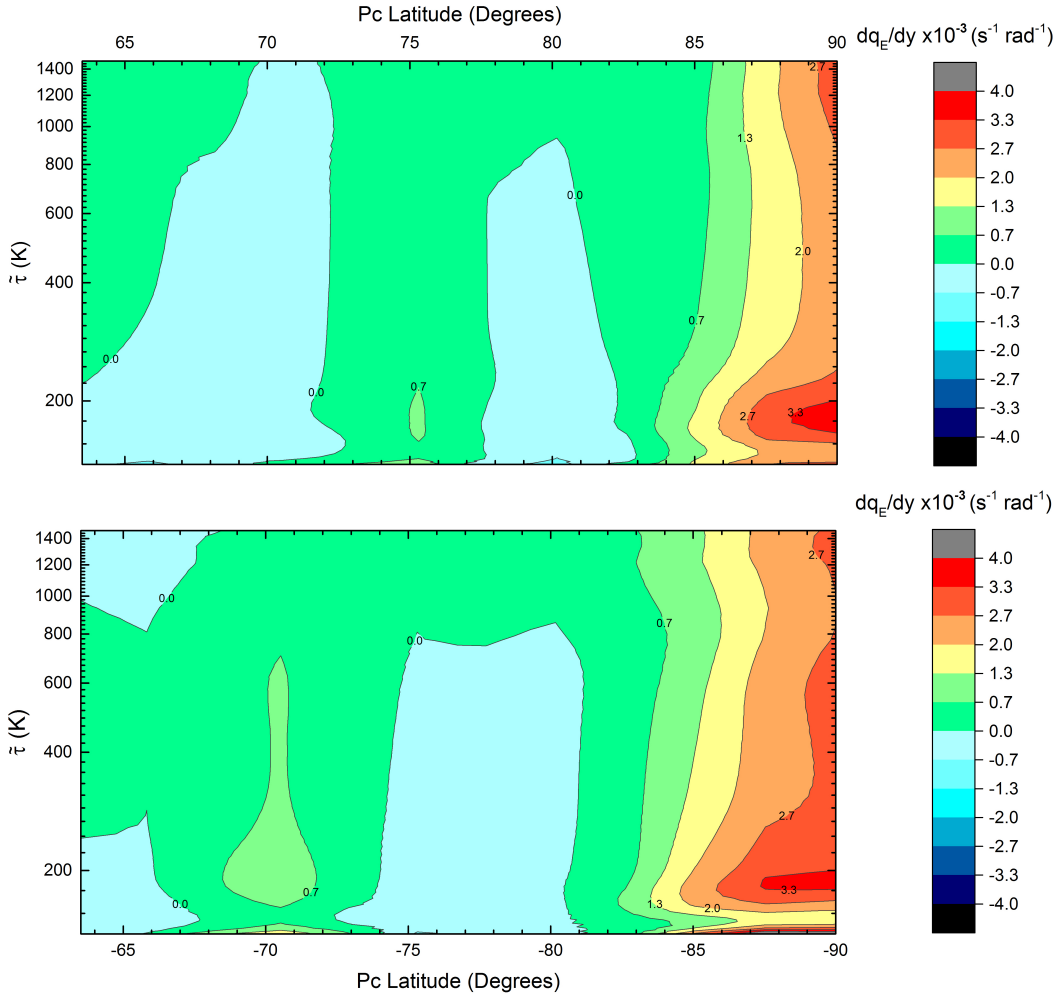

Figure 3.15: Meridional gradient of the normalized Ertel potential vorticity from 63.5° to 90° for the north polar region for June 2013 (top) and south polar region for December 2008 (bottom).

This definition of the quasi-geostrophic potential vorticity is obtained assuming that the specific heat is only a function of pressure. In our case, in order to take into account the variation of the para-hydrogen fraction and therefore, the dependence on the temperature of the specific heat, we use the "entxended" potential temperature computed in the previous section and we follow Gierasch et al. (2004) and Read et al. (2009b) and define a more generalized stability parameter as

$$s^2 = -\frac{Cp}{< Cp >}\frac{T_d}{T_s}\frac{\partial < \ln \tilde{\tau} >}{\partial \ln P} \tag{3.18}$$

where Cp is the normal specific heat and the $<>$ represent, once again, the zonal mean on area-weighting for all latitudes. Figure 3.16 represents the quasi-geostrophic potential vorticity at Saturn's polar regions for December 2008 (south) and June 2013 (north). These maps show that the quasi-geostrophic potential vorticity is,

once again, positive at the north polar region and negative at the south, due to the dominance of the Coriolis parameter, which is an order of magnitude larger than the relative vorticity and the stretching term (third term in equation 3.16), except at the pole. Furthermore, the north polar region reaches higher absolute values of the quasi-geostrophic potential vorticity from $\sim$ 400 mbar to 1 mbar than the south. Finally, comparing the quasi-geostrophic potential vorticity and the normalized Ertel potential vorticity, we see that the former reaches smaller absolute values between 63.5° and $\sim$ 87° north and south than the normalized Ertel potential vorticity, while the contrary happens at higher latitudes.

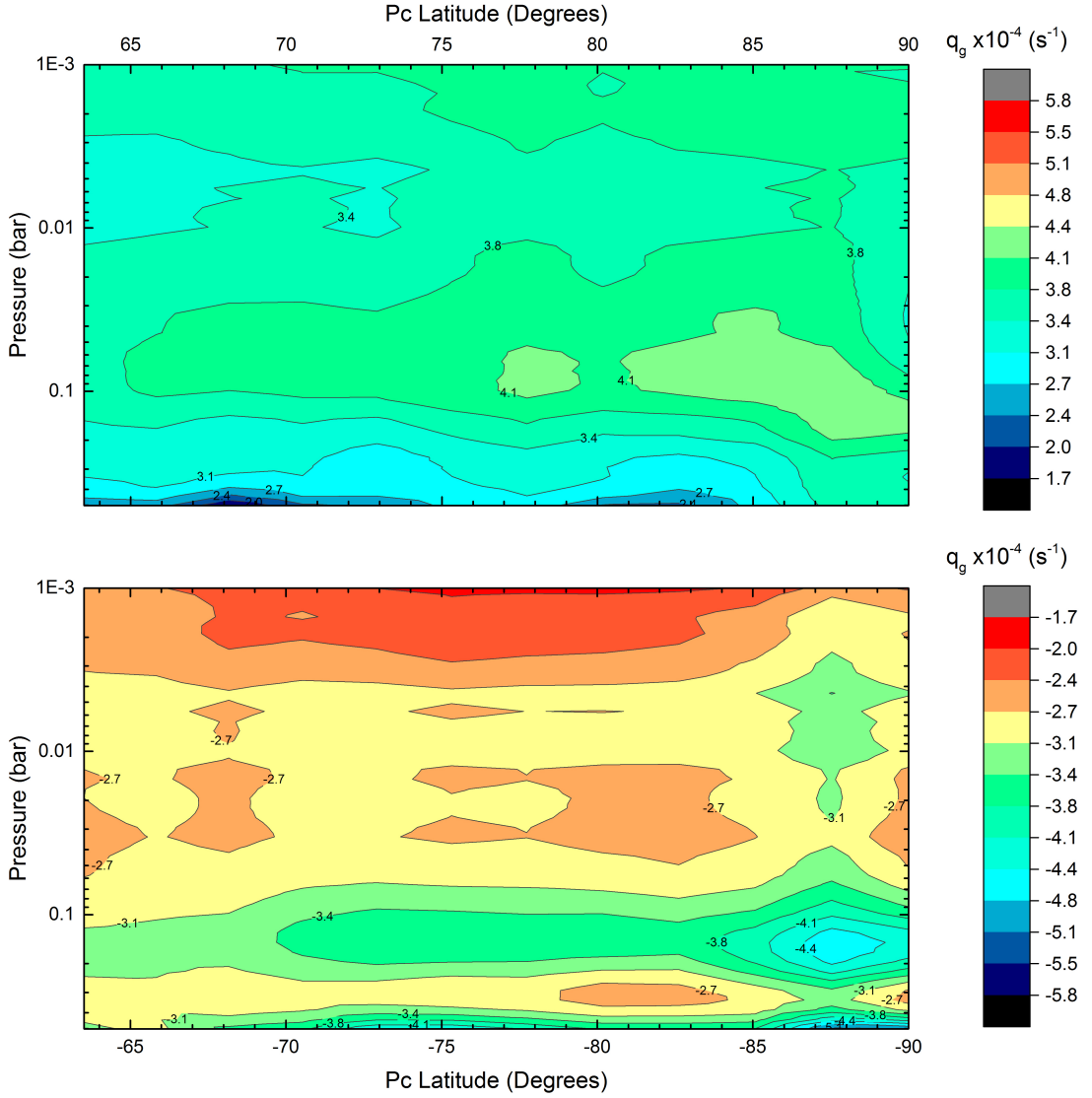

Figure 3.16: Zonally averaged quasi-geostrophic potential vorticity maps from 63.5° to the pole for the north polar region for June 2013 (top) and south polar region for December 2008 (bottom).

Meridional gradients of the quasi-geostrophic potential vorticity for the northern spring and southern summer (June 2013 and October/December 2008, respectively)

are shown in figure 3.17. The results show that, although the normalized Ertel potential vorticity and the quasi-geostrophic potential vorticity maps present some differences, the meridional gradients of these two magnitudes present a similar behavior. For the studied epochs, dq_g/dy changes sign at the flanks of the Hexagon jet and the eastward jet at 70.4°S, as well as at the lower flank of the polar jets, indicating that thermodynamic instability could develop at these regions. We also find that these changes are stronger at the troposphere and at the flanks of the polar jets, showing that overall the jets are more unstable at these regions.

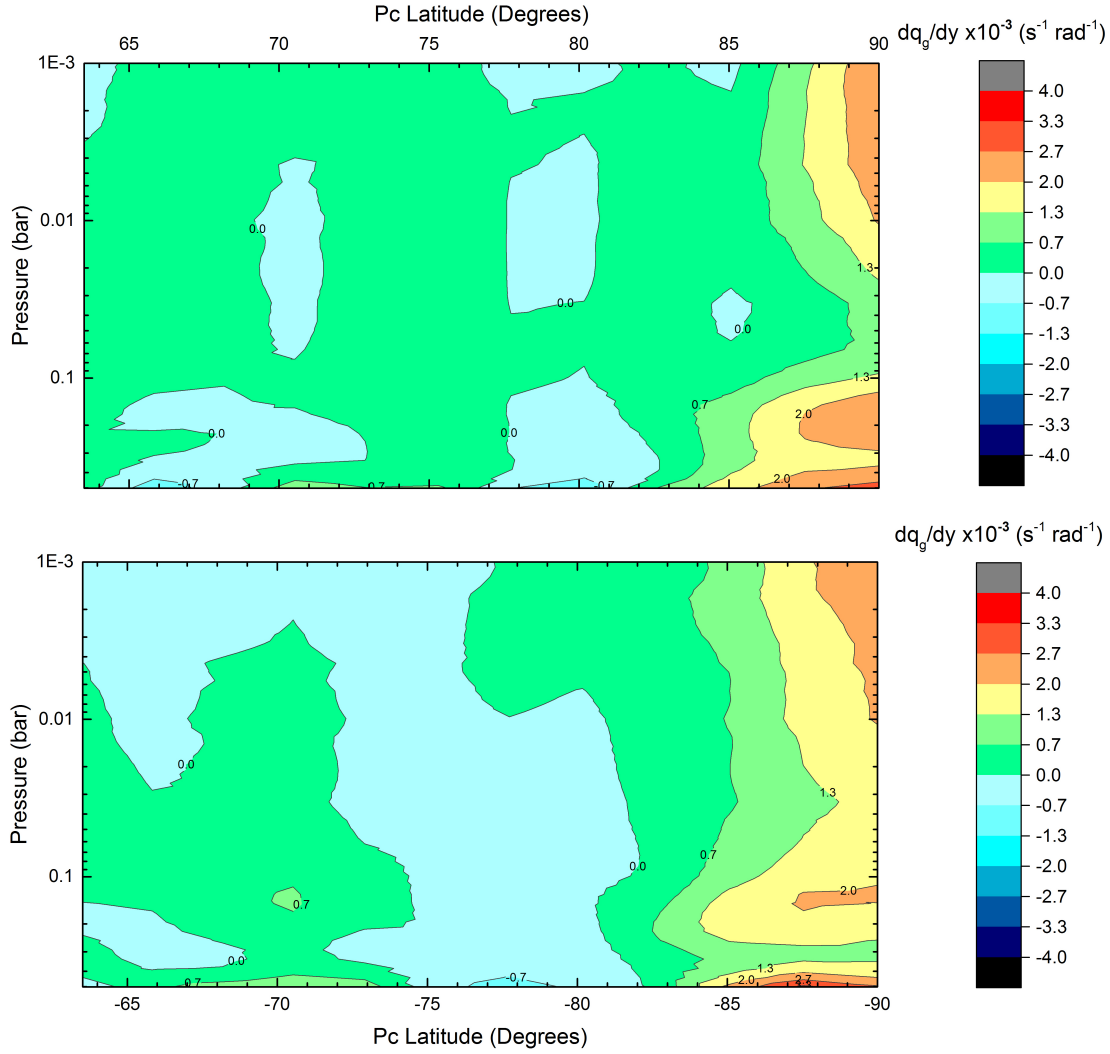

Figure 3.17: Meridional gradient of the zonally averaged quasi-geostrophic potential vorticity maps from 63.5° to the pole for the north polar region for June 2013 (top) and south polar region for December 2008 (bottom).

3.6 Discussion

In this study we have updated the horizontal velocity and vorticity fields of the north and south polar regions, from $\sim 60°$ to $90°$, using Cassini ISS images from June 2013 (north) and October 2006 and July/December 2008 (south).

Bi-dimensional velocity maps of both polar regions are computed. These maps show many similarities on the dynamics of both regions. Firstly, an intense eastward jet with a peak velocity of $140 - 150$ m s^{-1} is found at the outer rim of both polar vortices. Furthermore, a slower eastward jet with peak velocities of ~ 100 m s^{-1} is also observed in both hemispheres, consistent with previous studies (Sánchez-Lavega, 2002a; Baines et al., 2009; Vasavada et al., 2006; García-Melendo et al., 2011). The most remarkable difference between the two polar region is the presence of the Hexagon at the north polar region.

Regarding the shape of the eastward jets, we see that the Hexagon jet and its counterpart in the south are quasi-symmetric jets very similar in width. However, the northern and southern polar jets are clearly asymmetric showing a fast and essentially linear drop in the velocity from the peak at 88.5° to the pole. The width of the polar jets is also different being the northern polar jet 1.4° narrower at its FWHM than the southern polar jet. On the other hand, it is also apparent that the Hexagon jet is located 5° poleward than its counterpart in the south, making the westward jet, located between the Hexagon and the polar jet, narrower than the one in the south.

The north polar region's relative vorticity map shows the Hexagon as a jet stream with a peak vorticity of $\sim 6 \pm 1$ x 10^{-5} s^{-1}, ten times smaller than the Coriolis parameter, dominant at the polar regions. In the south, the relative vorticity map shows that the eastward jet located at 70.4°S reaches similar vorticity values. Furthermore, both polar regions present a very intense cyclonic vortex at each pole attaining high vorticity values of the order of the Coriolis parameter at the poles. In these vorticity maps we can also distinguish the presence of the anticyclonic vortices located at 80.6°N and 66.1°S. Vorticity gradient profiles show that the Rayleigh-Kuo instability criterion for a barotropic flow to become unstable is clearly satisfied at the flanks of the hexagonal jet and its counterpart in the south. The analysis of the barotropic instability as the origin of the Hexagon in the north is studied in Chapter 5.

The potential temperature is computed using the retrieved zonaly averaged temperature profiles by Fletcher et al. (2015) from December 2008 and June 2013 for Saturn's south and north polar regions, respectively. Additionally, as the potential temperature depends on the orto-para fraction of the atmosphere, we assume the normal version of specific heat, which considers a meta-stable distribution with a mole-fraction of molecular hydrogen $X_{orto-H_2} = 0.75$ and we define a new magnitude "extended" potential temperature. Vertical gradients of the "extended" potential temperature indicate that from the upper stratosphere at 1 mbar to the upper

troposphere at 1 bar, Saturn's atmosphere at the polar regions is statically stable ($d\tilde{\tau}/dP < 0$).

In addition, we use the obtained horizontal wind profiles and relate them with the zonally temperature profiles in order to obtain the zonally averaged Ertel and quasi-geostrophic potential vorticity at both polar regions from 63.5° to 90°. The results show that at the Ertel and quasi-geostrophic vorticity the Coriolis parameter is dominant, resulting in positive values at the north and negative values at the south polar region. Meridional gradients of these two magnitudes indicate that a thermodynamic instability could develop, at the studied epochs, at the flanks of the Hexagon, its counterpart in the south and the lower flanks of the polar jets.

Similarities on the horizontal wind profiles, vorticity, temperature and potential vorticity profiles between both polar regions do not give any hint for the presence of the hexagonal wave at the north polar region and its absence in the south.

Chapter 4

Cloud Morphology and Dynamics of Meteorological Features at the North Polar Region

The averaged horizontal wind structure and the zonal mean profiles of the velocity detailed in the previous chapter (3), describe the general circulation of Saturn's polar regions. However, in order to understand the physical processes responsible for the atmospheric dynamics of these regions, it is very valuable to characterize the cloud morphology at different spectral wavelengths, their temporal variation and local motions of the various meteorological features present at these regions.

In this chapter, we describe the cloud morphology of different features present at cloud level in the north polar region and we also analyze their temporal variation and dynamics.

4.1 Hexagon

Some planets of the solar system exhibit transient polygonal features or wavy patterns. On Earth, sub-tropical and polar jet-streams present meandering patterns and some hurricanes show transient polygonal patterns at their interior (Kossin and Schubert, 2001). On Jupiter, different eastward and westward jets in the north and south hemisphere present wavy patterns (Sánchez-Lavega et al., 1998; Barrado-Izagirre et al., 2008) and a similar feature, named the Ribbon, is observed on Saturn eastward jet located at 41°N (Smith et al., 1982; Sromovsky et al., 1983; Sánchez-Lavega et al., 2000; Sánchez-Lavega, 2002a; Sayanagi et al., 2010). However, the hexagonal feature on Saturn located at $\sim$ 75.8°N is a unique feature in the entire solar system.

This singular feature was discovered by Godfrey (Godfrey, 1988) in images from July 1981 captured during the flyby of the Voyager II, when he polar projected and mosaiced them. This mosaic of polar projections showed a clearly hexagonal feature located at 76° north, with sides of $\sim 14,000$ km. Measurements of cloud motions revealed that the hexagon enclosed a fast eastward jet of 100 ms^{-1} and that

the Hexagon itself was stationary. Moreover, at the time of the Voyager flybys, a large anticyclone, named the North Polar Spot (NPS), of $7,000 - 10,000$ km was observed right outside one of the Hexagon's sides (Godfrey, 1988; Sánchez-Lavega et al., 1993). Allison et al. proposed in 1990 that the Hexagon was originated by the interaction of one or more large anticyclones, like the NPS, with the eastward jet (Allison et al., 1990).

After its discovery in the late 80's, the Hexagon and the NPS were re-observed in images captured by the Hubble Space Telescope (HST) and by ground-based telescopes during 1990-1995 (Sánchez-Lavega et al., 1993; Caldwell et al., 1993; Sánchez-Lavega et al., 1997). After Cassini arrived to Saturn, the Hexagon was re-observed first by CIRS in 2007 (Fletcher et al., 2008) and then by VIMS in 2008 (Baines et al., 2009), when the north pole was not illuminated by the Sun and by the ISS cameras after the equinox (Sánchez-Lavega et al., 2014; Antuñano et al., 2015; Sayanagi et al., 2016). However, the NPS was not present in Cassini images indicating that the Hexagon does not need the NPS to keep its shape (Sánchez-Lavega et al., 2014; Antuñano et al., 2015).

When Hubble Space Telescope imaged Saturn's south polar region between 1997 and 2002, a fast eastward jet was discovered at similar latitudes (70.4°S) presenting comparable wind peak velocity (Sánchez-Lavega, 2002a). This eastward jet was zonal and did not present any hexagonal or polygonal pattern and no large anticyclone was observed in these images either (Sánchez-Lavega, 2002a). Vasavada et al. (2006), however, reported a faint polygonal structure at the eastward jet at 70.4° in ISS high-resolution images from 2004. ISS images between April 2008 and January 2009 showed a large anticyclone very similar in size ($7,800 \pm 400$ km) to the NPS just outside the zonal eastward jet (Antuñano et al., 2015). During the presence of this large anticyclone, that we named South Polar Spot (SPS) due to its similarity to the NPS, the eastward jet at 70.4°S did not present significant deviations from a pure zonal jet, indicating that the Hexagon did not originate from the interaction with the NPS.

A singular characteristic of the Hexagon is that its phase speed is almost stationary with respect to System III rotation frame, while it encloses a fast eastward jet. An analysis of images captured by Cassini ISS and with ground-based telescopes between 2008 and 2014, proved that the vertices of the Hexagon are almost stationary respect to Saturn's System III rotation rate, moving westward with an angular drift-rate of $< \omega >= 0.0129 \pm 0.0020°$/day (Sánchez-Lavega et al., 2014).

Observations of the Hexagon in the thermal infrared by CIRS in 2007 showed that in the upper troposphere, between 100 and 800 mbar, there are one warm and one cold belts at 77°N and 73°N, respectively (Fletcher et al., 2008). At the corresponding latitudes, images from VIMS at $3 - 4$ bar from 2008 show cloud covered (dark) and cloud free (bright) regions, respectively (Baines et al., 2009). This correlation between the temperature profiles from CIRS and images in the infrared by VIMS has been explained as a subsidence region at latitudes poleward the hexagonal

jet and an up-welling region at the exterior of the jet (Fletcher et al., 2008).

As described in the previous chapter, similarities in the dynamics of both polar regions do not give any hint of why a hexagonal jet is present in the north and not in the south and a seasonal effect for this explanation can be discarded as the Hexagon survived the long north polar winter. Different interpretations of the origin of the Hexagon will be described and discussed in chapter 5.

In what follows, we describe the cloud morphology of the Hexagon jet and its appearance in different wavelengths and report potential convective structures inside the hexagonal jet. Moreover, we characterize the motions and meandering of the jet and compare them with the dynamics of local features inside it.

4.1.1 Cloud Morphology

Both the Hexagon and its enclosed eastward jet, are clearly visible in wavelengths from the near-infrared ($\sim$ 1000 nm) to the violet (420 nm), which sense the upper troposphere at levels 100−700 mbar (Pérez-Hoyos et al., 2005; Sánchez-Lavega et al., 2006; García-Melendo et al., 2009; Sanz-Requena et al., 2017), in thermal infrared at wavelengths between 14.7 μm and 16.6 μm, which sense the upper troposphere at around 150 mbar (Fletcher et al., 2008), and also in images obtained by VIMS at 5 μm that sense the deep troposphere at around $4-5$ bar (Baines et al., 2009). However, in the thermal infrared at wavelengths between $7.4-8$ μm, which sense the upper stratosphere at ~ 1 mbar, the Hexagon is not longer observable (Fletcher et al., 2008, 2015). Figure 4.1 shows the Hexagon and its jet at visible wavelengths.

The regions north and south of the Hexagon jet have quite different appearance in visible and in 5 μm wavelenghts. CB2 and CB3 filters sense the top of the ammonia clouds, which is found at around 600 mbar at the latitude of the Hexagon (Sanz-Requena et al., 2017). In these filters, the Hexagon's interior, at the north of the jet, looks darker than the exterior, at the south, showing a dark and cloud-free area of $0.5-0.7°$ width right to the north of the jet. Both the interior and the exterior of the Hexagon present a large amount of compact clouds and small vortices that will be described in section 4.2. Methane band MT2 and MT3 filters, do not go through the tropospheric haze present at the polar region and they sense clouds high in the upper troposphere, which appear as bright features in these images. In these filters, the appearance of the Hexagon is plainer, with few details. The interior of the Hexagon is again darker than the exterior, indicating that the hazes penetrate deeper in the troposphere in the interior region of the Hexagon, as proposed by Sanz-Requena et al. (2017). Finally, the entire polar region looks bright in blue (BL1) and violet (VIO) filters, due to the Rayleigh scattering by the gas, and in these wavelengths the Hexagon's interior looks brighter than the exterior because of the presence higher or more dense hazes.

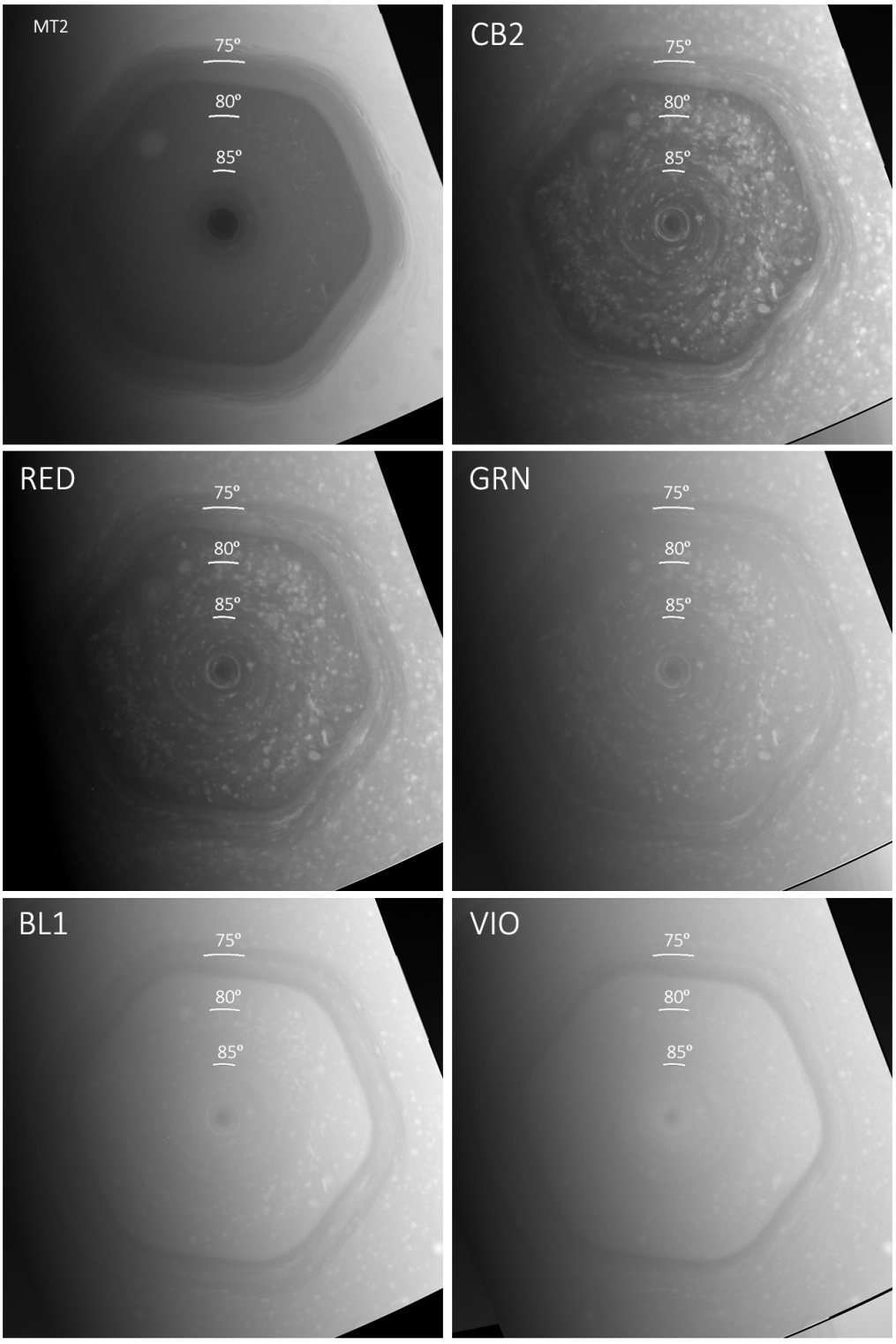

Figure 4.1: Cloud morphology of the Hexagon at different wavelengths captured by Cassini ISS wide angle camera on 25 June 2013.

The hexagonal eastward jet, when observed in CB2 and CB3 images, it is marked by elongated bright and dark clouds of $0.3 - 0.5°$ meridional width. The elongation of the clouds is due to the horizontal wind-shear on the jet, and clouds at the edges of the eastward jet are less elongated than the clouds near the center. These bright filaments are not parallel to each other, presenting a deviation towards the center of the jet, where the velocity is higher. The latitudinal and longitudinal distributions of these clouds are not homogeneous, and there are regions where larger or brighter clouds are observed. Measurements between 2008 and 2014 showed that in those filters the mean width of the jet is $2.8° \pm 0.5°$ and that the vertices of the Hexagon are located at a mean latitude of $74.7°\text{N} \pm 0.2°$ (Sánchez-Lavega et al., 2014). When the jet is observed in MT2 and MT3 filters, it is seen brighter than the Hexagon's interior but darker than the exterior and it presents some dark filaments that do not strictly follow its meandering pattern. The edges of the hexagonal jet observed in these wavelengths do not correspond exactly to the edges observed in CB2 and CB3 and are more distinct at the northern part of the jet. Finally, when it is observed in blue or violet filters, the eastward jet appears narrower with a dark region of $\sim 0.9°$ latitude following its meandering motion, not present when observed in other filters.

4.1.2 Zonal Winds

In the previous chapter, we described the general averaged zonal wind velocity profiles of the north and south polar regions. In these profiles, we averaged the vectors in latitudinal bins without taking into account that the hexagonal jet is not zonal and this introduced a large standard deviation in our profile. In order to solve this problem and to characterize the actual shape of the jet, we create a new coordinate system that measures latitudinal distances to the peak of the jet at a given longitude, following the meandering motion of the jet. To calculate the position of the maximum of the jet as a function of the longitude, we binned the zonal and meridional vectors between 60° and 83° north into 0.25° latitudinal bins using moving bins of 0.5° and 4° longitudinal bins with moving bins of 8° and then, we perform a sixth-grade polynomial fitting of the modulus of the velocity against the latitude for each longitudinal bin. After plotting the latitudes of the velocity peak against longitudes (figure 4.2a), we see that they can be fitted to a sinusoidal wave of wavenumber six defined as

$$\phi_{max}(\lambda) = \phi_0 + \Delta\phi_0 \sin\left(\frac{2\pi}{\Lambda}(\lambda - \lambda_0)\right) \tag{4.1}$$

where $\phi_0 = 75.79° \pm 0.01°$ is the mean latitude of the hexagonal jet, $\Delta\phi_0 = 0.49° \pm 0.01°$ is the amplitude of the oscillation, $\Lambda = 59.7° \pm 0.2°$ is the wavelength and $\lambda_0 = -6.0° \pm 0.7°$ is the phase shift.

When we plot this sinusoidal wave on top of a polar projection of the north polar region (figure 4.2b), we observe that the vertices of the Hexagon are the minimums of the sinusoidal wave, while the center of the sides correspond to the maximums. This indicates that the hexagonal feature is a sinusoidal wave of wavenumber six

that oscillates in latitude between 75.3° and 76.3°, which is seen as a Hexagon when it is polar projected. Figure 4.2c and figure 4.2d, show that if the amplitude of the sinusoidal would be twice of the observed amplitude, the eastward jet would be seen as a wavy pattern when polar projected, while an amplitude of half of the observed amplitude value would give a more zonal eastward jet.

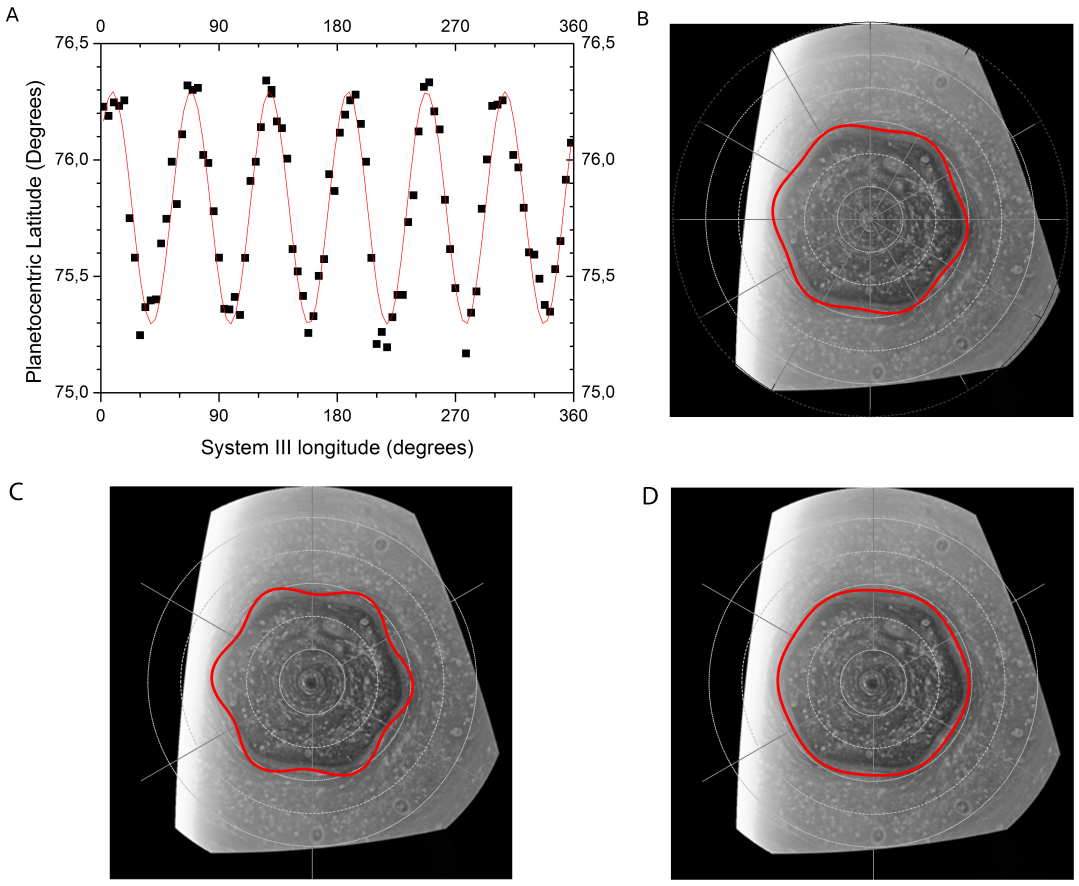

Figure 4.2: Panel A represent the latitudinal locations of the modulus velocity peaks for different longitudes (black squares) and the performed sinusoidal fitting (red solid line). Panel B shows the sinusoidal fitting polar projected on top of a WAC image from 25 December 2013. Panel C and D show a polar projection of a sinusoidal wave with a $\triangle\ \phi_0 = 1°$ (C) and $\triangle\ \phi_0 = 0.25°$ (D).

Once the latitudes of the velocity peaks for different longitudes are known, the new latitudinal coordinate, which measures the distance to the peak can be easily implemented. Equation 4.1, allows us to define a zonal coordinate $\phi'_k = \phi_k - \phi_{max}(\lambda_k)$, where ϕ_k and λ_k are the latitude and longitude of a given point. The new coordinate measures the distance in degrees to the maximum of the jet, with positive values north of the jet. Moreover, associated to this new coordinate there is a local reference system with axes x'_h parallel to the jet mean motion, and y'_h

perpendicular to it, that forms an angle

$$\tan\theta(\lambda) = \frac{1}{\cos\phi_0}\frac{d\phi_{max}}{d\lambda} \tag{4.2}$$

with the standard (x,y) coordinates tangent to the latitudinal circle and perpendicular to it. We can therefore decompose individual velocities in a component tangent and perpendicular to the jet as

$$u_h = u\cos\theta - v\sin\theta \tag{4.3}$$

$$v_h = v\cos\theta + u\sin\theta. \tag{4.4}$$

If we calculate averages of u_h in bins of constant ϕ' we obtain a mean profile adapted to the jet motion. Figure 4.3, shows the wind profile adapted to the jet compared with a standard zonal average. As it can be expected from the small deviations from zonal motions implied by equation 4.1, our analysis shows little difference between the two profiles, but when we take into account the meandering of the jet, the average profile is narrower and 5 ms^{-1} faster, reaching 105 ms^{-1}, and the standard deviation is consistently smaller. The vorticity and vorticity gradient profiles obtained from this zonal profile are shown in figure 4.4 by a dash-dotted red line. When we perform a zonal average of the meridional component, it is zero in both analysis, but in a purely zonal average, the standard deviation doubles its value in the latitudes of the Hexagon, reflecting the meandering of the jet, while it is essentially flat if averages are performed along the jet as described above.

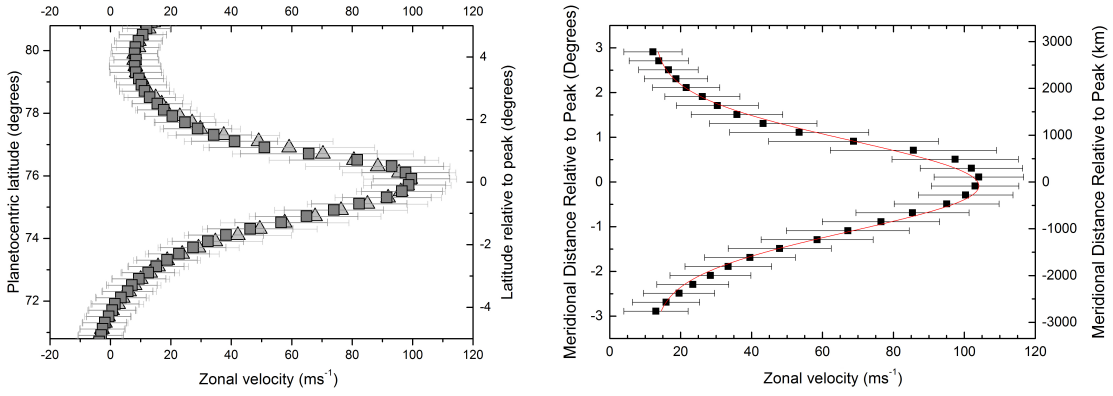

Figure 4.3: Left figure shows the hexagonal jet wind profile using two different methods. Light triangles and light error bars represent the zonal averages and standard deviation of the zonal winds. Darker squares and error bars represent averages for a reference system centered on the Hexagon jet peak. Right figure shows the Gaussian fit (red line) of the measured zonal winds of the hexagonal jet (black dots).

Following Allison et al. (Allison et al., 1990), we fit the zonal wind profile of the Hexagon to a Gaussian function defined as

$$u = u_0 \exp(-\frac{bR^2\,(y-y_0)^2}{2u_0}) \tag{4.5}$$

where R is the planetary radius at the Hexagon's mean latitude, $u_0 = 104$ ms^{-1} is the velocity peak, $b = 8.0\text{x}10^{-11}$ m^{-1}s^{-1} is the curvature of the jet and y is the meridional distance relative to the peak in kilometers. The full width at half maximum (FWHM) is $2.38° \pm 0.05°$, which is equivalent to $2,275 \pm 50$ km. This Gaussian, as shown in figure 4.3, fits very well the zonal wind profile of the Hexagon obtained taking into account its meandering.

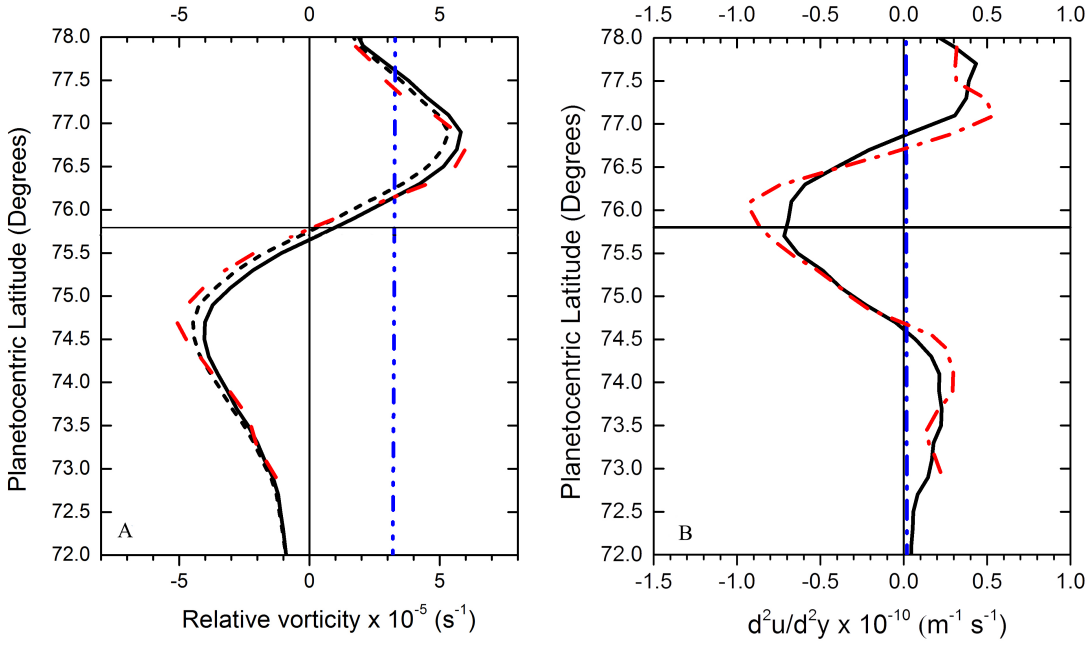

Figure 4.4: Left figure shows the relative vorticity (black dashed line), $-\partial u/\partial y$ (dark solid line) and $-\partial u_h/\partial y$ obtained using the zonal winds adapted to the Hexagon's meandering (red dash-dot line), while the figure on the right represents $\partial^2 u/\partial^2 y$ (black solid line) and the adapted gradient of the ambient vorticity $\partial^2 u_h/\partial^2 y$(red dash-dot line). The dash-dot-dot blue lines represent the Coriolis parameter (left) and the β parameter (right). The horizontal black solid line indicates the latitude of the center of the hexagonal jet.

4.1.3 Local Transient Activity

The study over 36 years of the Hexagon and its eastward jet has shown that they are long-lived stable features (i.e. Sayanagi et al. (2016)). However, Cassini ISS high-resolution images show that although they have remained unchanged since Voyager flybys, local transient activity can develop inside the hexagonal jet.

The most notable activity in this jet during the period of our study (January 2009 to November 2014) is a plume-like feature observed in CB2 images from 22-24 July 2013 as a large and bright feature, shown in figure 4.5a. At its maximum

longitudinal size, this plume is larger than half of the Hexagon's side and around 2/3 of its width, reaching longitudinal and meridional dimensions of $8,746 \pm 116$ km ($37.7° \pm 0.5°$) and $2,000$ km ($2.1°$), respectively. On 22 July, this feature was located at a vertex of the Hexagon and it grew $\sim 5°$ until it reached its maximum length at the first hours of 24 July 2013.

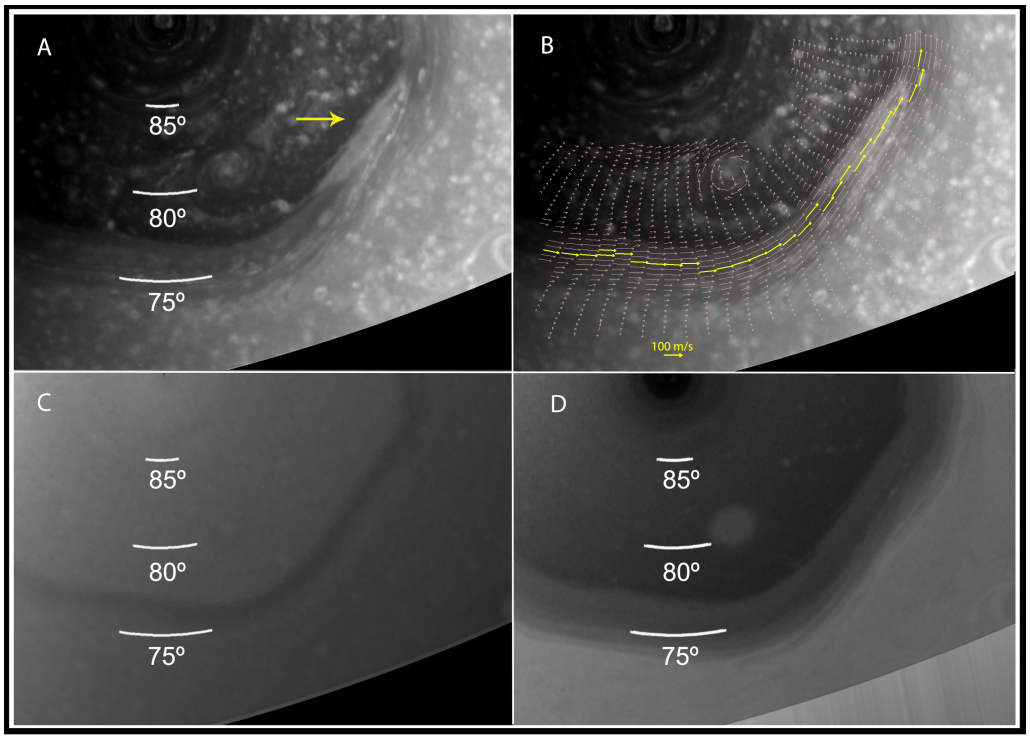

Figure 4.5: Four polar projections from 70°N to the pole of a meridional resolution of 0.02°/pixel from 23 July 2013 in CB2 (A and B), VIO (C) and MT2 (D). Panel a shows the transient plume-like feature marked by the yellow arrow and (B) shows the horizontal wind vectors of this region. The yellow arrows indicate the location of the peak velocity of the jet. The data in panel (B) is binned in 0.3° latitude and 4° longitude. (Figure from Antuñano et al. (2017))

An examination of the morphology of this feature shows that its head is not located at the latitude of the velocity peak of the jet, but 0.9° north of it, close to the northern edge of the jet, as represented in figure 4.5b, where the pink arrows represent the horizontal wind field and the yellow arrows indicate the location of the peak velocity of the hexagonal jet. Furthermore, we also observe that the end of the plume is divided longitudinally in two by a dark elongated region and that a smaller dark region is also located near its head. The absence of the plume-like feature in images captured with methane absorption band (MT2 ad MT3) filters (figure 4.5d) and with violet filter (VIO) (figure 4.5c), indicate that this feature is located at the same level as the surrounding clouds.

In order to determine the motion of this feature and its relationship with the dynamics of the hexagonal jet, we have measured two image pairs from 23 July 2013 separated by 89 and 125.55 minutes, respectively. Wind measurements performed by the brightness correlation software (see chapter 2.5 for measurement method in-

formation and measurement resolutions) show that overall, the plume follows the motion of the hexagonal jet during the observed period, showing a drift rate of $\omega = -33.76 \pm 0.59°$/day at its head, which corresponds to a zonal velocity of 89 ± 2 ms^{-1}. However, cloud tracking of smaller details inside the plume, indicate that some of these small details present zonal velocities that differ from the background, as represented in figure 4.6, where the represented uncertainties are computed taking into account the pointing error and the image resolution. This implies that some of the local movements inside the Hexagon cannot be interpreted as the motion of passive tracers. The meridional velocity of these details is ~ -20 ms^{-1}, following the meandering of the jet.

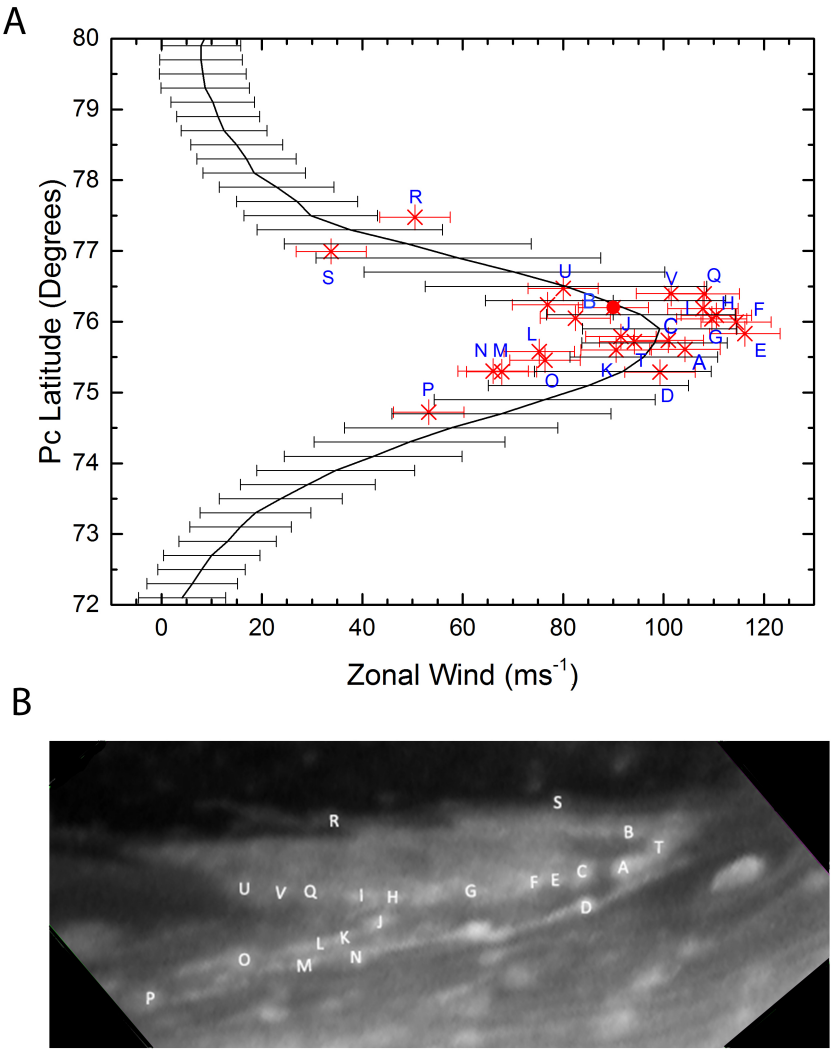

Figure 4.6: Figure A shows the zonal wind measurements of small details inside the plume (red crosses) compared to the zonal wind profile of the Hexagon (black solid lines). Figure B shows the plume-like feature in a screen-shot of a polar projection of meridional resolution of 0.02°/pixel centered at 76.5°N latitude and 120.8° longitude. In both figures, the tracked features are indicated by letters. (Figure from Antuñano et al. (2017))

The determination of the lifetime of the plume and the characteristic time-scale of its evolution is limited by the lack of images of this region around the observation dates. Previous images that captured the north polar region are from June 26 2013, a month before the plume was observed. These images do not show any plume-like feature, indicating that the plume observed in July 2013 evolved rapidly in less than a month. This, together with its brightness and the elongated shape of the plume, reveals that this plume could be of convective nature.

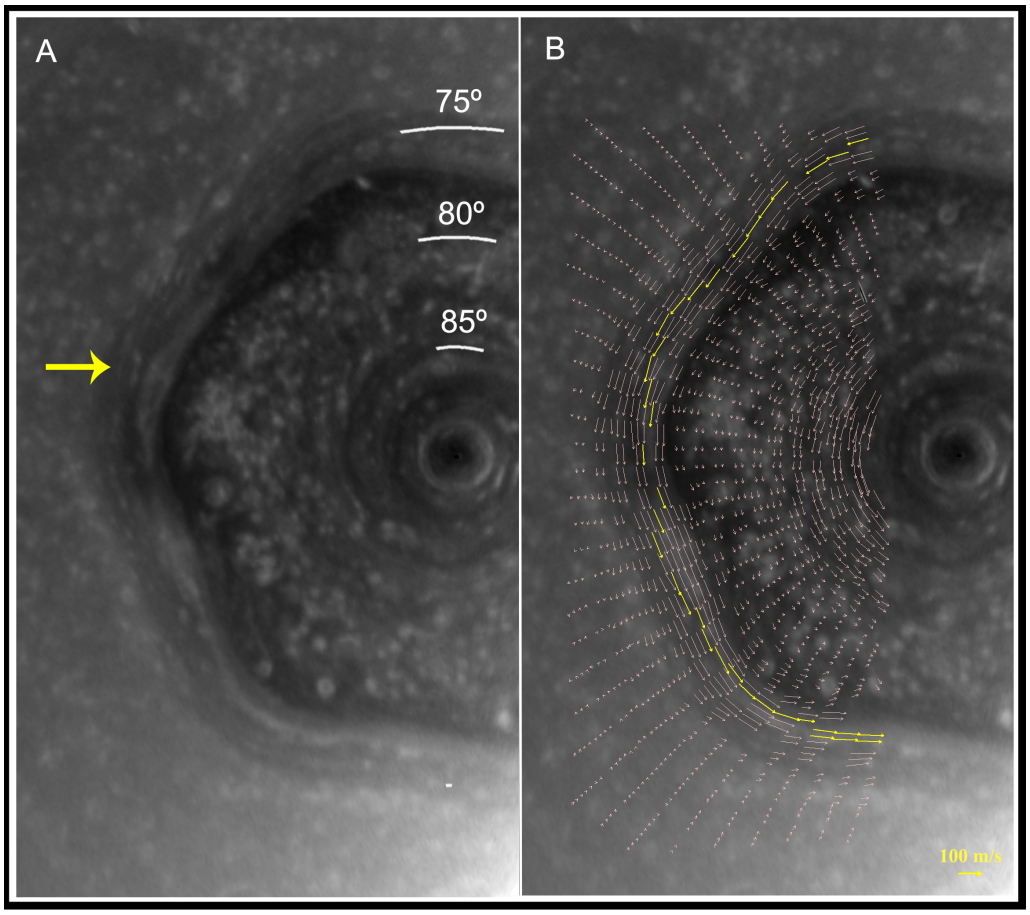

Figure 4.7: Polar projection of the north polar region from 70°N to the pole from 27 November 2013 showing the plume-like activity indicated by a yellow arrow (A) and the wind vectors at this region (B). The yellow arrows in panel (B) indicates the location of the peak velocity of the Hexagon jet. The data is binned in 0.3° latitude and 4° longitude. (Figure from Antuñano et al. (2017))

Regarding its life-time, next images showing this region are from 27 November 2013. These images show another plume-like feature at one of the vertex of the Hexagon, with longitudinal and meridional dimensions of $8,400 \pm 221$ km ($38° \pm 1°$) and $\sim 1,240$ km ($\sim 1.3°$), that is, this plume-like feature is similar in longitude, but narrower than the one from July 2013. This second feature is shown in figure 4.7a. Wind measurements of two image pairs from 27 November 2013, separated by 86 minutes and performed by the brightness correlation software, indicate that this feature moves at the same velocity as its background, presenting a velocity at its head of 85 ± 2 ms^{-1} (or a drift rate of $\omega = -32.17 \pm 0.63°$/day) (see 4.7b). Mea-

surements of small details inside the plume were not carried out due to the lower resolution of the images. The very similar characteristics of these two plumes raise the question of whether they are the same feature, which has survived 4 months, or if they are two different features, giving in this case information about the frequency of the phenomenon.

To try to determine this point, we have tracked the longitudinal position of this plume and we see that it deviates around 100° from the expected longitude of the plume from July 2013. Unfortunately, this discrepancy is not sufficient to guaranty that the two plumes are different features, since a decrease of just 5ms^{-1} on the velocity of the first plume, could explain this deviation.

4.1.4 Comparison with the equivalent region at the South

In the south polar region of Saturn, a fast eastward jet is observed at 70.4°S in wavelengths from the violet (420 nm) to the near-infrared ($\sim$ 1000 nm). This jet is circular, without any significant deviation from zonal motion. At some specific epochs, there are faint quasi-linear regions at some longitudes, different at separate dates (Vasavada et al., 2006). However, the eastward jet does not show a clear entire wavenumber in any of the cases. Figure 4.8 shows the morphology of the south polar region, where the circular jet is clearly visible.

Although its shape is different from the hexagonal jet, its appearance at various wavelengths is similar to its northern counterpart. CB2 and CB3 images show the interior of the eastward jet darker than the exterior presenting a large number of small clouds inside and outside it. Furthermore, the jet is distinguished by bright clouds that are elongated due to the horizontal wind shear. However, these images do not show as many small details as CB2 and CB3 images of the north polar region, probably due to the tropospheric haze present at the south polar vortex during its summer. MT2 and MT3 images show the circular jet brighter than the region of higher latitudes, indicating that it is higher in the troposphere than the latitudes poleward to it. So far, no plume-like convective activity has been observed in the jet at 70.4°S at any wavelength.

In order to compare this jet with the hexagonal one, we compute a fitting of the zonal velocity using the Gaussian function defined in equation 4.5. In this case we find that it is wider than the hexagonal jet, presenting a FWHM of $2.8° \pm 0.1°$ ($2,700 \pm 90$ km) and slower, with a mean velocity peak is $u_0 = 88 \pm 20$ ms^{-1} located at $\phi = -70.41° \pm 0.01°$ latitude with a curvature of $b = 8.0\text{x}10^{-11}$ $\text{m}^{-1}\text{s}^{-1}$. This Gaussian fit is represented in figure 4.9.

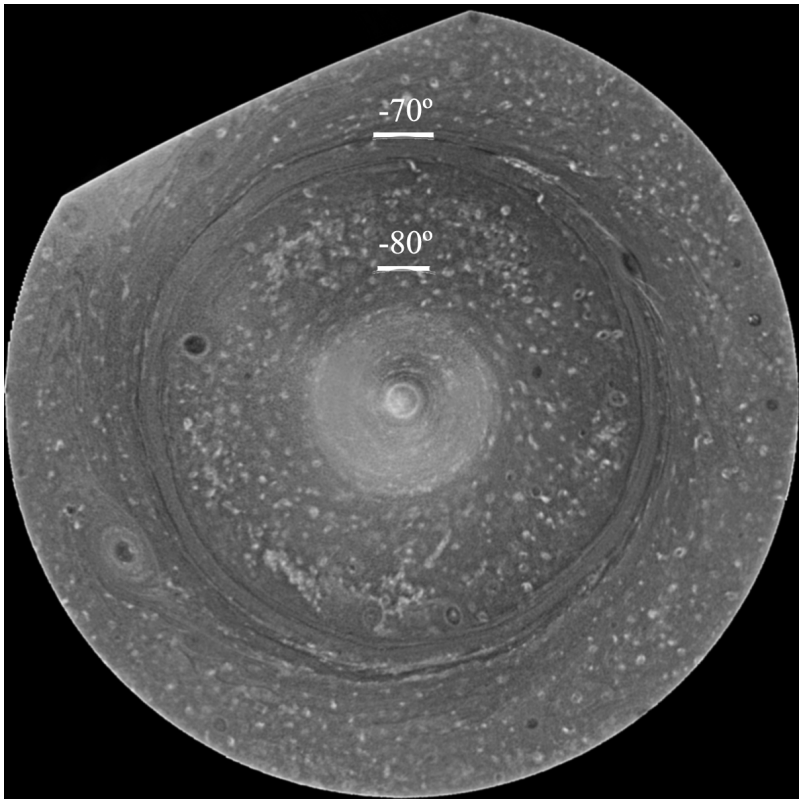

Figure 4.8: A polar projection from −60° to −90° from 3 December 2008 with a meridional resolution of this polar projection is 0.05°/pixel. This is built using four different CB2 images. The eastward jet is indicated by a yellow arrow. The brighter region around the pole is an artifact due to each image used to build this polar projection had different illumination angles.

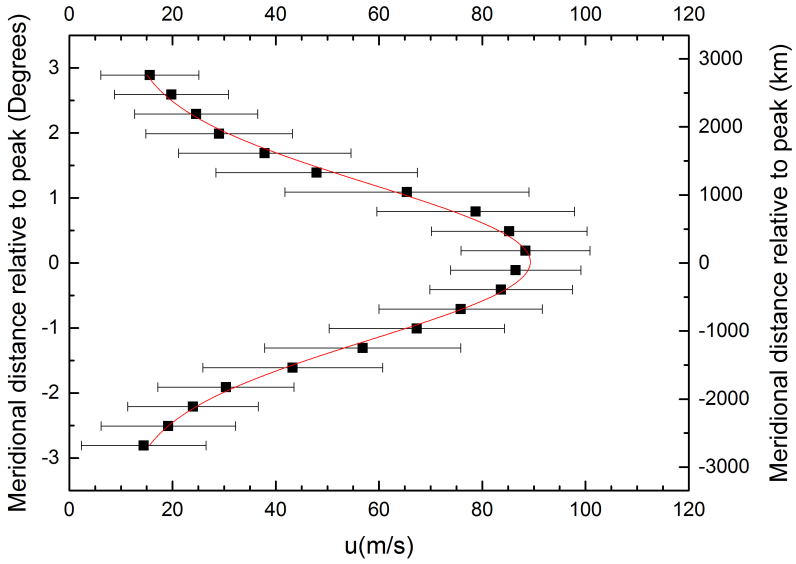

Figure 4.9: The Gaussian fitting (red line) compared to the averaged zonal velocity field of the eastward jet at −70.4° (black squares). (Figure from Antuñano et al. (2015))

4.2 Puffy Cloud Field and Regular Vortices

All the outer planets of our Solar System (Gas Giants and Icy Giants) present vortices in their atmospheres. Jupiter is the planet with the largest number of vortices. Its most characteristic one is an anticyclone called the "Great Red Spot" (GRS) (Rogers, 1995; Ingersoll et al., 2004) located at 22.5°S that has been observed over ~ 300 years and that nowadays measures around $16,000$ km in longitude and $11,000$ km in latitude. Another important anticyclone is the so-called "BA", which is located at 33.5°S and has half the size of the GRS (Sánchez-Lavega et al., 2001). Saturn is the second planet with the largest number of vortices and they are smaller than the ones found in Jupiter (Vasavada et al., 2006; Baines et al., 2009; del Genio and Barbara, 2016) with sizes around $2,000 - 4,000$ km. In the case of the Icy Giants, Neptune presents anticyclones at middle and low latitudes of sizes of $5,000 - 15,000$ km accompanied by higher clouds, and only one vortex , seen dark, has been detected in Uranus.

The cloud morphology of Saturn's polar regions is characterized by the presence of a large amount of small bright clouds and vortices of different sizes, shapes and life-times. In our study, we distinguish vortices from compact clouds by defining as vortices circular or elliptical clouds larger than $1,000$ km in longitude or latitude. In this section we describe the temporal variability and dynamics of vortices of this kind located at the north polar region between January 2009 and November 2014 and also, the seasonal variability and morphology of the compact clouds at the north polar region between January 2009 and June 2013.

4.2.1 Regular Vortices

The largest vortex found on Saturn's polar regions (apart from the polar vortex), is the so-called North Polar Spot (NPS). As mentioned above, this long-lived anticyclonic vortex, discovered in Voyager images from 1981 (Godfrey, 1988), was located at 75°N, just outside one of the sides of the Hexagon, and it remained at least until 1995 (Sánchez-Lavega et al., 1993, 1997). It had an elliptical shape of $\sim 10,000$ km in its west-east direction and $\sim 5,000$ km in the north-south direction (Godfrey, 1988; Sánchez-Lavega et al., 1993, 1997) and it was seen reddish in color and bright in methane band filters (Hunt and Moore, 1982; Sánchez-Lavega et al., 1997). Another remarkable anticyclone was observed in Cassini images between April 2008 and January 2009, this time in the southern polar region located at 66°S, and it was named the South Polar Spot (SPS) in analogy with the vortex in the north(Antuñano et al., 2015). Again, the vortex was elliptical with zonal dimension (west-east) of $7,800 \pm 400$ km and meridional dimension (north-south) of $4,800 \pm 400$ km, and it was seen bright with a dark region at its center in CB2 and CB3 images and bright in MT2 images.

During the epoch under study (January 2009 to November 2014) different smaller vortices appear in the north polar region, indicated by arrows in figure 4.12. The most notable one is a bright oval located at a mean latitude of $80.6° \pm 0.2°$ with

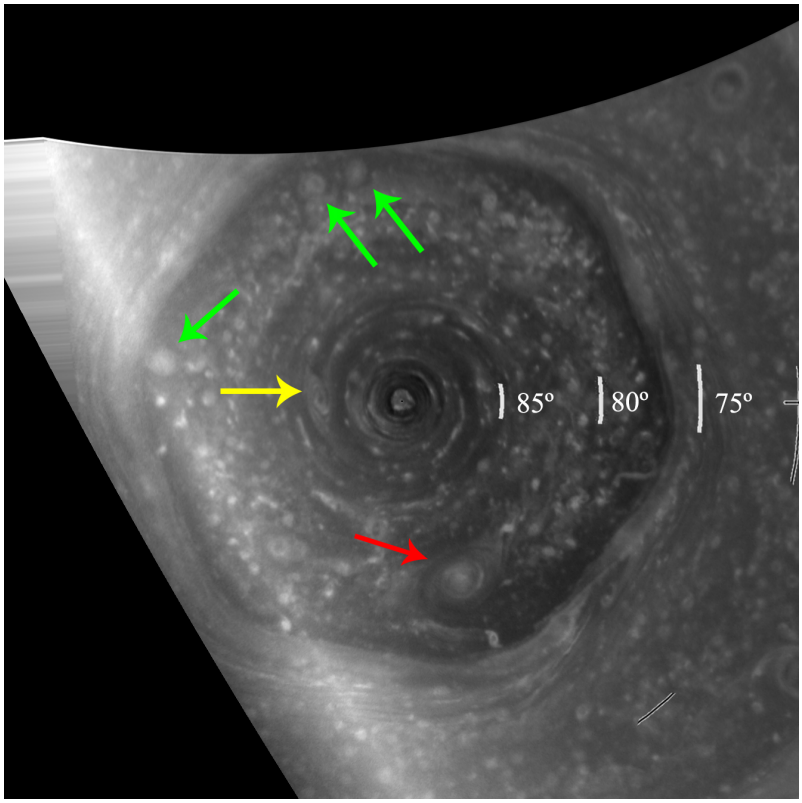

Figure 4.10: A polar projection from 70°N to the pole from 24 July 2013 showing different anticyclones and cyclones indicated by arrows.

a zonal dimension of $23 \pm 1°$ ($3,616 \pm 157$ km) and $2.5 \pm 0.5°$ ($2,380 \pm 480$ km) meridional dimension, visible in Cassini ISS images since at least November 2012 to January 2015, showing that it is a long-lived feature. A similar vortex located at similar latitudes was visible in VIMS images during the north polar winter (Baines et al., 2009) and in ISS images in January 2009, but the large period between these two early observations and the epoch under study does not allow us to identify them as the same feature.

Examinations of the appearance of the vortex at 80.6° between November 2012 and January 2015, show that in CB2 and CB3 images, this vortex consists of an inner bright region of $18 \pm 1°$ ($2,850 \pm 157$ km) zonal dimension and $2.2 \pm 0.2°$ ($2,300 \pm 240$ km) meridional dimension, formed of small spiraling clouds, surrounded by an outer region of lower contrasted clouds of $5 \pm 1°$ (786 ± 157 km) zonal dimension and $0.2 \pm 0.2°$ (240 ± 240 km) meridional dimension. This vortex, is also visible in methane absorption band filters as a bright structure, while it is not observed in VIO images, suggestive of a feature relatively high in the troposphere. Its mean drift rate deduced from a linear regression of the measured longitudes between November 2012 and September 2014 is $\omega = -6.063 \pm 0.021°$/day relative to System III, which corresponds to a mean zonal velocity of $\bar{u} = 11$ ms^1, this is, it moves in general with the background. Figure 4.11b, illustrates the residuals in longitude position of the vortex relative to its reference system, where a variation of $\pm 1 \text{ms}^{-1}$ on the zonal velocity of the vortex could explain the deviation shown in this figure. Its relative vorticity measured in ISS images captured in June 2014 is $-7 \pm 1 \times 10^{-5}$ s^{-1}, around

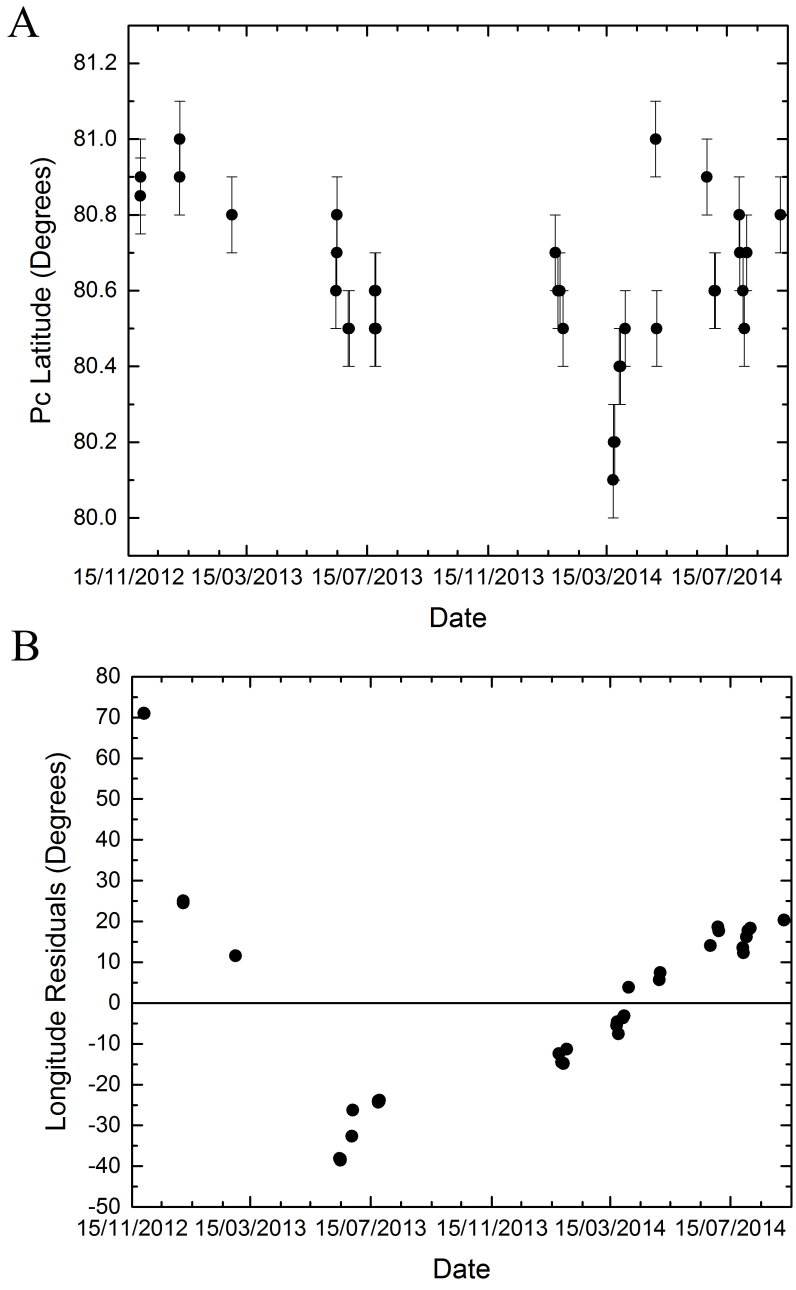

Figure 4.11: (Variation of the latitudinal position of the vortex located at 80.6° (A) and the residuals in longitude relative to the reference system of this vortex (B) between November 2012 and September 2014.

ten times the relative vorticity (du/dy) of the background and 1/4th of the Coriolis parameter $f = 2\Omega \sin(\phi)$ at that latitude, where Ω is the planetary angular vorticity and ϕ is the latitude. Tracking of the latitude of this vortex during the studied epochs, shows that the vortex oscillates in latitude, as it is represented in figure 4.11a.

The second largest vortex present at the north polar region during the epoch under study, is an elliptical anticyclone located at a mean latitude of $85.8° \pm 0.1°$ with

a zonal dimension of $27 \pm 3°$ ($1,879 \pm 208$ km) and meridional dimension of $1.5 \pm 0.1°$ ($1,425 \pm 95$ km). It is present in CB2 images over one year, between November 2012 and November 2013, while it is not visible in methane absorption band and violet images, indicating that it is trapped at cloud level. During this period its morphological appearance varies considerably, changing from an elliptical shape with a dark region at its center surrounded by bright narrow filaments in November 2012 to a less contrasted elliptical vortex with a dark region at its center surrounded by a brighter area and a dark region at its edge in July 2013. After this epoch, ISS images do not show this anticyclone. Tracking of the position of this vortex during the studied epoch indicates that its zonal mean velocity is $\bar{u} = 96 \pm 5$ ms^{-1} (mean drift rate of $\omega = -124.0 \pm 5.6°$/day) and therefore, it moves with the background. The resolution of images and the time interval between different images of the vortex did not allow the calculation of the relative vorticity of this vortex. On the other hand, the latitude of this last vortex oscillates between 85.6° and 85.9° during the studied period.

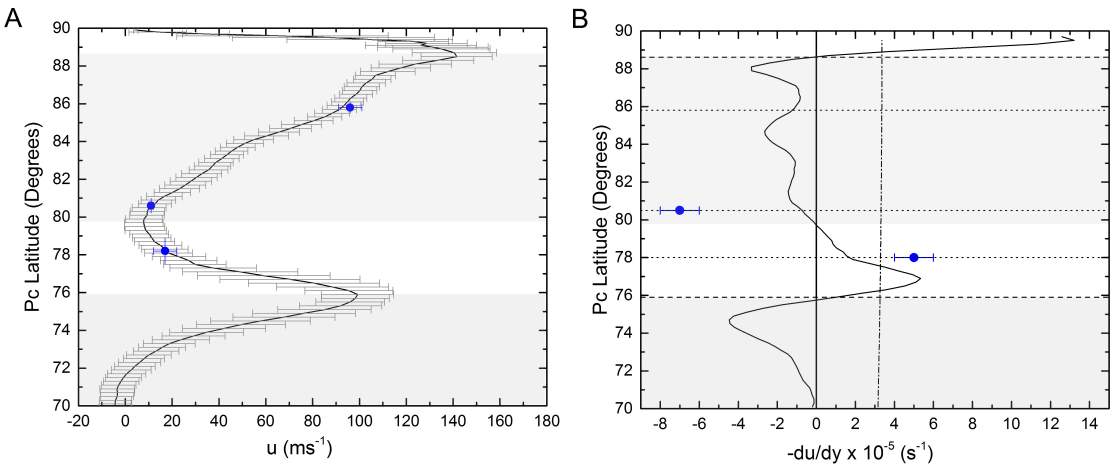

Figure 4.12: (A) Zonal mean velocity of the anticyclones at 80.6°N and 85.8°N and the cyclones at 78.2°N (blue dots) compared with the zonal mean velocity of the background (solid black line). (B) The relative vorticity of the anticyclone at 80.6°N and cyclones at 78.2°N (blue dots) compared to $-du/dy$ from 70°N to the pole (solid black line) and the Coriolis parameter (dashed-dot black line). The shadowed areas represent the anticyclonic regions, while white areas are cyclonic regions. In both panels horizontal dotted lines represent the location of the different cyclones and anticyclones and the dashed lines represent the location of the Hexagon and the north polar vortex.

Finally, different small circular cyclonic vortices have been observed in CB2 and CB3 images at around 78.2°N during the different epochs under study, with a size of the order of $5° - 7°$ ($1,000 - 1,500$ km). These vortices are not observed in methane band and violet filters. Between January 2009 and November 2014, the number of visible vortices varied, ranging from three to five vortices present simultaneously, presenting a vorticity of the order of $4 \pm 1 \times 10^{-5}$ s^{-1}, which is around twice the relative vorticity of its background. Tracking of their position shows that, overall, they drift with a mean drift rate of $\omega = -7.5 \pm 0.7°$/day, corresponding to a zonal mean velocity of $\bar{u} = -17 \pm 5$ ms^{-1}, this is, they move with the same velocity as their background. These vortices do not migrate poleward or equatoward, but instead, they follow the meandering in latitude of the hexagonal jet oscillating between 77.7°

and 78.7° and they present a life-time of at least of one month. However, the lack of intermediate images does not allow to assure a longer life-time. The presence of this type of cyclones at the same latitude over four years gives a hint of a tendency toward their formation at 78°N.

Figure 4.12 represents the latitudinal location of the cyclones and anticyclones described in this section, as well as their mean zonal velocity and their relative vorticity compared to their background values.

4.2.2 Puffy Clouds

Unlike vortices, which are observed at various latitudes on Saturn (Vasavada et al., 2006; Trammell et al., 2014; Antuñano et al., 2015, 2017), the field of compact clouds (see figure 4.13) is only observed at the poles. These small compact cloud fields cover these regions since the first images captured by the Voyagers in 1980 and 1981 and are also observed by Cassini VIMS at 5 μm wavelength (as opacity to the thermal radiation), which senses $3-4$ bar altitude, during Saturn's north polar winter (Baines et al., 2009; del Genio et al., 2009) and by Cassini ISS cameras when the sunlight is illuminating the poles. They cover a region from ~ 60°N to 90°N and from ~ -57°S to 90°S, divided in two by the hexagonal jet and its counterpart in the south. The puffy cloud field is best observed in continuum band CB2 and CB3 filters, while the clouds are not visible in images from the methane absorption band filters (MT2 and MT3) and violet filter (VIO), indicating that they are trapped at the ammonia cloud level. The structure of the compact cloud field looks similar to the cumulus clouds of closed mesoscale cellular convection (MCC) on Earth (Agee et al., 1973), but at larger scale.

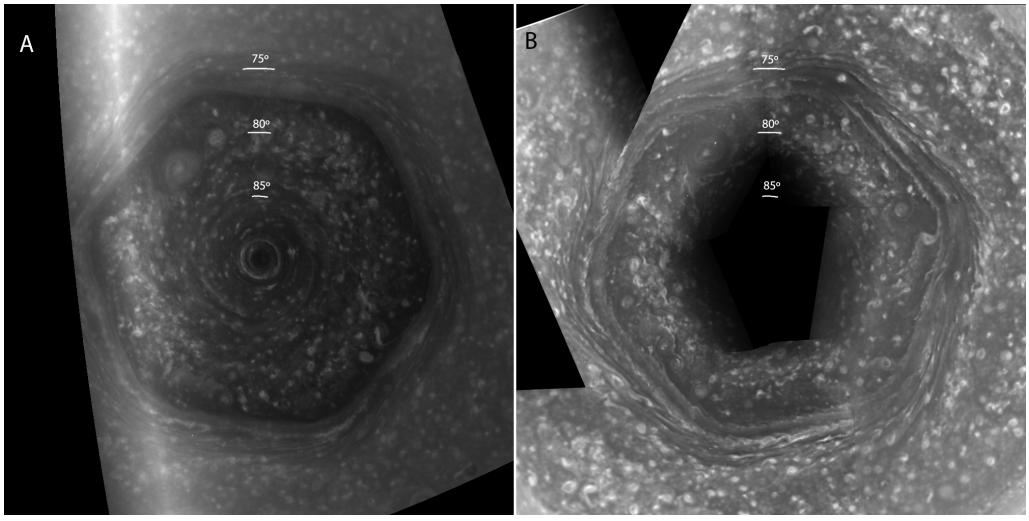

Figure 4.13: Two Polar projections from 70°N to 90°N from 25 June 2013 (left) and 3 January 2009 (Right), where "puffy clouds" are clearly seen filling the polar areas. The Polar projection of the right panel is built using five images. (Figure from Antuñano et al. (2017))

In the case of the north polar region of Saturn, CB2 and CB3 images show a $0.5° - 0.7°$ meridional width dark and cloud free region north of the Hexagon and following the hexagonal shape. Moreover, clouds are elongated due to wind shear

at latitudes higher than 84°. For this reason, in order to study seasonal variation on the number of clouds, their size and their distribution between the beginning of the northern spring and the beginning of the northern summer we concentrate in the region from 77°N to 84°N, where the clouds are not elongated. We have measured the latitude, longitude and size of each cloud at both epochs with the aim to compare the statistics of the distribution of clouds. Figure 4.13 shows two polar projection from 70° north and south to the pole, built with five CB2 images from 3 January 2009 (early spring) and one CB2 image from 25 June 2013 (early summer).

In these two epochs, January 2009 and June 2013, we detect of the order of 410 and 480 small bright clouds, respectively, from 77°N to 84°N. Their sizes vary from 10 km to 1,000 km and their separation ranges between $150-400$ km in both epochs. If we classify clouds by size (see figure 4.14a and b), we find that in January 2009 (early spring) the largest group corresponds to clouds of $200-300$ km, while in June 2013 (early summer) the peak amount of clouds is found for clouds of $10-200$ km. However, this difference might be due to the lower resolution of images from January 2009, which is around half the resolution of images from June 2013. Overall, the typical size of these clouds is around $280-340$ km, which is of the order of the thickness of the weather layer that comprises the ammonia and water clouds (from the tropopause to $\sim 10-12$ bar) (West et al., 2009), with a thickness of around $\sim 5H-6H$, where $H \sim 50$ km is the scale height. As shown in figure 4.14g and figure 4.14h, no relationship between the sizes and latitudinal bands is observed at any of the studied epochs.

In addition, we see that the clouds in June 2013 are homogeneously distributed in latitude, while in January 2009 there is a significant decrease on the number of clouds in the latitudinal bands between 77° and 78° and between 82° and 84°, responsible of the lower total number of clouds detected in January 2009, as shown in figure 4.14c and figure 4.14d. However, this decrease might not be real as the latitudinal band $82°-84°$ is partially in the shadow in some of the measured images from January 2009 and therefore, it was not possible to detect clouds over the entire longitudinal circle at these latitudes. The distribution in longitude and the separation between near clouds are not homogeneous, as can be seen in figure 4.14e and f and in figure 4.15. This last figure shows four different panels, two centered at 78° at separate longitudes (A and B) and the other two centered at 80°, again at different longitudes (C and D). Both pairs of images show clearly how the density of clouds at a given latitude is not uniform.

The shape of these small bright clouds vary from cloud to cloud. Many present a ring-like shape, or spiraling features suggestive of rotation. Unfortunately, we have not been able to measure the vorticity of these compact clouds due to the resolution of the images and the small size of the clouds.

Furthermore, cloud-tracking of these puffy clouds is extremely difficult, since they change, merge or disappear due to shear in a maximum of few days. We can estimate the life-time of the small clouds before breaking due to horizontal wind-

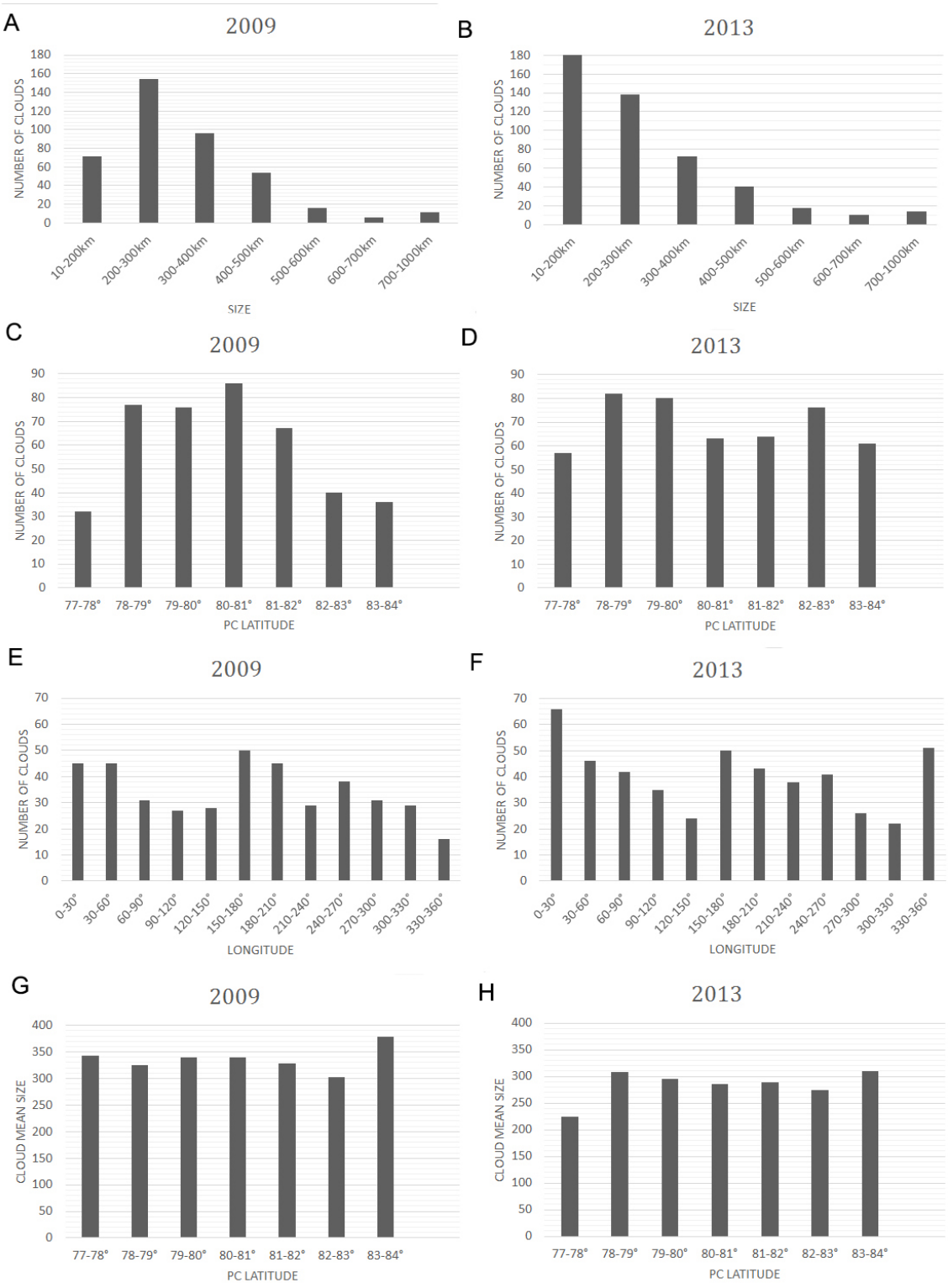

Figure 4.14: Analysis of the size and distribution of the polar compact cloud field for January 2009 (left) and June 2013 (right). Panels A and B show the number of clouds of different sizes, panels C and D show the latitudinal distribution of the "puffy clouds", panels E and F present the longitudinal distribution of these clouds and panels G and H show the mean sizes for particular latitudinal bands. (Figure from (Antuñano et al., 2017))

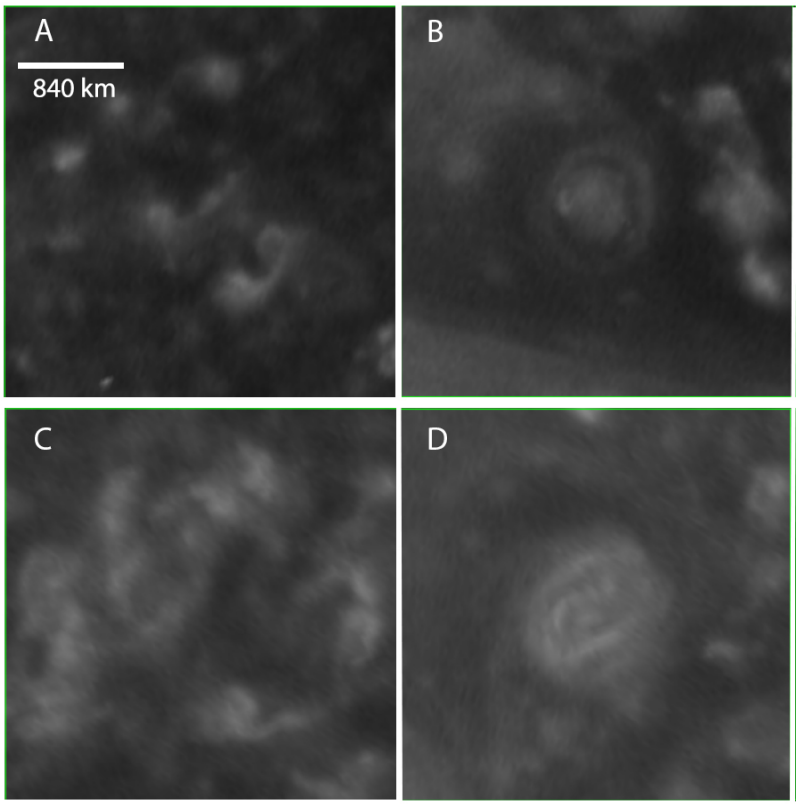

Figure 4.15: Cloud morphology of the "puffy cloud" field. The fours panels are 353×353 pixel boxes of CB2 polar projections with meridional resolution of 0.01°/pixel from 25 June 2013. The boxes are centered at: A) 78° latitude and 165° longitude, B) 78° latitude and 193° longitude, C) 80° latitude and 6° longitude and D) 80° latitude and 341° longitude.

shear, as $\tau_L = 1/(du/dy)$, of less than 2 days at latitudes between 78° and 79° and between 80° and 84°, while it could be as large as 7-9 days at latitudes between 79° and 80°. Moreover, taking into account the velocity difference and the separation between two or more clouds, we can estimate the life-time of a single cloud due to merger with other clouds as approximately $5 - 16$ hours. Thus, cloud-tracking of these puffy clouds is extremely difficult, as they change, merge or disappear in a maximum of few days.

Finally, with the aim of establishing if there is a meridional drift of the clouds, we have tracked, despite the difficulties, the displacement of 24 small clouds located between 77° and 85° during 5 days in images from 21 to 26 January 2014. Further identifications were not possible due to the rapid change of the clouds. During these five days, all the tracked clouds moved with the background and their mean meridional velocity was $\bar{v} = 0.7 \pm 2.2$ ms^{-1}, showing that during the tracked period the clouds do not migrate significantly towards the pole or toward the equator.

4.3 North Polar Vortex

Various planets from the Solar System present polar vortices (vortices centered at the poles or close to it). Earth's and Mars' polar vortices have a strong seasonal

dependence widening and weakening (and in the case of Mars even vanishing) with seasons (Mitchell et al., 2014). Venus has two polar vortices, which show a highly variable cloud morphology varying from a single vortex, a dipole shape or more complex forms (Piccioni et al., 2007; Luz et al., 2011; Garate-Lopez et al., 2013). At the outer planets, polar vortices have been detected by Cassini in Saturn and its largest moon Titan, where a vortex started to develop when it reached winter season (Teanby et al., 2010). Juno has shown no hint of a polar vortex in Jupiter (Bolton et al., Science, in the press).

Saturn's polar vortices where first detected in the Cassini era (first form Earth and later by Cassini). Images captured in the thermal middle-infrared with the Keck I Telescope in Hawaii in February 2004, showed that the south pole was warmer than its surroundings suggesting a presence of a polar vortex (Orton and Yanamandra-Fisher, 2005). Around five moths later, right after Cassini's orbit insertion in 1 July 2004, ISS high-resolution cameras captured Saturn's south pole, confirming the existence of a polar vortex (Sánchez-Lavega et al., 2006). Higher resolution images from October 2006, showed an eye-like structure with a darker almost cloud free region at the center surrounded by a brighter clouds at $-88°$ moving at velocities of ~ 150 ms^{-1} (Dyudina et al., 2008). Before Saturn equinox, when the north polar region was still not illuminated by the Sun, thermal infrared images from March 2007 showed an increase of temperature at the north pole suggesting a presence of a polar vortex at the north pole (Fletcher et al., 2008). Around a year later in June 2008, VIMS images captured in 5 μm wavelength, confirmed the presence of a North Polar Vortex (NPS) with a fast eastward jet moving at ~ 140 ms^{-1} at $\sim 88°$ latitude (Baines et al., 2009). After Saturn's equinox in 2009, ISS cameras have captured high-resolution images of the north polar vortex and have enabled a detailed characterization of its cloud morphology and dynamics (Antuñano et al., 2015; Sayanagi et al., 2016, 2017). In this section we will detail this characterization of the north polar vortex, together with its horizontal wind structure and we will compare it to the south polar vortex.

4.3.1 Cloud Morphology and Observed Temporal Variation

After Saturn's equinox in 2009, Cassini started a phase of almost equatorial orbits and it was not until late 2012 that it was able to image the north polar region again. Between late 2012 and late 2014, Cassini imaged the North Polar Vortex (NPV) with both NAC and WAC cameras in all their filters (from ultraviolet to near-infrared) showing the morphology of the polar vortex at different altitude levels and at different epochs. Figure 4.16 shows a section of these images, showing the evolution of the vortex in a selection of filters and at four separate dates.

The NPV is a stable almost circular vortex that expands from 88.5°N to 90°N. In CB2 images, where we sense the upper cloud level of the troposphere, the vortex appears as a depressed region, whose center, surrounded by spiraling bright clouds, appears to be deeper in the troposphere. In fact, in some NAC CB2 images from

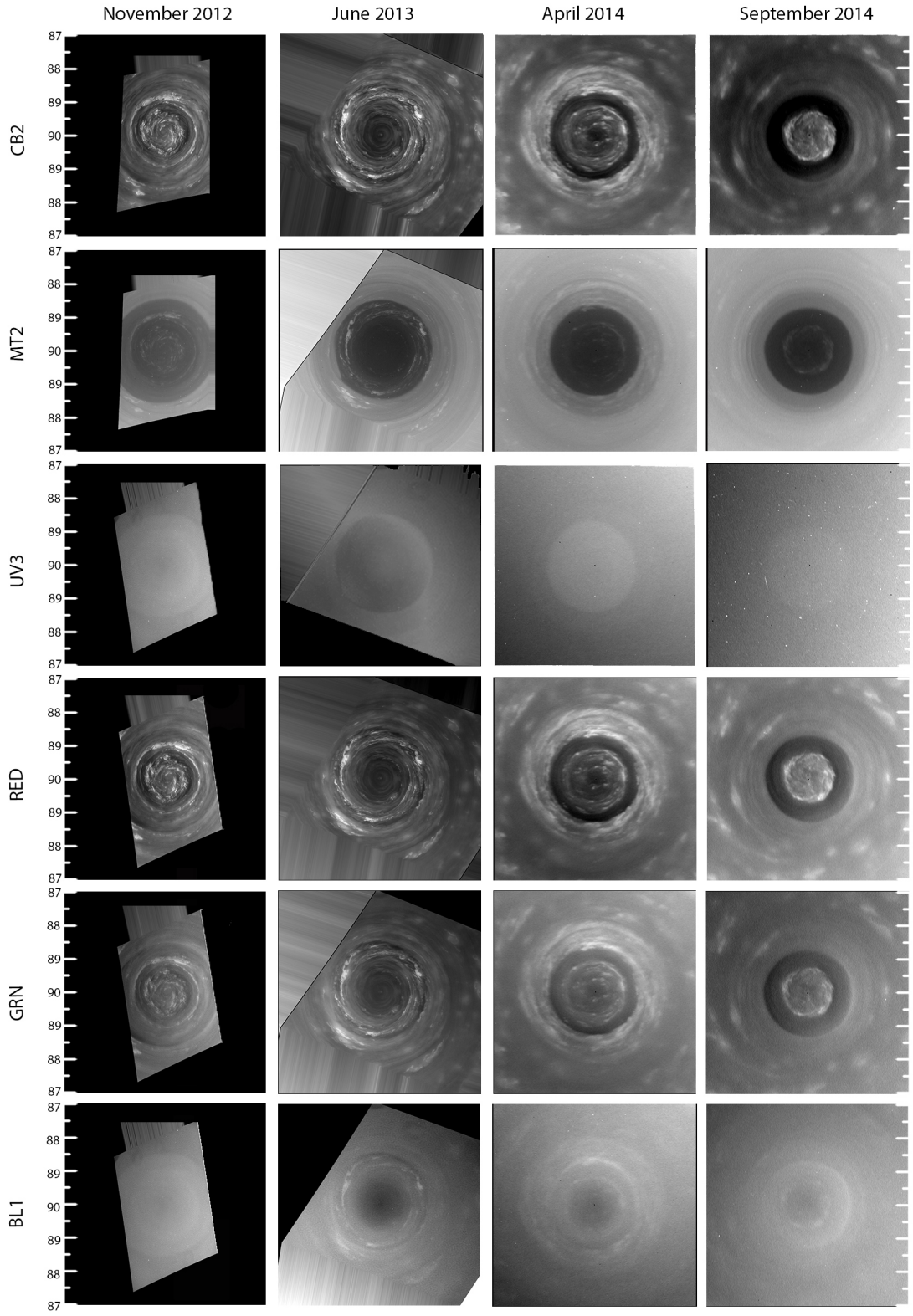

Figure 4.16: Temporal variation of the cloud morphology of the North Polar Vortex (NPV) shown in 0.005 °/pixel meridional resolution polar projections from 87° to the pole of NAC images from 27 November 2012, 14 June 2013, 2 April 2014 and 10 September 2014 in 6 different wavelengths. (Figure from Antuñano et al. (2017))

June 2013, there are dark regions in the "wall" that form the spiraling clouds, which are identified as the shadows of higher clouds confirming that clouds at the center are deeper. In the methane absorbing filter MT2, images show a dark almost circular region without many contrasted features expanding to $\sim 88.5°$N, as the thicker layer of tropospheric haze absorbs most of the light at those wavelengths. Similarly, in ultraviolet images the NPV appears bright due to the Rayleigh scattering by the haze. Blue, green and red (BL1, GRN and RED) filters shows a transition from highly absorbing to penetrating filters.

Although the vortex' size and its circular shape have remained stable since the first images, its morphology at cloud level experimented important changes. Figure 4.16 shows a rapid variation at various wavelengths between November 2012 and September 2014. CB2 images from November 2012 show the polar vortex as an "eye-like" structure formed by bright spiraling clouds. However, in CB2 images from June 2013, the bright spiraling clouds found at the vortex' center in November 2012 disappear, uncovering deeper spiraling clouds at its center. Almost a year later, the morphology of the polar vortex in April 2014 appears different again. CB2 images of this epoch show a formation of a new dark and cloud free almost circular region of $\sim 0.3°$ radius centered at the pole surrounded by bright spiraling clouds down to 89°N. Encircling this bright region down to 88.7°N a new dark, cloud free ring-like area appears followed by a bright spiraling 1° width zone. Finally, by September 2014, a bright circular area of spiraling clouds extends from the center of the vortex down to 89.2°N and the dark ring observed on images from April 2014 becomes wider expanding down to 88.7°. Moreover, the bright region that surrounded the dark ring on April 2014 becomes darker and plainer.

MT2 images from November 2012 show a dark, almost cloud free circular region expanding from the pole down to 88.5°N. Nevertheless, these images show brighter spiraling clouds inside the dark region, corresponding to some of the bright features of CB2 images, and thus indicating that those features are higher clouds in the atmosphere. In June 2013, the size of the dark circular region remains unchanged, however, its center appears darker almost without any brighter clouds. Images from April and September 2014 show that the dark region reduced 0.2° extending from the pole down to 88.7°. Moreover, some brighter clouds appear in the center, not present in June 2013.

4.3.2 Horizontal Wind Field and Vorticity

The dynamics of the poles in fast-rotating Giant planets is clearly conditioned by the Coriolis force as it reaches high values at these latitudes. In the case of the north polar region of Saturn, as described in chapter 3, the averaged zonal wind profile of the polar jet has an asymmetric shape. Poleward of 80° latitude, where it reaches its minimum of ~ 5 ms^{-1}, it increases with latitude reaching ~ 140 ms^{-1} at 88.5° and then, it starts a rapid and almost linear decrease with latitude to 0 ms^{-1} at the pole (Baines et al., 2009; Antuñano et al., 2015; Sayanagi et al., 2017).

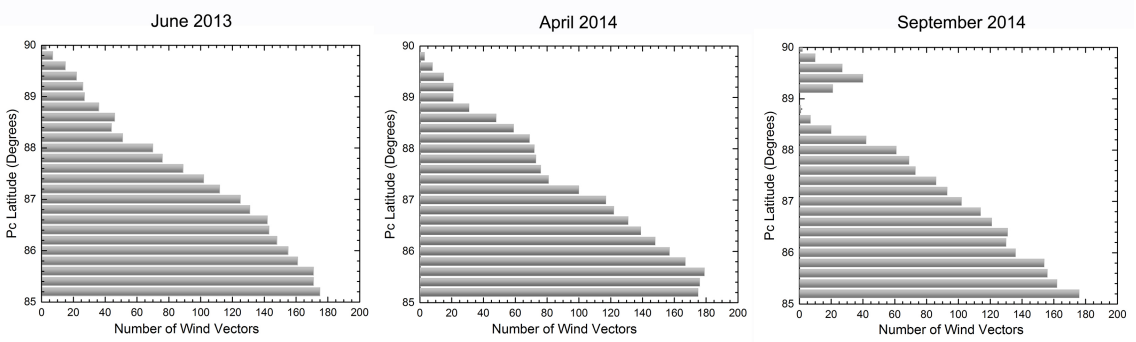

Figure 4.17: Distribution of the obtained wind measurements in 0.2° latitude bins for June 2013, April 2014 and September 2014.

Given the strong changes in morphology in the polar vortex between November 2012 and September 2014, the question arises whether those changes are due to some change in the dynamics of the regions. In order to check this point, we have compared the horizontal wind field, relative vorticity and divergence between June 2013, April 2014 and September 2014 by measuring by cloud tracking and with the brightness correlation software two new image pairs from April and September 2014. The two measured image pairs are: (a) one CB2 image pair separated by 38.77 minutes from 2 April 2014 and (b) one CB2 image pairs separated by 45.33 minutes from 10 September 2014. In total, we have obtained $3,323$ wind vectors from 85° to 90°: (i) $1,171$ from June 2013, (ii) $1,140$ from April 2014 and (iii) $1,012$ from September 2014. Figure 4.17 represents the number of wind vectors in 0.2° latitude bins. The absence of measured wind vectors between 88.6° and 89.2° in September 2014 corresponds to the cloud-free dark ring observed in CB2 images (see figure 4.16).

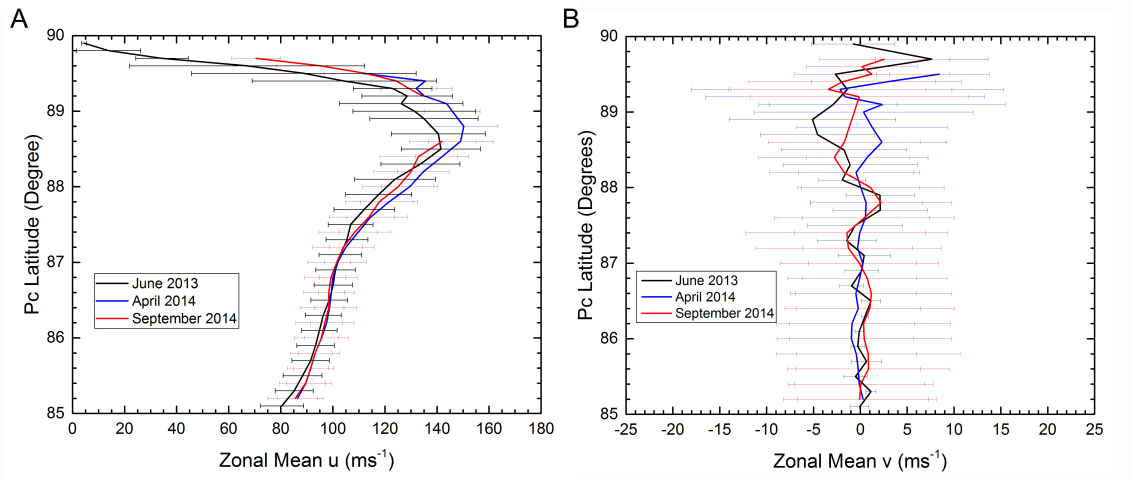

Figure 4.18: Zonally averaged zonal velocity (a) and meridional velocity (b) from 85°N to 90°N from June 2013 (black), 2 April 2014 (blue) and 10 September 2014 (red).

Figure 4.18 presents the zonally averaged horizontal wind field of the North Polar Vortex between 85°N and 90°N for June 2013, 2 April 2014 and 10 September 2014,

where zonal and meridional velocities have been binned in 0.2° latitude using moving bins of 0.4° between 85°N and 89°N and in 0.1° latitude with moving bins of 0.2° at higher latitudes. This figure shows that the zonally averaged horizontal wind field remains unchanged over these epochs, reaching a peak velocity of $140 - 150$ ms^{-1}. The zonal mean velocity profile of the North Polar Vortex from November 2012 obtained by Sayanagi et al. (2017) presents higher values than the ones presented in this section, reaching values of 165 ± 16 ms^{-1}. However, this difference may not be real and it might be due to the higher resolution images (2 km compared to $4 - 16$ km) and spatial averaging (0.01° latitude) used by Sayanagi et al. (2017).

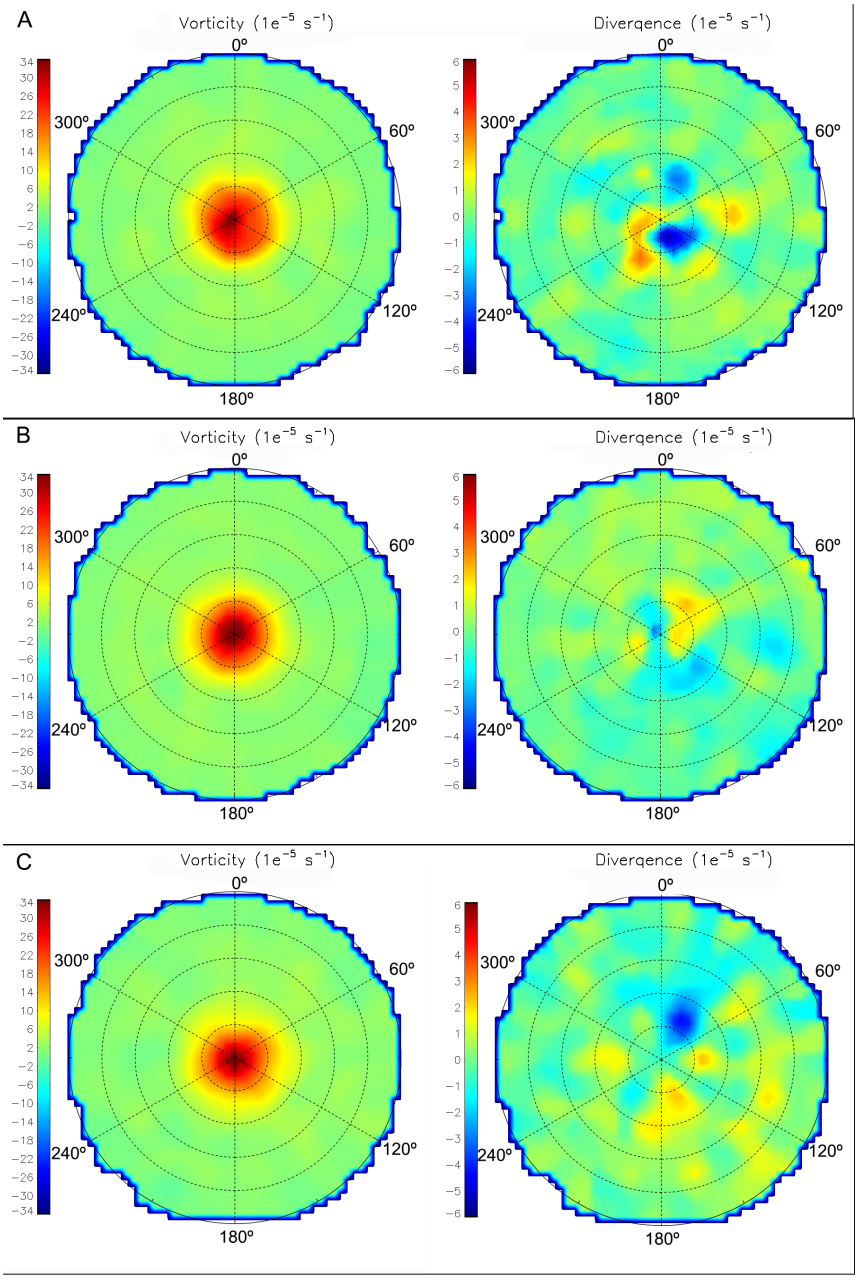

Figure 4.19: Relative vorticity (left) and divergence (right) maps of the north polar region from 85° to the pole for June 2013 (a), April 2014 (b) and September 2014 (c). The dashed circles represent the latitude between 85° and 90° every 1° latitude.

Finally, we present in figure 4.19 relative vorticity and divergence maps of the NPV for June 2013 and April and September 2014. These maps have been built following the steps described in chapter 3. However, in order to analyze in detail these two magnitudes at the North Polar Vortex, we have interpolated the data into a regular grid with $\triangle X \sim \triangle Y \sim 190$ km (which corresponds to $\sim 0.2°$) and averaged it over $\sim$ 760km, instead of the lower resolution interpolation and the stronger smoothing performed to analyze the general dynamics of the polar regions (see chapter 3), where the lower image-resolution of the images used to analyze the dynamics at lower latitudes did not allow a more detailed interpolation. The lower spatial averaging of the data will result in greater values of the relative vorticity obtained in this section, which we believe are closer to the "real" values.

Figure 4.19 shows that, at these three epochs, the relative vorticity does not change significantly, reaching values of $10 \pm 1 \times 10^{-5}$ s^{-1} at 88.5°, which is approximately 1/4 of the Coriolis parameter at this latitude and increasing rapidly with latitude until 33×10^{-5} s^{-1} at the pole, that is, values of the order of magnitude of the Coriolis parameter. The lower vorticity values between 88.6° and 89.2° in figure 4.19c (September 2014) are not significant due to the absence of wind vectors at these latitudes. The relative vorticity values of this region from November 2012 obtained by Sayanagi et al. (2017) are twice the values presented in this study. However, this might be due to the higher resolution of spatial averaging of their data and due to the fact that they do not smooth the data.

The divergence in this region is considerably smaller than the relative vorticity at all the studied epochs, oscillating around zero.

4.3.3 Comparison to the South Polar Vortex

The South Polar Vortex (SPV), discovered before the North Polar Vortex in Cassini images from July 2004 (Sánchez-Lavega et al., 2006), is very similar to the vortex found at the north pole (Antuñano et al., 2015; Sayanagi et al., 2017) as can be seen in figure 4.20. In CB2 high resolution images from October 2006 and July and December 2008, it has an "eye-like" almost circular shape with fast bright spiraling clouds at 88.5°S (Dyudina et al., 2008; Antuñano et al., 2015; Sayanagi et al., 2017). This polar vortex, at this wavelength, seems less populated of clouds and looks plainer than the NPV. However, this might be due to the viewing angle condition of the south polar images. Similar to the NPV, in MT2 images, the south polar vortex is seen as a dark almost circular region without any contrasted features inside it, confirming that it is located at a depressed region of the atmosphere, and in VIO images it is seen bright due to the Rayleigh scattering.

The dynamics of the SPV is also very analogous to that of the NPV, reaching similar velocity and vorticity values. The polar eastward jet accompanying the south polar vortex has a velocity peak of 157 ± 12 ms^{-1} located at the same latitude as the NPV, but in the southern hemisphere (88.5°S). Poleward this latitude the velocity decreases rapidly as in the north polar region. It reaches a vorticity value

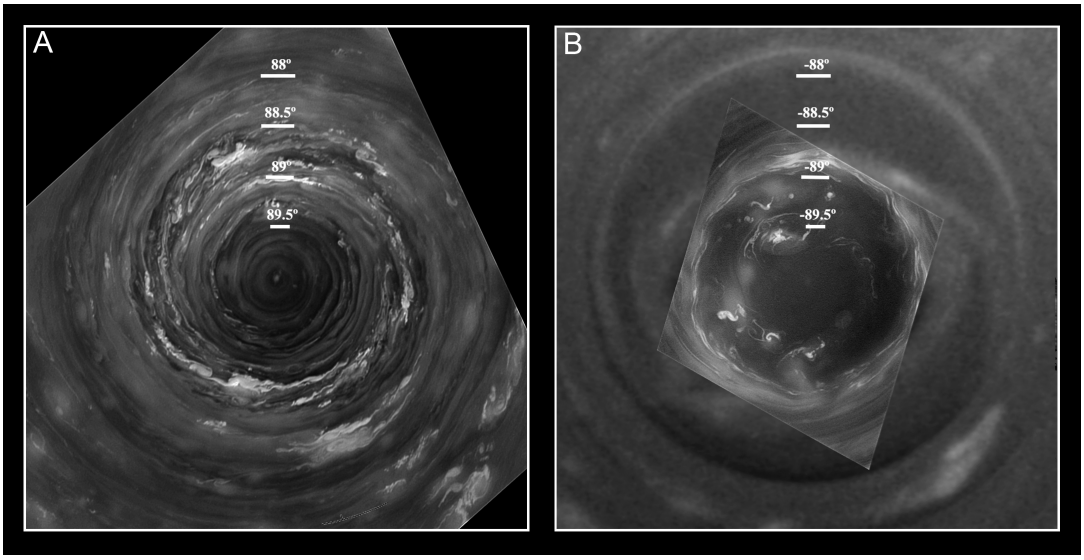

Figure 4.20: Polar projections of the north (left) and south (right) polar regions from 87.5° to the pole from 14 June 2013 (left) and 14 July 2008 (right) showing the North and South Polar vortices in CB2 images. Panel B is a composition of two different images with different resolutions. The image in the back is a CB2 WAC image of spatial resolution of 295 km/pixel, while the image in the front is a CB2 NAC image of spatial resolution 2.4 km pixel. (Figure from Antuñano et al. (2015)).

of $-10 \pm 1 \times 10^{-5}$ s^{-1} at -88.5°S , 1/3th of the Coriolis parameter at that latitude, and it increases with latitude reaching a vorticity of $-23 \pm 2 \times 10^{-5}$ s^{-1} at the pole. The zonal wind profile and the vorticity map are shown in figure 4.21.

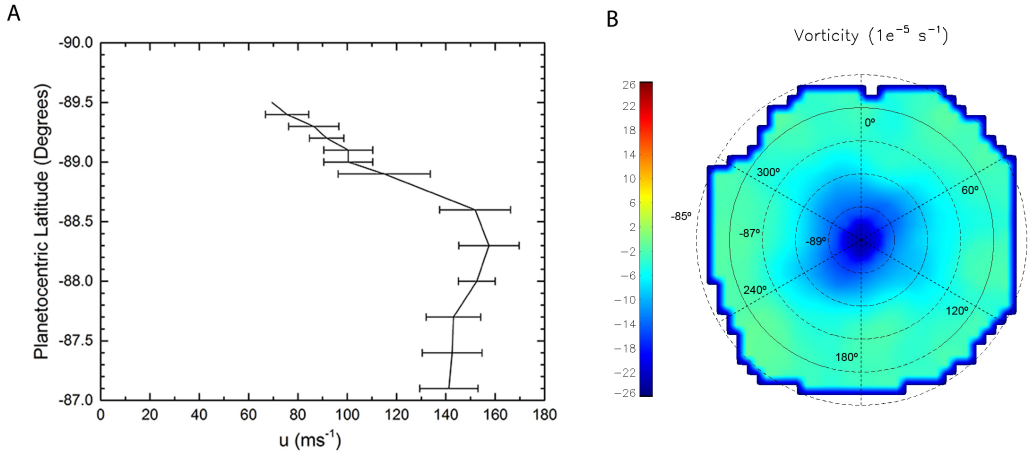

Figure 4.21: Panel A is an enlargement of figure 3.6, showing the averaged zonal velocity profile of the south polar region from 87°S to 90°S. Panel B shows the vorticity of the south polar region from 85°S to the pole.

4.4 Discussion

Saturn takes around 30 Earth years to orbit the Sun, each of its seasons lasting a little bit longer than 7 years. Its long seasons and the tilt of the rotation axis of

the planet (26.7°) result in strong seasonal variations on Saturn's stratosphere and upper troposphere (above about $1-2$ bar pressure level), exacerbated in the equator by the shadow of the rings. However, a long-term study of the north polar region of Saturn has shown that the Hexagon, the "puffy" cloud field and the dynamics of the North Polar Vortex (NPV) do not vary with seasons. Variability has been observed in the cloud cover of the NPV between late 2012 and 2014 and cloud morphology at the hexagon but on temporal scales much shorter than those expected for seasonal radiative forcing (e.g. the radiative time constant). Moreover, the "puffy" cloud field, the Hexagon, and the North Polar Vortex are also present in Saturn's atmosphere during the long north polar winter, as observed by Cassini VIMS at 5 m. These results favor the hypothesis that the dynamics of the polar regions beneath the upper ammonia cloud is driven by the internal heat source. In the case of the Hexagon, its unchanged aspect and dynamics against seasonal forcing together with the very small phase velocity in system III suggests that the rotation period of the Hexagon could represent the rotation period of Saturn's internal "solid body", with the hexagon then assumed to be rooted to the deep atmosphere and interior.

The study of the motion and cloud morphology of the "puff" cloud field indicates that their life time is of the order of a few days due to wind shear, mutual interactions and mergers, and it suggests that the larger cyclones and anticyclones present at Saturn's polar regions, that we have called "regular vortices" are probably formed by the accumulative mergers of the "puffy" clouds.

Finally, the study of Saturn's polar vortices is of great interest, since they form under very different dynamical conditions to those of the terrestrial planets. Very recent discoveries by JUNO have shown that although Jupiter's polar regions are covered by discrete cyclones rotating around the poles, there are no polar vortices in Jupiter (Bolton et al. Science in press May 26th, 2017). This difference in the polar dynamics between the two giant planets was proposed in a numerical shallow water layer model by O'Neill et al. (2015), which was able to reproduce the formation of a polar vortex on Saturn as the merger of multiple storms originated by moist convection and located near the poles. These storms should drift in Saturn due to the beta effect toward the poles, transporting and depositing there their cyclonic vorticity. The lack of polar vortices on Jupiter could then simply explained as due to the small beta-drift in this planet.

The visual aspect of the compact "puffy" cloud field described above resemble the small cyclonic storms required by O'Neill et al. (2015). model. However, we have not been able to detect the drift to the north neither of the smaller puffy clouds nor of the singular vortices found at the north polar region, and therefore we are not able to confirm or support this model.

Chapter 5

Interpretation of the Hexagon

Over the last decades, different hypothesis have been proposed to explain the nature and origin of the Hexagon. Allison et al. (1990) proposed that the Hexagon is a stationary Rossby wave formed by the interaction of the eastward jet with one or more vortices located right to its south. In their model, they argued using the horizontal wind field obtained by Godfrey (1988), that the Rossby phase speed for barotropic waves harmonic in longitude and latitude is zero, implying a stationary wave pattern. Moreover, assuming that the vortex impinging on the jet creates a stationary perturbation and that the vertical structure is related to the zonal wavenumber, they calculated the vertical eigenvalue of the quasi-geostrophic potential vorticity and found that the wave is vertically trapped within a region of positive static stability. From these results, they suggested that the nature of the Hexagon could be forced at deep levels due to the planet's interior convection. This hypothesis was compromised with the observation that although the north polar vortex (NPS) or any other vortex is not present right outside the Hexagon, the Hexagon remains unchanged, in contradiction to their model, which needs the continuum presence of the vortex for the Hexagon to remain present.

Sánchez-Lavega et al. (2014), confirmed that the motion of the vertices of the Hexagon was almost stationary in System III, and analyzing the three-dimensional dispersion equation for a Rossby wave, argued that the Hexagon is compatible with a free Rossby wave, with no need of forcing. Again, the vertical structure of the wave is trapped in a region of positive static stability, whose velocity could represent the rotation of the interior of Saturn. This model is detailed below.

An alternative explanation for the origin of the Hexagon was presented by Barbosa-Aguiar et al. (2010). They proposed that the Hexagon could be originated from a barotropic instability. In their study, they performed fluid dynamical laboratory experiments in a rotating tank, showing that a quasi-geostrophic and barotropic atmosphere could form a hexagonal vortex street. They also computed a linear barotropic instability analysis taking into account the zonal velocity profile of the Hexagon measured by Sánchez-Lavega et al. (2000). Their results show that for a Rossby deformation radius $L_D = NH/f$ (where $N = \left(\frac{g}{T}\left(\frac{dT}{dz} + \frac{g}{C_p}\right)\right)^{1/2}$ is the Brunt-Väisälä frequency, $H = R^*T/g$ is the scale-height and $f = 2\Omega \sin\phi$ is the

Coriolis parameter) of $L_D = 2500$ km, the maximum growth rate occurs for a zonal wavenumber of 6. However, in the same study, an analysis of the eastward jet at 70.4°S shows that the maximum growth does not peak at any specific wavenumber and that overall the growth rate is weaker. An important difference between their laboratory experiment's results and the observations is the vortex street formed, and not observed in Saturn's Hexagonal feature, which arises as a consequence of the meandering of the jet (Antuñano et al., 2015).

Morales-Juberías et al. (2011, 2015) performed numerical simulations using the Explicit Planetary Isentropic-Coordinate EPIC-General Circulation Model (Dowling et al., 1998) in order to study the instability arising from an eastward jet. In their models, they use a jet with a horizontal wind structure of a Gaussian shape that violates the Rayleigh-Kuo criterion for barotropic stability and the Charney-Stern criterion for baroclinic stability. In their first model (Morales-Juberías et al., 2011), they assumed a deep jet and their results showed that the final wavenumber depends on the width of the zonal jet. In their simulations, a vortex street was formed, moving than at the observations (Sánchez-Lavega et al., 2014). In a later work (Morales-Juberías et al., 2015), they assume, instead, a shallow jet, whose velocity decreases with pressure, vanishing at 10 bar. Their results show that for a specific form of the vertical wind shear and the zonal velocity profile at its base, the jet becomes unstable and meanders forming a hexagonal pattern, moving with a similar phase speed to the observed one.

The actual origin of the Hexagon is still a subject of open debate and none of the hypothesis proposed is conclusive enough. Here, we analyze different interpretations for the origin of the Hexagon. First, we review the hypothesis of Sánchez-Lavega et al. (2014) that considers the Hexagon as a deep-rooted Rossby wave that could be a manifestation of a deep unstable jet. Then, we introduce a numerical analysis of the fastest growing modes of the barotropic and baroclinic instabilities for the Hexagon jet and its counterpart in the south, in an attempt to elucidate the differences that may give rise to a well formed wave in the north and not in the south.

5.1 A free Rossby Wave

In our study (Sánchez-Lavega et al., 2014), we analyzed the three-dimensional dispersion equation for a free Rossby wave in order to analyze the vertical structure and the sign of the vertical wavenumber (m^2) for the hexagonal eastward jet at 75.8°N, assuming that the motion of the vertices of the Hexagon reflects the phase speed of the three-dimensional Rossby wave and that the side of Hexagon and the width of the jet provide an estimation of the zonal and meridional wavelengths.

Rossby waves can be seen as arising as a consequence of the conservation of the potential vorticity. Due to Saturn's rapid rotation rate, the quasi-geostrophic approximation is valid ($R_0 = NH/F << 1$, where R_0 is the Rossby number). Within this approximation, the quasi-geostrophic potential vorticity q_g is conserved

in geostrophic motion and therefore, we have

$$\frac{D_g q_g}{Dt} = 0 \tag{5.1}$$

where, $\frac{D_g}{Dt} = \frac{\partial}{\partial t} + u_g \frac{\partial}{\partial x} + v_g \frac{\partial}{\partial y}$ is the advective derivative following geostrophic motion and

$$q_g = f_0 + \beta y + \left[\nabla^2 + \frac{\partial}{\partial z} \left(\frac{f_0^2}{N^2} \frac{\partial}{\partial z} \right) \right] \Psi \tag{5.2}$$

(Pedlosky, 1987; Vallis, 2006; Sánchez-Lavega, 2011) is the quasi-geostrophic potential vorticity (analogue to equation 3.16, but expressed in terms of the geostrophic streamfunction Ψ).

In this expression, the Coriolis term f has been expanded using the β-plane approximation ($f = f_0 + \beta y$). The geostrophic streamfunction verifies:

$$u_g = -\frac{\partial \Psi}{\partial y} \qquad v_g = \frac{\partial \Psi}{\partial x} \tag{5.3}$$

In order to solve equation 5.2, we linearize Ψ decomposing it as the sum of a fixed Ψ_0 plus a small perturbations Ψ':

$$\Psi = \Psi_0 + \Psi'. \tag{5.4}$$

We consider a basic reference atmosphere with purely zonal motion $u(y)$ and constant static stability. The geostrophic unperturbed streamfunction is accordingly to 5.3

$$\Psi_0 = -\int u(y) \mathrm{d}y \tag{5.5}$$

which is a trivial solution of equation 5.2. Ignoring second order terms in Ψ', equation 5.2 becomes:

$$\left(\frac{\partial}{\partial t} + \bar{u} \frac{\partial}{\partial x} \right) \left[\nabla^2 \Psi' + \frac{\partial}{\partial z} \left(\frac{f_0^2}{N^2} \frac{\partial}{\partial z} \right) \Psi' \right] + \left(\beta - \frac{\partial^2 \bar{u}}{\partial^2 y} \right) \frac{\partial \Psi'}{\partial x} = 0. \tag{5.6}$$

We seek for a plane wave solution of this equation of the form

$$\Psi' = \mathrm{Re} \left(\Psi_0' \exp \left[\left(\frac{z}{2H} \right) + i \left(kx + ly + mz - \omega t \right) \right] \right), \tag{5.7}$$

where $k = 2\pi/L_x$, $l = 2\pi/L_y$ and $m = 2\pi/L_z$ are the zonal, meridional and vertical wavenumber, respectively, and ω is the wave frequency. Introducing equation 5.7 into equation 5.6 gives the three-dimensional dispersion relationship

$$c_x - \bar{u} = -\frac{\beta - \frac{\partial^2 \bar{u}}{\partial^2 y}}{k^2 + l^2 + (m^2 f_0^2/N^2) + 1/4L_D^2} \tag{5.8}$$

where $c_x = \omega/k$ is the zonal phase speed of three-dimensional Rossby wave (Sánchez-Lavega et al., 2014).

If the local Coriolis parameter (f_0) is much smaller than the Brunt-Väisälä frequency (N), then, the dispersion relationship 5.8 does not depend on the vertical structure and it reduces to the barotropic case (see the following section).

Measurements of the velocity of the vertices of the Hexagon in images captured with ground-based telescopes between 2008 and 2014, show that the Hexagon's speed relative to System III is -0.036 ms^{-1}. Assuming this value as the zonal phase speed (c_x) of the Rossby wave, $L_D = 1,000$ km (Read et al., 2009b), $\bar{u} = 120$ ms^{-1}, $< d^2u/d^2y >= -7 \times 10^{-11}$ m^{-1}s^{-1} and calculating k and l by using the Hexagon side $L_x = 14,500$ km and its meridional extent ($\sim 3°$) $L_y = 5,785$ km, we obtain $m^2 < 0$. This implies that the Rossby wave does not propagate in the vertical direction and therefore, it is vertically trapped in a region of positive static stability in Saturn's atmosphere. The vertical extent of the wave is unknown and not determined by this analysis. However, since the Hexagon has remained unchanged over 36 years and it has survived the long north polar winter, we suggested that it could extend well below 10 bar (Sánchez-Lavega et al., 2014).

5.2 Instability

The study of the stability and unstable disturbances of a jet have been largely used in order to understand and explain some meteorological features at different planet's atmospheres (Pedlosky, 1987; Vallis, 2006; Sánchez-Lavega, 2011). In particular, two kind of instabilities related to the shape of the wind velocity profile have been widely analyzed: (i) the barotropic instability and (ii) the baroclinic instability.

In this study, we follow previous works (Barbosa-Aguiar et al., 2010; Conrath et al., 1981; Godfrey and Moore, 1986) in order to analyze these two instabilities for the hexagonal jet and its counterpart in the south, using updated wind and thermal structures deduced from recent Cassini data.

5.2.1 Barotropic Instability

In a barotropic atmosphere, there are no meridional temperature gradients on constant pressure (isobaric) surfaces. Therefore, according to the thermal wind relationship (described in equation 3.13 introduced in chapter 3.5.1) there is no vertical wind-shear and the velocity has only meridional dependence, $u = u(y)$. In these

cases, the instability arises according to the meridional wind shear of the flow.

As mentioned in chapter 3.4, a necessary, but not sufficient condition for a barotropic instability to grow in a zonal jet is $\beta - \partial\bar{u}^2/\partial y^2 > 0$ in the studied domain (Sánchez-Lavega, 2011), which is clearly satisfied at the flanks of the Hexagon jet and its counterpart at 70.4°S (see figure 3.9).

In this section, we perform a linear numerical analysis of the barotropic instability for the hexagonal jet and its counterpart in the south. As before, we work in the beta plane approximation, and we assume a quasi-geostrophic barotropic fluid. We follow Barbosa-Aguiar et al. (2010), to try to explain the hexagonal shape in the northern jet and its absence in the south. For this purpose, we use the zonal wind profile from Antuñano et al. (2015) presented in chapter 3.

Once again, we use the conservation of the quasi-geostrophic potential vorticity equation (equation 5.1). However, this time, we assume a shallow water barotropic and inviscid flow and thus, we use the shallow water version of the quasi-geostrophic potential vorticity, which can be written as

$$q' = \nabla^2\Psi + \beta y - 1/L_D^2\Psi \tag{5.9}$$

(Vallis, 2006; Sánchez-Lavega, 2011). This expression is obtained from the quasi-geostrophic potential vorticity equation (5.2) by assuming that N^2 does not vary with pressure (altitude), taking into account that the wind is in geostrophic balance (equation 1.2) and using the geostrophic streamfunction described in the previous section (equation 5.3). As before, we write the streamfuction as the sum of a basic state plus a small perturbation $\Psi = \Psi_0 + \Psi'$, where once again the unperturbed streamfuction is $-\int u(y)\mathrm{d}y$. We look for an harmonic solution of the type:

$$\Psi' = \Psi'_0(y)\exp\left[ik'\left(x - ct\right)\right] \tag{5.10}$$

where, $k' = \frac{n'}{R\cos\phi}$ is the streamwise wavenumber, n' is the zonal wavenumber, R is the planetary radius at latitude ϕ and $c = c_r + ic_i$ is the phase speed (c_r and c_i are the real and imaginary part of the phase speed).

Introducing equation 5.9 and equation 5.10 in equation 5.1 and after linearizing it, we obtain the linearized vorticity equation:

$$(\bar{u} - c)\left[\frac{\partial^2\Psi'_0}{\partial^2 y} - k'^2\Psi'_0\right] + \left[\beta - \frac{\partial^2\bar{u}}{\partial^2 y} - \frac{1}{L_D^2}\right]\Psi'_0 = 0. \tag{5.11}$$

In order to solve this equation for the velocity profile of the Hexagon and its counterpart in the south, we use the Gaussian fit of their zonal velocity profiles given in equation 4.5 introduced in chapter 4, with the parameters described in sections 4.1.2 and 4.1.4. Following Barbosa-Aguiar et al. (2010), we solve this problem for a jet extending between the latitudinal range of $-5,000$ km to $5,000$ km relative

to the velocity peak (which roughly corresponds to 71.5°N to 80.1°N) and we impose the Neumann boundary condition ($\frac{\partial \Psi_0'}{\partial y} = 0$) at the upper and lower latitudes. However, we have checked that for narrow jets, which is the case of the Hexagon and the jet at 70.4°S, Dirichlet boundary conditions ($\Psi_0' = 0$) give identical results. Finally, we approximate the derivatives with the Finite Difference Method (FMD) described in chapter 2. Once the boundary conditions are imposed, the problem becomes an eigenvalue problem that we solve inverting the corresponding matrix, using standard algebraic routines implemented in MATLAB, where $c = c_r + ic_i$, the phase speed of the perturbation, is the eigenvalue of this problem.

Taking into account the form of the trial functions (equation 5.10), we see that the perturbation grows exponentially when the imaginary part of the phase speed (c_i) is positive. In order to obtain the most unstable wavenumber and its growth rate ($\sigma = kc_i$), we must search for the eigenvalue with the largest imaginary part.

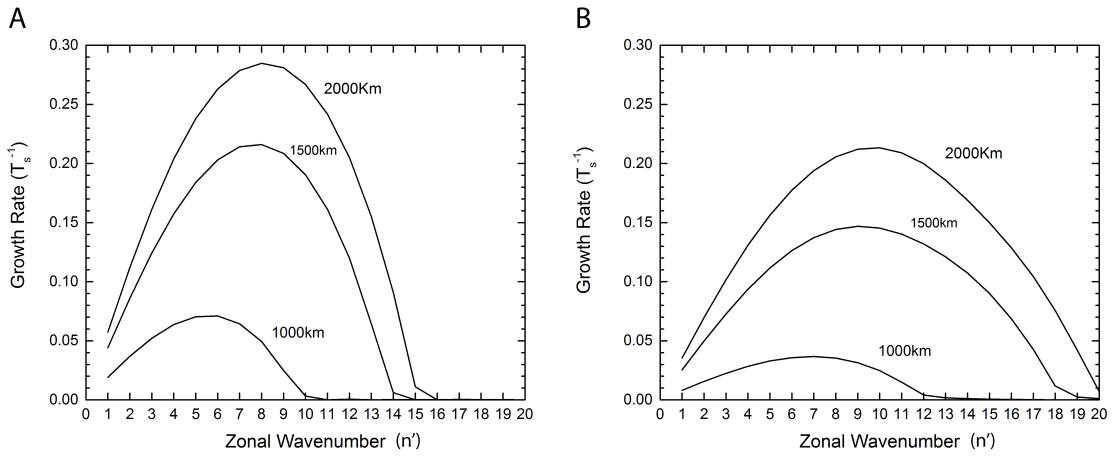

Figure 5.1: Growth rate curves of the barotropic instability for the Hexagon jet (a) and for its counterpart in the south (b) for different Rossby deformation radius. $T_s = \Omega$ in System III.

Figure 5.1, represents the growth rate curves for the Hexagon and its counterpart in the south, for different wavenumbers (n') and different values of the Rossby deformation radius (L_D). These results show that at the hexagonal jet, the growth rate peaks at a zonal wavenumber 6 with an e-folding time of ~ 14 T_s (T_s= Saturnian day) for a Rossby deformation radius of $L_D = 1,000$ km. At the counterpart in the south, using the same Rossby deformation radius there is a maximum at wavenumber 7 with a time scale of ~ 28 T_s, while for $L_D = 1,500$ km, the growth rate peaks at wavenumber 9 with a time scale of 7 T_s in the south.

These results are in agreement with the observations in the north, where the Hexagon is the manifestation of a mode 6 wave, however, there is no wave-like structure present in the eastward jet at $70,4$°S. Nevertheless, we have to point out that the results we find for the south are not necessarily in contradiction with obser-

vations, as our study does not provide information about the equilibrium amplitude of the perturbation, which could be small enough in the south to hide any wave-like pattern (see equation 4.1).

5.2.2 Baroclinic Instability

In a baroclinic atmosphere, meridional temperature gradients are present in constant pressure surfaces and thus, the vertical wind-shear is not zero ($du/dz \neq 0$) and the zonal flow depends on the meridional and vertical components ($u = u(y, z)$). In these cases, if the atmosphere is statically stable, this is, if $N^2 > 0$, a baroclinic instability can develop (Pedlosky, 1987; Vallis, 2006; Sánchez-Lavega, 2011). A necessary, but not sufficient condition for the baroclinic instability to grow, is given by the Charney-Stern instability criterion (Charney and Stern, 1962), which states that an instability can grow if the sign of the meridional gradient of the quasi-geostrophic potential vorticity changes in the studied domain. As described in chapter 3.5.2, this last condition is satisfied at cloud level at the flanks of both the Hexagon jet and the eastward jet at 70.4°S.

In order to analyze the vertical behavior of a baroclinic instability, we follow Godfrey and Moore (1986) in their one-dimensional numerical analysis of the baroclinic instability used to study the Ribbon wave, which assume a periodic perturbation in the zonal (x) and meridional (y) directions and in time (t).

In this numerical model, we use the conservation of the quasi-geostrophic vorticity equation defined in equations 5.1 and 5.2, and we write, once again, the streamfunction as $\Psi = \Psi_0 + \Psi'$. We use the same unperturbed stream function as before, but now we define the perturbed stream function as

$$\Psi' = \Psi'_0(z) \exp\left[i\left(k_x(x - ct) + k_y y\right)\right] \tag{5.12}$$

where k_x and k_y are the zonal and meridional wavenumbers (to simplify we dropped the apostrophes on k_x and k_y). Introducing the streamfunction in equation 5.2 and writing the zonal and meridional velocities in terms of the geostrophic streamfuction as $u_g = -\frac{\partial \Psi}{\partial y}$ and $v_g = \frac{\partial \Psi}{\partial x}$, we can develop equation 5.1 to obtain the linearized vorticity equation by neglecting the second order or higher terms (Godfrey and Moore, 1986):

$$(\bar{u} - c)\left[f^2 \frac{\partial}{\partial z}\left[\frac{\partial \Psi'_0/\partial z}{N^2}\right] - \left(k_x^2 + k_y^2\right)\Psi'_0\right] + \left[\beta - \frac{\partial^2 \bar{u}}{\partial y^2} - f^2 \frac{\partial}{\partial z}\left[\frac{\partial \bar{u}/\partial z}{N^2}\right]\right]\Psi'_0 = 0. \tag{5.13}$$

Before solving this equation we need to introduce the boundary conditions for this problem. For this purpose, we analyze the simplest baroclinic instability model, the Eady model (Eady, 1949), where the disturbance is confined between two horizontal

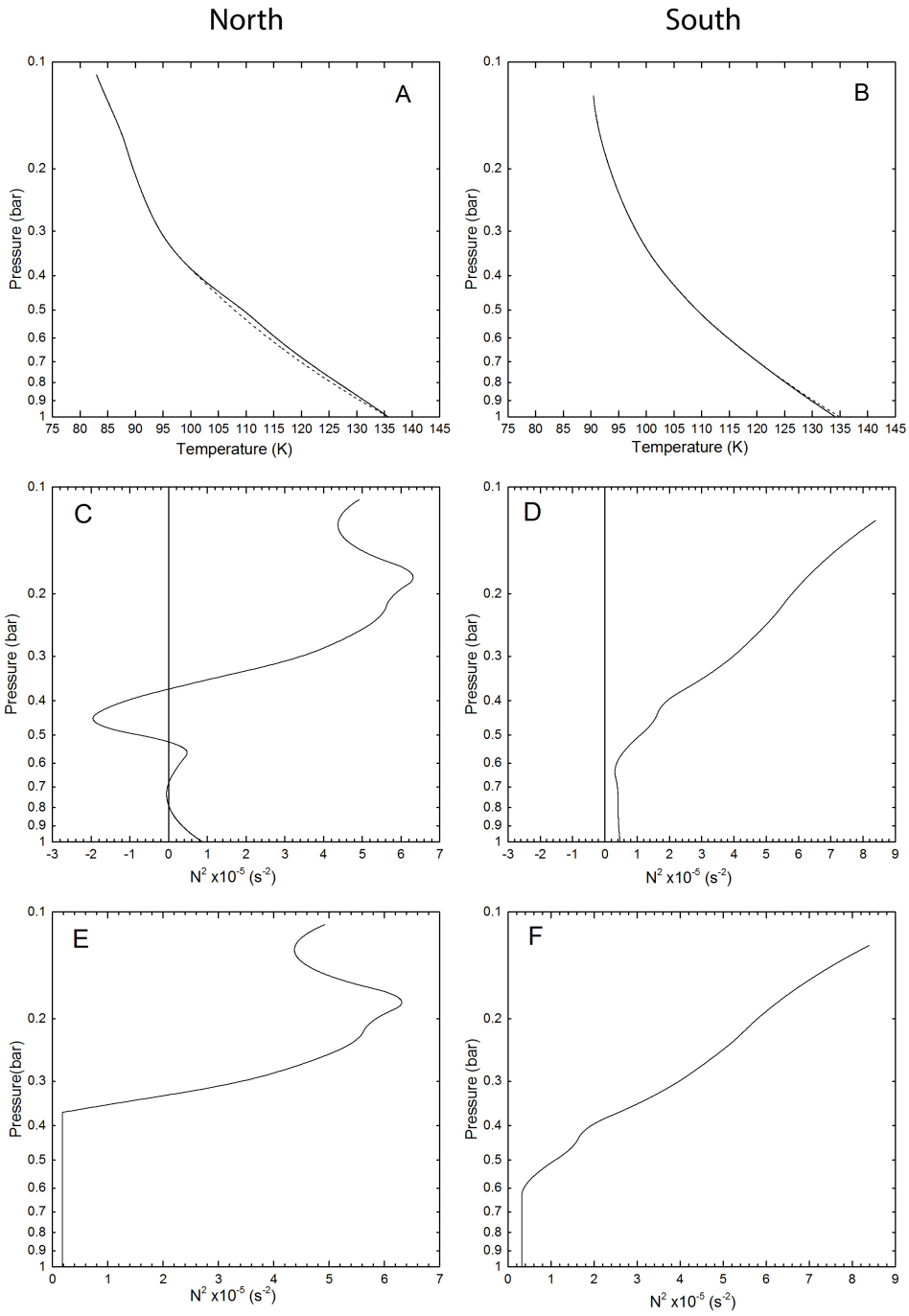

Figure 5.2: Temperature profiles from Fletcher et al. (2015) (solid lines) from June 2013 (A) and December 2008 (B) and derived Brunt-Väisälä frequency profiles for the hexagonal jet (C) and its counterpart in the south (D). Modified Brunt-Väisälä profiles used for the claculations are shown for the Hexagon (E) and the eastward jet at the south (F). The dashed lines in (A) and (B) represent the corresponding temperatures for the used Brunt-Väisälä (E) and (F) profiles. (Figure from Antuñano et al. (2017))

boundaries and the vertical velocity (w) is zero at the top and the bottom (rigid surfaces). From the primary quasi-geostrophic equations, $w = 0$ implies (Godfrey and Moore, 1986)

$$(\bar{u} - c)\frac{\partial \Psi_0'}{\partial z} - \frac{\partial \bar{u}}{\partial z}\Psi_0' = 0. \tag{5.14}$$

The rigid surface at the top and at the bottom of the model is consistent in baroclinic instability models of the Earth's atmosphere, where a solid surface is found at the bottom. However, Gierasch et al. (1979) showed that the analysis of the instability of zonal flows in Jupiter depends strongly in the boundary condition of the lower boundary. They demonstrated that an infinite adiabatic region below the studied region can be approximated using $\Psi_0' = 0$ as the lower boundary. This applies also to Saturn, whose atmosphere is assumed to be adiabatic below ~ 500 mbar pressure level and therefore, we follow Gierasch et al. (1979) and use $\Psi_0' = 0$ boundary condition at the lower boundary of our model. We consider a region of the atmosphere with the top at $p = 100$ mbar (the tropopause) and different depths of the bottom layer.

The Brunt-Väisälä frecuency profile is calculated using the temperature profiles from June 2013 (north) and December 2008 (south) from Fletcher et al. (2015). We use $g = 9.5$ ms^{-2}, z in kilometers relative to $p_0 = 700$ mbar and the normal specific heat, C_p, assuming a meta-stable distribution of hydrogen-helium with no orto-para exchange with a mole-fraction of molecular hydrogen of $X_{orto-H_2} = 0.75$. The computed N^2 profiles are also shown in figure 5.2.

In a baroclinic analysis, the static stability must be positive in the studied domain ($N^2 > 0$) and the Richardson number ($Ri = N^2/(\partial u/\partial z)^2$) must be positive and large (Sánchez-Lavega, 2011) for the baroclinic instability to develop. As can be seen in figure 5.2c, using the retireved temperature profiles from Fletcher et al. (2015), N^2 becomes negative at around 300 mbar at the latitude of hexagonal jet. In order to choose a coherent positive value for the Brunt-Väisälä frequency below that pressure level, we take a nearly adiabatic atmosphere ($N^2 \sim 0$) below ~ 500 mbar. Therefore, we use $N^2 = 0.17 \times 10^{-5}$ s^{-2} for the hexagonal jet below 300 mbar and $N^2 = 0.3 \times 10^{-5}$ s^{-2} for the south below 600 mbar. The modified Brunt-Väisälä profiles used in our calculations are shown in figure 5.2e and 5.2f, respectively.

Taking into account the temperature profile at cloud level (500-700 mbar) we compute the vertical wind-shear from the thermal wind relationship (analogue to equation 3.13)

$$f\frac{\partial u}{\partial z} = -\frac{R^*}{H}\frac{\partial T}{\partial y}. \tag{5.15}$$

The mean vertical wind-shear at cloud level is $\frac{\partial u}{\partial z} = -0.1$ ms^{-1}/km (as obtained

in chapter 3.5.1) and therefore, we write

$$\bar{u}(z) = u_{max} - 0.1z \tag{5.16}$$

where we use the measured peak velocity at cloud level $u_{max} = 104$ ms^{-1} of the hexagonal jet and $u_{max} = 88$ ms^{-1} at the eastward jet at 70.4°S (see chapter 3). Finally, in order to solve this problem with realistic values, we use the values of the horizontal wind field described in chapter 3: $\partial^2 u/\partial^2 y = 0.6 \times 10^{-10}$ m^{-1}s^{-1}, $f = 3.2 \times 10^{-4}$ s^{-1}, $\beta = 2 \times 10^{-12}$ m^{-1}s^{-1} for the hexagonal jet and $\partial^2 u/\partial^2 y = -0.5 \times 10^{-10}$ m^{-1}s^{-1}, $f = -3.1 \times 10^{-4}$ s^{-1}, $\beta = 2 \times 10^{-12}$ m^{-1}s^{-1} for its counterpart in the south at 70.4°S. In addition, we take $k_y = 0$ since the maximum growth in the Eady model occurs when the disturbance does not depend on the meridional wavenumber.

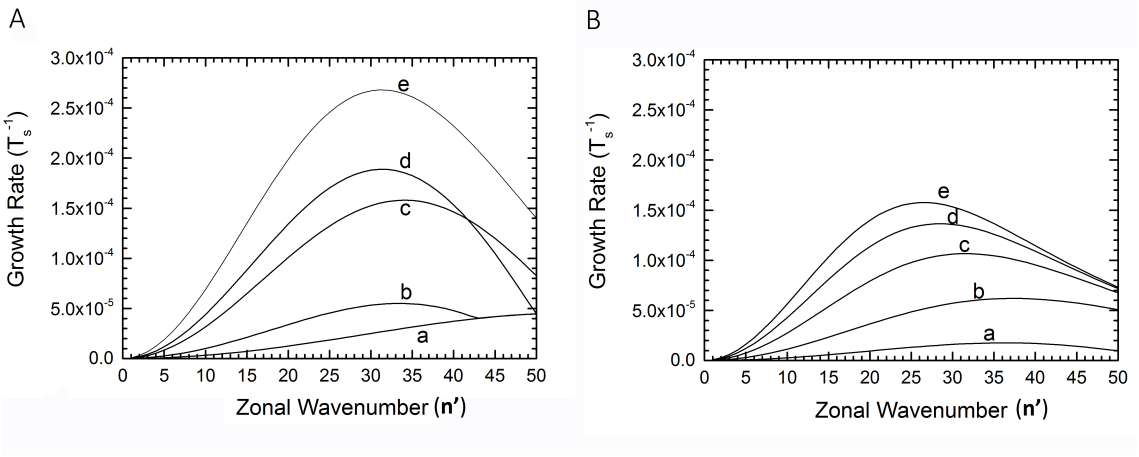

Figure 5.3: Growth-rate curves of the studied baroclinic instability for the hexagonal jet (A) and its counterpart in the south (B). Different curves represent the variation of the growth rate when the bottom layer changes from 1 bar (a) to 5 bar (e). $T_s = \Omega$ in System III. (Figure form Antuñano et al. (2017))

We have computed the growth-rate curves of baroclinic instability for five different values of the bottom layer (from 1 bar to 5 bar). Figure 5.3, shows the obtained growth-rate curves for the hexagonal jet and its counterpart in the south for the five different altitudes (curves a to e). Our results indicate that the most unstable zonal wavenumbers, $n' = 32$ for the Hexagon and $n' = 27$ for the eastward jet in the south, correspond to the model with the deepest bottom layer (at 5 bar) for both eastward jets. Moreover, they show that the growth-rate of the baroclinic instability in the jet at 70.4°S is smaller than that of the Hexagon. The large wave numbers of the fastest growing modes both for the south and north indicate that these results are not consistent with the observations neither at the Hexagon nor at its counterpart in the south.

5.3 Discussion

The origin and nature of the Hexagon is still an open question, as some of the hypotheses that attempt to answer this question remain controversial. In this study, we have analyzed several possible interpretations of the Hexagon's origin from two different points of views: (i) the Hexagon as a Rossby wave and (ii) the possibility that the Hexagon originates from an instability of the jet.

The results of our analyses suggest that:

- The hexagon could be a free Rossby wave vertically trapped in a region of positive static stability ($m^2 < 0$), which does not need to be forced, as suggested by Allison et al. (1990)), by a vortex impinging on the jet.
- The Hexagon could also be a result of a barotropic instability in a Gaussian jet. However, this hypothesis does not explain the absence of a Hexagon in the southern hemisphere.
- The Hexagon does not arise as a baroclinic instability in a first approximation, in which we consider a disturbance of amplitude $\Psi_0'(z)$ periodic in the zonal (x) and meridional (y) directions and in time (t) and assume a vertical velocity profile $u(z)$ deduced from the thermal wind at the peak velocity of the analyzed Gaussian jet. A more general analysis of a baroclinic instability, that considers the zonal velocity profile $u(y, z)$ and a disturbance of amplitude $\Psi_0'(y, z)$ periodic only in the zonal direction (x) and time (t), may give different results, as suggested by the work of Morales-Juberías et al. (2015), since their numerical simulations show that a very particular $u(y, z)$ profile is required in order to obtain a Hexagon. profile is required in order to obtain a Hexagon. Unfortunately, in their work they do not provide essential information about their modeled atmosphere that is needed to reproduce their results.

Finally, we have to mention that our analysis of the growing modes of both barotropic and baroclinic instabilities do not provide information of the latitudinal amplitude of the disturbance, which plays an important role in the manifestation of the disturbance as a Hexagon (see figure 4.2). Furthermore, these models cannot explain the longevity of the Hexagon, which suggests that it may be a "deep-rooted" feature instead of a feature originated from seasonal instabilities.

Chapter 6

Conclusions

This dissertation is focused on the study and characterization of the dynamics of Saturn's polar regions and the Hexagon, focusing on its relationship to the cloud morphology and local dynamics of the observed meteorological features at that regions. For this purpose, we have used Cassini ISS high-resolution images captured at visible wavelengths, from the violet (400 nm) to the near-infrared (1,000 nm), from November 2006, October/December 2008 and June 2013. The observations and database, as well as the methodology used in order to achieve the goals of this thesis are indicated in chapter 2. In chapter 3, we have described the averaged horizontal wind field and relative vorticity, and the zonally averaged Ertel and quasi-geostrophic potential vorticity of both polar regions from $\sim 60°$ to $90°$. A characterization of the different cloud morphologies observed at the north polar region, their local dynamics and temporal variability is presented in chapter 4. Finally, various interpretations of the nature of Hexagon are given in chapter 5.

The main conclusions of this dissertation are detailed below.

Averaged Dynamics of Saturn's Polar Regions

- Averaged horizontal velocity maps of Saturn's north and south polar regions from June 2013 and October/December 2008, respectively, show that the zonal dynamics of these regions are very similar. On the one hand, we can find an intense eastward jet located at the outer region of each polar vortex, reaching velocities of $140 - 150$ ms^{-1}. In addition, a slower and narrow eastward jet is also observed at both polar regions, with a velocity peak of ~ 100 ms^{-1}. Finally, two slow westward jets are also observed at both polar regions, reaching velocities of ~ -10 ms^{-1}. These results are in agreement with previous measurements.

- However, some differences are also present in these maps. The most remarkable one is that the most equatoward jet of the north polar region meanders in latitude forming a hexagonal shape, while its counterpart in the south does not deviate from a purely zonal flow. Therefore, meridional velocity maps show a very different behavior between the north and south polar regions,

where the meandering of the hexagonal jet presents poleward and equatoward meridional velocities of the order of ± 28 ms^{-1}, while at the south polar region non of the jets present meridional velocities as they do not deviate from a zonal flow.

- From the zonal velocity profiles we see that both polar jets are clearly asymmetric, presenting a fast drop on the velocity poleward of 88.5°. Moreover, although both north and south polar jets reach their peak velocity at the same latitude, the southern polar jet is 1.4° wider at the Full Width Half Maximum (FWHM), extending more equatoward, than the north polar jet. On the other hand, the hexagonal jet and the eastward jet at 70.4°S present symmetric zonal mean profiles with a Gaussian shape of $2.38 \pm 0.05°$ and $2.8 \pm 0.1°$ FWHM, respectively. Finally, the jet at 70.4° south is located 5° closer to the equator than the Hexagon.

- Averaged relative vorticity maps, retrieved from the measured horizontal wind fields, show that the relative vorticity is very similar at both polar regions. It is mainly zero away from the eastward jets, due to the weak westward jets present at the polar regions. However, at the hexagonal jet and its counterpart in the south at 70.4°S, it increases and reaches a vorticity peak of $\pm 6 \pm 1 \times 10^{-5}$ s^{-1}, around 1/10th of the Coriolis parameter at those latitudes. Finally, both polar vortices reach strong cyclonic averaged relative vorticity of the order of the Coriolis parameter at the poles. Profiles of meridional gradients of the ambient vorticity ($\partial^2 \bar{u}/\partial^2 y$) show that the Rayleigh-Kuo stability criterion for barotropic atmosphere is clearly violated at the flanks of the Hexagon and its counterpart in the south.

- Zonally averaged extended potential temperature ($\tilde{\tau}$) maps for December 2008 (southern summer) and June 2013 (beginning of northern summer) have been computed using temperature profiles retrived by Fletcher et al. (2015) from CIRS data and considering the normal specific heat with an orto-para fraction $X_{orto-H_2} = 0.75$. The results show a strong variation on the zonally averaged "extended" potential temperature with altitudes above 60 mbar. Furthermore, it is clearly seen that isentropic surfaces almost follow isobaric surfaces. Vertical gradients of the zonally averaged "extended" potential temperature show a stratified and statically stable ($d\tilde{\tau}/dP < 0$) atmosphere between 1 mbar and 500 mbar (the region under study).

- Latitude-pressure normalized Ertel and quasi-geostrophic potential vorticity maps of both polar regions from 63.5° north and south to the pole and for pressures between 500 mbar and 1 mbar have been calculated. These maps show that the Coriolis parameter is dominant at the regions under study, resulting in positive potential vorticities at the north polar region and negative at the south at all pressure levels. Both the normalized Ertel and the quasi-geostrophic potential vorticities range between 2.2×10^{-4} s^{-1} and 4.2×10^{-4} s^{-1} at the north polar region and between -2.2×10^{-4} s^{-1} and -5.5×10^{-4} s^{-1} at the south polar region. Meridional gradients of these two magnitudes present a very similar behavior, showing that at the southern summer (December

2008) and the beginning of the northern spring (June 2013), thermodynamic instability could grow at the flanks of the Hexagon, its counterpart in the south at 70.4° and the flanks of the polar jets.

- Similarities in the dynamics of both polar regions suggest that the presence of the Hexagon in the north and its absence in the south could be related to the latitudinal difference of their latitude location, where the Hexagon is 5° poleward than its counterpart in the south.

Temporal Variability, Dynamics and Characterization of Local Vortices and Compact Cloud Field of the North Polar Region

Local vortices:

- Local vortices are found at different latitudes on Saturn, including the polar regions. Between January 2009 (early northern spring) and November 2014 (beginning of northern summer) two anticyclones and various cyclones are present at the north polar region.

- The largest anticyclone is a long-lived feature of $3,600 \times 2,400$ km size that has been observed from November 2012 to at least November 2014. Measurements of the local velocity of this anticyclones indicate that it moves with the background, presenting a relative vorticity of around ten times the ambient vorticity of the area. Furthermore, tracking of the location of this anticyclone during the studied epoch shows that the anticyclone did not migrate to the pole nor to the equator.

- The second anticyclone, visible in continuum band images, was present over a year with a size of $2,800 \times 2,300$ km near the polar jet at 85.8°N. This vortex did not migrate during the studied epoch either to the pole or to the equator. Measurements of its zonal velocity show that, as the previously mentioned anticyclone, it moves with the background. We were not able to measure vorticity in this case.

- A number of cyclones are observed at around 78°N, right poleward the Hexagon. These cyclones are circular, presenting typical sizes of $1,000 - 1,500$ km. During the studied epoch, between 3 and 5 cyclones are present simultaneously moving with the same velocity as their background and presenting a relative vorticity two times larger than the ambient vorticity of that region. Tracking of these cyclones show that they oscillate around $\pm 0.5°$ in latitude following the meandering of the hexagonal jet with a life-time of at least one month.

Compact Cloud Field:

- Saturn's polar regions, unlike other latitudes, present a large number of bright compact clouds in continuum band images. These clouds, not observed in methane absorption band and violet wavelengths, are relatively deep in the troposphere, as they are clearly visible at $4 - 5$ bar pressure level in images captured at 5 μm by VIMS during the long north polar winter.

- Although they present diverse shapes, most of them show a ring-like shape, similar to the cumulus clouds of closed mesoscale cellular convection (MCC) generated on Earth.

- The number, size and distribution of the compact clouds present between 77°N and 84°N (where they are not elongated due to wind-shear) do not change significantly between the early northern spring (January 2009) and the beginning of the summer (June 2013). At this region there are around 410 and 480 bright clouds of sizes ranging from ~ 10 km to $1,000$ km in January 2009 and June 2013, respectively, distributed nearly uniformly in latitude but not homogeneously in longitude. Their typical longitudinal size is of the order of $200 - 300$ km at both epochs.

- These compact clouds move with the background and as far as our measurements permit, they do not migrate either to the pole or to the equator. Finally, their estimated lifetime is at best cases shorter than $8 - 9$ days.

- The presence of the compact cloud field in the first high-resolution images of the polar regions and during the long northern winter, when Saturn's north pole was not illuminated by the Sun, suggest that the compact cloud field could be originated deep in the troposphere by internal heat.

Cloud Morphology and Temporal Variability of the North Polar Vortex

- A long-lived and stable cyclonic vortex is present at each pole of Saturn. Both vortices are almost circular, expanding from 88.5° north and south to the pole and presenting bright spiraling clouds at their outer edge. Analysis of their appearance at various wavelengths show that they are located at a depressed region of the atmosphere, as they are observed dark in methane absorption band filters and bright in violet.

- Although both polar vortices are long-lived features, the appearance and albedo of the north polar vortex at cloud level varies rapidly between November 2012 and September 2014 (see figure 4.16) reducing 0.2° in latitude in methane absorption band and violet filters. During these epochs, the zonal velocity profile and the relative vorticity of the regions remains unchanged, not being affected by the albedo changes.

- The absence of migration of the studied "puffy" cloud field and regular cyclones and anticyclones does not allow us to confirm or reject that Saturn's polar vortices are not formed from the poleward migration of small cyclones.

Cloud Morphology, Local Dynamics and Interpretation of the Hexagon

- The Hexagon is a long-lived and stable feature that has been present in Saturn's northern polar region for more than 35 years. Although it is observed with the highest contrast at continuum band CB2 filters (752 nm), it is also

seen at visible wavelengths ($400 - 1,000$ nm) and in thermal infrared wavelengths between 14.7 μm and 16.6 μm and at 5 μm, which sense the upper (150 mbar) and the mid troposphere ($4 - 5$ bar), respectively. However, in the thermal infrared at $7.4 - 8$ μm, which sense the upper stratosphere ($1 - 10$ mbar), the Hexagon is no longer noticeable.

- The appearance of the hexagonal jet and its surroundings at different wavelengths show that the region poleward the hexagonal eastward jet is a depressed region in the troposphere, while equatoward the jet, the region is higher in the troposphere. In the case of the hexagonal eastward jet, continuum band images show that it is formed by bright and dark narrow filaments that follow the meandering and seem to be deviated toward its center.

- Measurements of the motion of the vertices of the Hexagon show that they are nearly stationary respect to Saturn's System III rotation rate, moving westward with a mean drift-rate of $< \omega >= 0.0129 \pm 0.0020°$/day between 2008 and 2014.

- The center of the hexagonal jet meanders between 75.3° and 76.3°, following a simple sinusoidal function with zonal wavenumber 6 and 0.5° amplitude.

- Its zonal velocity, computed using a coordinate system adapted to the motion of the eastward jet, shows a velocity peak of 105 ms^{-1} and a Gaussian shape of FWHM of 2.38°. This jet presents a high relative vorticity, around ten times larger than the ambient vorticity and 1/4th of the Coriolis parameter.

- Although the hexagon is a long-lived stable feature, different episodes of transient plume-like activity, probably of convective nature, have been observed trapped at the cloud level inside the hexagonal jet. During these activities, the zonal mean profile remained unchanged and the plume moved, overall, with the background.

- In order to understand the nature of the Hexagon, we have performed different interpretations. Firstly, we have focused on the motions of the vertices of the Hexagon and the longitudinal and meridional size of its sides to demonstrate that it could be a free Rossby wave trapped at a region of positive static stability of unknown vertical extension. Lastly, we have computed the growing modes for the hexagonal jet and its counterpart in the south assuming, on the one hand, an unstable shallow water barotropic jet and on the other hand, a baroclinic jet. Results show that in the case of a shallow water barotropic flow, the maximum growth rate is obtained for a zonal wavenumber 6 for the hexagonal jet and 7 for the eastward jet at 70.4° for a $L_D = 1,000$ km. These results are in agreement with the observations of the hexagonal jet, but not with the observations of the eastward jet in the south. Results of the growing modes of a simple 1D baroclinic flow show that the zonal wavenumber of the maximum growth-rate is of the order of 30 at both jets, not observed at any of the jets.

- Finally, taking into account the longevity of the Hexagon, the temporal stability and its survival to the long northern winter we propose that the Hexagon could be a manifestation of the meanders of a deep unstable jet and we suggest that the motion of its vertices could maybe represent the real rotation rate of the interior of Saturn.

6.1 Future Work

The Cassini spacecraft is obtaining unprecedented high-resolution images of the north polar region of Saturn during its "Gran Finale" mission, which will provide new information of the dynamics of this region at very high-resolution. Therefore, analyzing these images and measuring the horizontal wind field of the north polar region will be our first goal in order to:

- Study the long-term dynamics of Saturn's polar regions.
- Obtain, if possible, (u', v') profiles and momentum injection rates at the polar jets and in particular, at the Hexagon, with the aim of understanding the process of the maintenance of the jets.
- Study the thermal structure of the polar regions and their horizontal wind at simultaneous epochs, in order to analyze seasonal effects on these regions.
- Apply new studies of the gravitational field $g(r, \phi, \lambda)$ to the vertical structure of the jets present at the north and south polar regions.

Furthermore, it would be interesting to use the James Webb Telescope (JWST) and the Hubble Space Telescope (HST) in order to continue analyzing the temporal evolution of the Hexagon and the polar regions in visible and thermal-infrared wavelengths.

The final goal of the study would be to develop a numerical model capable of reproducing the observed dynamics and morphology of the polar regions and the origin of the Hexagon and see how they relate to the general circulation on Saturn by:

- Expanding the study of the growing modes of the baroclinic instability by computing a more general bi-dimensional analysis for diverse values of the unknown parameters of Saturn's atmosphere (under work).
- Developing consistent 3D general circulation models of Saturn.

Publications

This thesis has contributed to the following publications:

Refereed Contributions (ISIS)

1. **Antuñano, A.**, del Río-Gaztelurrutia, T., Sánchez-Lavega, A., Hueso, R. (2014). Horizontal velocity of Saturn's polar regions and Hexagon. *Highlights of Spanish Astrophysics VIII, Proceedings of the XI Scientific Meeting of the Spanish Astronomical Society*, 637 − 642. ISBN 978-84-606-8760-3.

2. **Antuñano, A.**, del Río-Gaztelurrutia, T., Sánchez-Lavega, A., Hueso, R. (2015). Dynamics of Saturn's Polar Regions. *Journal of Geophysical Research (Planets)*, 120(Feb), 155 − 176. DOI: 10.1002/2014JE004709.

3. **Antuñano, A.**, del Río-Gaztelurrutia, T., Sánchez-Lavega, A., Rodríguez-Aseguinolaza, J. (2017). Cloud morphology and dynamics in Saturn's northern polar region. *Under review in Icarus*.

4. **Antuñano, A.**, Read, P.L., Fletcher, L.N., del Río-Gaztelurrutia, T., Sánchez-Lavega, (*in preparation*). Zonally averaged Potential Vorticity of Saturn's Polar Regions.

Additional Publications

<u>Refereed Contributions:</u>

1. Sánchez-Lavega, A., del Río-Gaztelurrutia, T., Hueso, R., Pérez-Hoyos, S., García-Melendo, E., **Antuñano**, A., Mendikoa, I., Rojas, J. F., Lillo, J., Barrado-Navascués, D., Gomez-Forrellad, J. M., Go, C., Peach, D., Barry, T., Milika, D. P., Nicholas, P. and Wesley, A. (2014). Saturn's rotation period revealed by the hexagon long-term motion. *Geophysical Research Letters*, 41, 1425-1431. DOI: 10.1002/2013GL059078

2. Sánchez-Lavega, A., García-Melendo, E., Pérez-Hoyos, S., Hueso, R., Wong, M. H., Simon, A., Sanz-Requena, J. F., **Antuñano, A.**, Barrado-Izagirre, N., Garate-Lopez, I., Rojas, J. F., del Río-Gaztelurrutia, T., Gómez-Forrellad, J.

M., Pater, I., Li, L. and Barry, T. (2016) An enduring rapidly moving storm as a guide to Saturn's Equatorial jet's complex structure. *Nature Communications*, 7, 13262. DOI: 10.1038/ncomms13262.

3. Sanz-Requena, J. F., Pérez-Hoyos, S., Sánchez-Lavega, A., **Antuñano, A.** and Irwin, P. G. J. (2017). Haze and cloud structure of Saturn's north pole and Hexagon from Cassini/ISS imaging. *Under review to Icarus.*

4. del Río-Gaztelurrutia, T., Sánchez-Lavega, A., **Antuñano, A.**, Legarreta, J., Sayanagi, K.M., Hueso, R and Rojas, J.F. (2017). A Planetary-Scale disturbance in long living three vortex system in Saturn's atmosphere. *In preparation.*

Non-Refereed Contributions:

1. Sánchez-Lavega, A., del Río-Gaztelurrutia, T., Hueso, R. and **Antuñano, A.** (2016). Grandes grupos solares en el verano de 2015. *Astronomía*, 36, 200 (Feb.). ISSN:1699-7751.

This thesis has contributed to the following communications:

Meeting Presentations

Oral:

1. **Antuñano, A.**, del Río-Gaztelurrutia, T., Sánchez-Lavega, A., Hueso, R. Perfil de vientos bidimensional en la región polar norte de Saturno y Hexágono. *Reunión Cientfica de la Sociedad Española de Astronomía 2012*, Teruel, Spain. September 2014.

2. **Antuñano, A.**, del Río-Gaztelurrutia, T., Sánchez-Lavega, A., Hueso, R. Dynamics of Saturn's Polar Regions. Program Book, page 130, DPS2014-508.01. *46th Annual Meeting of the Division for Planetary Sciences of the AAS*, Tucson, USA. November 2014.

3. **Antuñano, A.**, del Río-Gaztelurrutia, T., Sánchez-Lavega, A. An analysis of the stability of Saturn's hexagon jet and its counterpart in the south. *IV Reunin sobre Ciencias Planetarias y Exploracin del Sistema Solar (CPESS4)*, Alicante, Spain. July 2015.

4. **Antuñano, A.**, del Río-Gaztelurrutia, T., Sánchez-Lavega, A. An analysis of the stability of Saturn's hexagon jet and its counterpart in the south. Program Book, page 43, EPSC2015-231. *European Planetary Science Congress 2014*, Nantes, France. September 2015.

5. **Antuñano, A.**, del Río-Gaztelurrutia, T., Sánchez-Lavega, A., Rodríguez-Aseguinolaza, J. Dinámica y nubes en las regions polares de Saturno y el Hexágono. *Reunión Cientfica de la Sociedad Española de Astronomía 2012*, Bilbao, Spain. September 2016.

Posters:

1. **Antuñano, A.**,del Río-Gaztelurrutia, T., Sánchez-Lavega, A., Hueso, R. Horizontal velocity in Saturn's northern polar region and hexagon. Program Book, page 23, EPSC2014-291. *European Planetary Science Congress 2014*, Cascais, Portugal. September 2014.

Additional Communications

Oral:

1. Sánchez-Lavega, A., del Río-Gaztelurrutia, T., **Antuñano, A.,** Hueso, R., Pérez-Hoyos, S., Mendikoa, I., Rojas, J. F. and IOPW-PVOL team. The long-term rotation period of Saturn's hexagon. Program Book, page 23, EPSC2013-170. *European Planetary Science Congress 2013*, London, United Kingdom. September 2013

2. Sánchez-Lavega, A., Hueso,R., Pérez-Hoyos, S., **Antuñano, A.**, Rojas, J. F., del Río-Gaztelurrutia, T., Barrado-Izagirre, N., Garate-Lopez, I., García-Melendo, E., Wong, M. H., de Pater, I., Simon, A. A., Gomez-Gorrellad, J. M. and Sanz-Requena, J. F. An enduring rapidly moving storm as a guide to Saturn's equatorial jet complex structure. Program Book, page 111, DPS2015-400.03. *47th Annual Meeting of the Division for Planetary Sciences of the AAS*, National Harbor, USA. November 2015.

3. del Río-Gaztelurrutia, T., Sánchez-Lavega, A., **Antuñano, A.**, Hueso,R., Pérez-Hoyos, S., Rojas, J. F., Wong, M. H., Simon, A. A., Gomez-Gorrellad, J. M. polar disturbance surrounding a long living cyclone in Saturn's atmosphere.*AGU Fall Meeting 2015*, San Francisco, USA. December 2015.

Posters:

1. del Río-Gaztelurrutia, T., Sánchez-Lavega, A., **Antuñano, A.**, Hueso,R., Pérez-Hoyos, S., Rojas, J. F., Wong, M. H., Simon, A. A., Gomez-Gorrellad, J. M. polar disturbance surrounding a long living cyclone in Saturn's atmosphere. Program book, page 98, DPS2015-311.12. *47th Annual Meeting of the Division for Planetary Sciences of the AAS*, National Harbor, USA. November 2015.

2. Sánchez-Lavega, A., Hueso,R., Pérez-Hoyos, S., **Antuñano, A.**, Rojas, J. F., del Río-Gaztelurrutia, T., Barrado-Izagirre, N., Garate-Lopez, I., García-Melendo, E., Wong, M. H., de Pater, I., Simon, A. A., Gomez-Gorrellad, J. M. and Sanz-Requena, J. F. An enduring rapidly moving storm as a guide to Saturn's equatorial jet complex structure. *AGU Fall Meeting 2015*, San Francisco, USA. December 2015.

Bibliography

Acton, C. H. (1996). Ancillary data services of nasa's navigation and ancillary information facility. *Planetary and Space Science*, 44(1):65–70.

Acuña, M. H. and Ness, N. F. (1980). The magnetic field of saturn: Pioneer 11 observations. *Science*, 207(4429):444–446.

Agee, E. M., Chen, T. S., and Dowell, K. E. (1973). A review of mesoscale cellular convection. *Bulletin of the American Meteorological Society*, 54(10):1004–1012.

Allison, M., Godfrey, D. A., and Beebe, R. F. (1990). A wave dynamical interpretation of saturn's polar hexagon. *Science*, 247(4946):1061–1063.

Anderson, J. D. and Schubert, G. (2007). Saturn's gravitational field, internal rotation, and interior structure. *Science*, 317(5843):1384–1387.

Antuñano, A., del Río-Gaztelurrutia, T., Sánchez-Lavega, A., and Hueso, R. (2015). Dynamics of saturn's polar regions. *Journal of Geophysical Research: Planets*, 120(2):155–176.

Antuñano, A., del Río-Gaztelurrutia, T., Sánchez-Lavega, A., and Rodríguez-Aseguinolaza, J. (2017). Cloud morphology and dynamics in saturn's northern polar region. (Under review in Icarus).

Archinal, B. A., A'Hearn, M. F., Bowell, E., Conrad, A., Consolmagno, G. J., Courtin, R., Fukushima, T., Hestroffer, D., Hilton, J. L., Krasinsky, G. A., Neumann, G., Oberst, J., Seidelmann, P. K., Stooke, P., Tholen, D. J., Thomas, P. C., and Williams, I. P. (2011). Report of the IAU working group on cartographic coordinates and rotational elements: 2009. *Celestial Mechanics and Dynamical Astronomy*, 109(2):101–135.

Atreya, S. K. and Wong, A.-S. (2005). Coupled clouds and chemistry of the giant planets- a case for multiprobes. *Space Science Reviews*, 116(1-2):121–136.

Baines, K. H., Momary, T. W., Fletcher, L. N., Showman, A. P., Roos-Serote, M., Brown, R. H., Buratti, B. J., Clark, R. N., and Nicholson, P. D. (2009). Saturn's north polar cyclone and hexagon at depth revealed by cassini/VIMS. *Planetary and Space Science*, 57(14-15):1671–1681.

Barbosa-Aguiar, A. C., Read, P. L., Wordsworth, R. D., Salter, T., and Yamazaki, Y. H. (2010). A laboratory model of saturn's north polar hexagon. *Icarus*, 206(2):755–763.

Barnet, C., Westphal, J., Beebe, R., and Huber, L. (1992). Hubble space telescope observations of the 1990 equatorial disturbance on saturn: Zonal winds and central meridian albedos. *Icarus*, 100(2):499–511.

Barrado-Izagirre, N., Sánchez-Lavega, A., Pérez-Hoyos, S., and Hueso, R. (2008). Jupiter's polar clouds and waves from cassini and hst images: 1993-2006. *Icarus*, 194(1):173–185.

Broadfoot, A. L., Sandel, B. R., Shemansky, D. E., Holberg, J. B., Smith, G. R., Strobel, D. F., McConell, J. C., Kumar, S., Hunten, D. M., Atreya, S. K., Donahue, T. M., Moos, H. W., Bertaux, J. L., Blamont, J. E., Pomphrey, R. B., and Linick, S. (1981). Extreme ultraviolet observations from voyager 1 encounter with saturn. *Science*, 212(4491):206–211.

Brown, R. H., Baines, K. H., Bellucci, G., Bibring, J.-P., Buratti, B. J., Capaccioni, F., Cerroni, P., Clark, R. N., Coradini, A., Cruikshank, D. P., Drossart, P., Formisano, V., Jaumann, R., Langevin, Y., Matson, D. L., Mccord, T. B., Mennella, V., Miller, E., Nelson, R. M., Nicholson, P. D., Sicardy, B., and Sotin, C. (2004). The cassini visual and infrared mapping spectrometer (vims) investigation. In *The Cassini-Huygens Mission*, pages 111–168. Springer Nature.

Caldwell, J., Turgeon, B., Hua, X.-M., Barnet, C. D., and Westphal, J. A. (1993). The drift of saturn's north polar spot observed by the hubble space telescope. *Science*, 260(5106):326–329.

Charney, J. G. and Stern, M. E. (1962). On the stability of internal baroclinic jets in a rotating atmosphere. *Journal of the Atmospheric Sciences*, 19(2):159–172.

Choi, D. S., Showman, A. P., and Brown, R. H. (2009). Cloud features and zonal wind measurements of saturn's atmosphere as observed by cassini/VIMS. *Journal of Geophysical Research*, 114(E4).

Conrath, B. and Gautier, D. (2000). Saturn helium abundance: A reanalysis of voyager measurements. *Icarus*, 144(1):124–134.

Conrath, B. J., Gautier, D., Hanel, R. A., and Hornstein, J. S. (1984). The helium abundance of saturn from voyager measurements. *The Astrophysical Journal*, 282:807.

Conrath, B. J. and Gierasch, P. J. (1984). Global variation of the para hydrogen fraction in jupiter's atmosphere and implications for dynamics on the outer planets. *Icarus*, 57(2):184–204.

Conrath, B. J., Gierasch, P. J., and Nath, N. (1981). Stability of zonal flows on jupiter. *Icarus*, 48(2):256–282.

Davies, M. E., Abalakin, V. K., Bursa, M., Lieske, J. H., Morando, B., Morrison, D., Seidelmann, P. K., Sinclair, A. T., Yallop, B., and Tjuflin, Y. S. (1995). Report of the IAU/IAG/COSPAR working group on cartographic coordinates and rotational elements of the planets and satellites: 1994. *Celestial Mechanics & Dynamical Astronomy*, 63(2):127–148.

del Genio, A., Barbara, J., Ferrier, J., Ingersoll, A., West, R., Vasavada, A., Spitale, J., and Porco, C. (2007). Saturn eddy momentum fluxes and convection: First estimates from cassini images. *Icarus*, 189(2):479–492.

del Genio, A. D., Achterberg, R. K., Baines, K. H., Flasar, F. M., Read, P. L., Sánchez-Lavega, A., and Showman, A. P. (2009). Saturn atmospheric structure and dynamics. In *Saturn from Cassini-Huygens*, pages 113–159. Springer Nature.

del Genio, A. D. and Barbara, J. M. (2012). Constraints on saturn's tropospheric general circulation from cassini ISS images. *Icarus*, 219(2):689–700.

del Genio, A. D. and Barbara, J. M. (2016). An objective classification of saturn cloud features from cassini ISS images. *Icarus*, 271:222–236.

del Río-Gaztelurrutia, T., Legarreta, J., Hueso, R., Pérez-Hoyos, S., and Sánchez-Lavega, A. (2010). A long-lived cyclone in saturn's atmosphere: Observations and models. *Icarus*, 209(2):665–681.

Desch, M. D. and Kaiser, M. L. (1981). Voyager measurement of the rotation period of saturn's magnetic field. *Geophysical Research Letters*, 8(3):253–256.

Dougherty, M. K., Kellock, S., Southwood, D. J., Balogh, A., Smith, E. J., Tsurutani, B. T., Gerlach, B., Glassmeier, K.-H., Gleim, F., Russell, C. T., Erdos, G., Neubauer, F. M., and Cowley, S. W. H. (2004). The cassini magnetic field investigation. In *The Cassini-Huygens Mission*, pages 331–383. Springer Nature.

Dowling, T., Fischer, A., Gierasch, P., Harrington, J., LeBeau, R., and Santori, C. (1998). The explicit planetary isentropic-coordinate (EPIC) atmospheric model. *Icarus*, 132(2):221–238.

Dyudina, U., IngersollL, A., Ewald, S., Porco, C., Fischer, G., Kurth, W., Desch, M., Genio, A. D., Barbara, J., and Ferrier, J. (2007). Lightning storms on saturn observed by cassini ISS and RPWS during 2004–2006. *Icarus*, 190(2):545–555.

Dyudina, U. A., Ingersoll, A. P., Ewald, S. P., Porco, C. C., Fischer, G., and Yair, Y. (2013). Saturn's visible lightning, its radio emissions, and the structure of the 2009-2011 lightning storms. *Icarus*, 226(1):1020–1037.

Dyudina, U. A., Ingersoll, A. P., Ewald, S. P., Vasavada, A. R., West, R. A., Genio, A. D. D., Barbara, J. M., Porco, C. C., Achterberg, R. K., Flasar, F. M., Simon-Miller, A. A., and Fletcher, L. N. (2008). Dynamics of saturn's south polar vortex. *Science*, 319(5871):1801–1801.

Eady, E. T. (1949). Long waves and cyclone waves. *Tellus*, 1(3):33–52.

Edgington, S. G. and Spilker, L. J. (2016). Cassini's grand finale. *Nature Geoscience*, 9(7):472–473.

Elachi, C., Allison, M. D., Borgarelli, L., Encrenaz, P., Im, E., Janssen, M. A., Johnson, W. T. K., Kirk, R. L., Lorenz, R. D., Lunine, J. I., Muhleman, D. O., Ostro, S. J., Picardi, G., Posa, F., Rapley, C. G., Roth, L. E., Seu, R., Soderblom,

L. A., Vetrella, S., Wall, S. D., Wood, C. A., and Zebker, H. A. (2004). Radar: The cassini titan radar mapper. *Space Science Reviews*, 115(1-4):71–110.

Epele, L. N., Fanchiotti, H., Canal, C. A. G., Pacheco, A. F., and Sañudo, J. (2007). Venus atmosphere profile from a maximum entropy principle. *Nonlinear Processes in Geophysics*, 14(5):641–647.

Esposito, L. W., Barth, C. A., Colwell, J. E., Lawrence, G. M., McClintock, W. E., Stewart, A. I. F., Keller, H. U., Korth, A., Lauche, H., Festou, M. C., Lane, A. L., Hansen, C. J., Maki, J. N., West, R. A., Jahn, H., Reulke, R., Warlich, K., Shemansky, D. E., and Yung, Y. L. (2004). The cassini ultraviolet imaging spectrograph investigation. *Space Science Reviews*, 115(1-4):299–361.

Fischer, G., Kurth, W. S., Gurnett, D. A., Zarka, P., Dyudina, U. A., Ingersoll, A. P., Ewald, S. P., Porco, C. C., Wesley, A., Go, C., and Delcroix, M. (2011). A giant thunderstorm on saturn. *Nature*, 475(7354):75–77.

Flasar, F. M., Kunde, V. G., Abbas, M. M., Achterberg, R. K., Ade, P., Barucci, A., B'ezard, B., Bjoraker, G. L., Brasunas, J. C., Calcutt, S., Carlson, R., C'esarsky, C. J., Conrath, B. J., Coradini, A., Courtin, R., Coustenis, A., Edberg, S., Edgington, S., Ferrari, C., Fouchet, T., Gautier, D., Gierasch, P. J., Grossman, K., Irwin, P., Jennings, D. E., Lellouch, E., Mamoutkine, A. A., Marten, A., Meyer, J. P., Nixon, C. A., Orton, G. S., Owen, T. C., Pearl, J. C., Prang'e, R., Raulin, F., Read, P. L., Romani, P. N., Samuelson, R. E., Segura, M. E., SHOWALTER, M. R., Simon-Miller, A. A., Smith, M. D., Spencer, J. R., Spilker, L. J., and Taylor, F. W. (2004). Exploring the saturn system in the thermal infrared: The composite infrared spectrometer. *Space Science Reviews*, 115(1-4):169–297.

Fletcher, L., Irwin, P., Teanby, N., Orton, G., Parrish, P., Dekok, R., Howett, C., Calcutt, S., Bowles, N., and Taylor, F. (2007). Characterising saturn's vertical temperature structure from cassini/CIRS. *Icarus*, 189(2):457–478.

Fletcher, L. N., Hesman, B., Achterberg, R., Irwin, P., Bjoraker, G., Gorius, N., Hurley, J., Sinclair, J., Orton, G., Legarreta, J., García-Melendo, E., Sánchez-Lavega, A., Read, P., Simon-Miller, A., and Flasar, F. (2012). The origin and evolution of saturn's 2011-2012 stratospheric vortex. *Icarus*, 221(2):560–586.

Fletcher, L. N., Hesman, B. E., Irwin, P. G. J., Baines, K. H., Momary, T. W., Sánchez-Lavega, A., Flasar, F. M., Read, P. L., Orton, G. S., Simon-Miller, A., Hueso, R., Bjoraker, G. L., Mamoutkine, A., del Rio-Gaztelurrutia, T., Gomez, J. M., Buratti, B., Clark, R. N., Nicholson, P. D., and Sotin, C. (2011). Thermal structure and dynamics of saturn's northern springtime disturbance. *Science*, 332(6036):1413–1417.

Fletcher, L. N., Irwin, P., Achterberg, R., Orton, G., and Flasar, F. (2016). Seasonal variability of saturn's tropospheric temperatures, winds and para-h 2 from cassini far-IR spectroscopy. *Icarus*, 264:137–159.

Fletcher, L. N., Irwin, P., Sinclair, J., Orton, G., Giles, R., Hurley, J., Gorius, N., Achterberg, R., Hesman, B., and Bjoraker, G. (2015). Seasonal evolution of saturn's polar temperatures and composition. *Icarus*, 250:131–153.

Fletcher, L. N., Irwin, P. G. J., Orton, G. S., Teanby, N. A., Achterberg, R. K., Bjoraker, G. L., Read, P. L., Simon-Miller, A. A., Howett, C., de Kok, R., Bowles, N., Calcutt, S. B., Hesman, B., and Flasar, F. M. (2008). Temperature and composition of saturn's polar hot spots and hexagon. *Science*, 319(5859):79–81.

Fouchet, T., Moses, J. I., and Conrath, B. J. (2009). Saturn: Composition and chemistry. In *Saturn from Cassini-Huygens*, pages 83–112. Springer Nature.

Galopeau, P. H. M. and Lecacheux, A. (2000). Variations of saturn's radio rotation period measured at kilometer wavelengths. *Journal of Geophysical Research: Space Physics*, 105(A6):13089–13101.

Garate-Lopez, I., Hueso, R., Sánchez-Lavega, A., Peralta, J., Piccioni, G., and Drossart, P. (2013). A chaotic long-lived vortex at the southern pole of venus. *Nature Geoscience*, 6(4):254–257.

García-Melendo, E., Hueso, R., Sánchez-Lavega, A., Legarreta, J., del Río-Gaztelurrutia, T., Pérez-Hoyos, S., and Sanz-Requena, J. F. (2013). Atmospheric dynamics of saturn's 2010 giant storm. *Nature Geoscience*, 6(7):525–529.

García-Melendo, E., Pérez-Hoyos, S., Sánchez-Lavega, A., and Hueso, R. (2011). Saturn's zonal wind profile in 2004-2009 from cassini ISS images and its long-term variability. *Icarus*, 215(1):62–74.

García-Melendo, E., Sánchez-Lavega, A., Legarreta, J., Perez-Hoyos, S., and Hueso, R. (2010). A strong high altitude narrow jet detected at saturn's equator. *Geophysical Research Letters*, 37(22):n/a–n/a.

García-Melendo, E., Sánchez-Lavega, A., Rojas, J., Pérez-Hoyos, S., and Hueso, R. (2009). Vertical shears in saturn's eastward jets at cloud level. *Icarus*, 201(2):818–820.

Gierasch, P. J., Conrath, B. J., and Read, P. L. (2004). Nonconservation of ertel potential vorticity in hydrogen atmospheres. *Journal of the Atmospheric Sciences*, 61(15):1953–1965.

Gierasch, P. J., Ingersoll, A. P., and Pollard, D. (1979). Baroclinic instabilities in jupiter's zonal flow. *Icarus*, 40(2):205–212.

Godfrey, D. (1988). A hexagonal feature around saturn's north pole. *Icarus*, 76(2):335–356.

Godfrey, D. and Moore, V. (1986). The saturnian ribbon feature- a baroclinically unstable model. *Icarus*, 68(2):313–343.

Gurnett, D. A. (2005). Radio and plasma wave observations at saturn from cassini's approach and first orbit. *Science*, 307(5713):1255–1259.

Gurnett, D. A., Kurth, W. S., Kirchner, D. L., Hospodarsky, G. B., Averkamp, T. F., Zarka, P., Lecacheux, A., Manning, R., Roux, A., Canu, P., Cornilleau-Wehrlin, N., Galopeau, P., Meyer, A., Bostrm, R., Gustafsson, G., Wahlund, J.-E., Åhlen, L., Rucker, H. O., Ladreiter, H. P., Macher, W., Woolliscroft, L. J. C., Alleyne, H., Kaiser, M. L., Desch, M. D., Farrell, W. M., Harvey, C. C., Louarn, P., Kellogg, P. J., Goetz, K., and Pedersen, A. (2004). The cassini radio and plasma wave investigation. *Space Science Reviews*, 114(1-4):395–463.

Gurnett, D. A., Lecacheux, A., Kurth, W. S., Persoon, A. M., Groene, J. B., Lamy, L., Zarka, P., and Carbary, J. F. (2009). Discovery of a north-south asymmetry in saturn's radio rotation period. *Geophysical Research Letters*, 36(16).

Hanel, R., Conrath, B., Flasar, F. M., Kunde, V., Maguire, W., Pearl, J., Pirraglia, J., Samuelson, R., Cruikshank, D., Gautier, D., Gierasch, P., Horn, L., and Ponnamperuma, C. (1982). Infrared observations of the saturnian system from voyager 2. *Science*, 215(4532):544–548.

Hanel, R., Conrath, B., Flasar, F. M., Kunde, V., Maguire, W., Pearl, J., Pirraglia, J., Samuelson, R., Herath, L., Allison, M., Cruikshank, D., Gautier, D., Gierasch, P., Horn, L., Koppany, R., and Ponnamperuma, C. (1981). Infrared observations of the saturnian system from voyager 1. *Science*, 212(4491):192–200.

Hoskins, B. J., McIntyre, M. E., and Robertson, A. W. (1985). On the use and significance of isentropic potential vorticity maps. *Quarterly Journal of the Royal Meteorological Society*, 111(470):877–946.

Hueso, R., Legarreta, J., García-Melendo, E., Sánchez-Lavega, A., and Pérez-Hoyos, S. (2009). The jovian anticyclone BAII. circulation and interaction with the zonal jets. *Icarus*, 203(2):499–515.

Hueso, R., Legarreta, J., Pérez-Hoyos, S., Rojas, J., Sánchez-Lavega, A., and Morgado, A. (2010a). The international outer planets watch atmospheres node database of giant-planet images. *Planetary and Space Science*, 58(10):1152–1159.

Hueso, R., Legarreta, J., Rojas, J., Peralta, J., Pérez-Hoyos, S., del Río-Gaztelurrutia, T., and Sánchez-Lavega, A. (2010b). The planetary laboratory for image analysis (PLIA). *Advances in Space Research*, 46(9):1120–1138.

Hunt, G. E. and Moore, P. (1982). *Saturn (Rand McNally Library of Astronomical Atlases for Amateur and)*. Rand McNally & Company.

Ingersoll, A. P., Beebe, R. F., Conrath, B. J., and Hunt, G. E. (1984). Structure and dynamics of saturn's atmosphere. In *Saturn (Space Science Series)*, chapter Structure and dynamics of Saturn's atmosphere, pages 195–238. University of Arizona Press.

Ingersoll, A. P., Dowling, T. E., Gierasch, P. J., Orton, G. S., Read, P. L., Sánchez-Lavega, A., Showman, A. P., Simon-Miller, A. A., and Vasavada, A. R. (2004). Dynamics of jupiter's atmosphere. In *Jupiter: The Planet, Satellites and Magnetosphere*. CAMBRIDGE UNIV PR.

Kliore, A. J., Anderson, J. D., Armstrong, J. W., Asmar, S. W., Hamilton, C. L., Rappaport, N. J., Wahlquist, H. D., Ambrosini, R., Flasar, F. M., French, R. G., Iess, L., Marouf, E. A., and Nagy, A. F. (2004). Cassini radio science. *Space Science Reviews*, 115(1-4):1–70.

Kliore, A. J., Lindal, G. F., Patel, I. R., Sweetam, D. N., Hotz, H. B., and MC-Donough, T. R. (1980a). Vertical structure of the ionosphere and upper neutral atmosphere of saturn from the pioneer radio occultation. *Science*, 207(4429):446–449.

Kliore, A. J., Patel, I. R., Lindal, G. F., Sweetnam, D. N., Hotz, H. B., Waite, J. H., and McDonough, T. R. (1980b). Structure of the ionosphere and atmosphere of saturn from pioneer 11 saturn radio occultation. In *1980, Pioneer Saturn*, pages 5857–5870. Wiley-Blackwell.

Kossin, J. P. and Schubert, W. H. (2001). Mesovortices, polygonal flow patterns, and rapid pressure falls in hurricane-like vortices. *Journal of the Atmospheric Sciences*, 58(15):2196–2209.

Krimigis, S. M., Mitchell, D. G., Hamilton, D. C., Livi, S., Dandouras, J., Jaskulek, S., Armstrong, T. P., Boldt, J. D., Cheng, A. F., Gloeckler, G., Hayes, J. R., Hsieh, K. C., Ip, W.-H., Keath, E. P., Kirsch, E., Krupp, N., Lanzerotti, L. J., Lundgren, R., Mauk, B. H., McEntire, R. W., Roelof, E. C., Schlemm, C. E., Tossman, B. E., Wilken, B., and Williams, D. J. (2004). Magnetosphere imaging instrument (MIMI) on the cassini mission to saturn/titan. *Space Science Reviews*, 114(1-4):233–329.

Kurth, W. S., Averkamp, T. F., Gurnett, D. A., Groene, J. B., and Lecacheux, A. (2008). An update to a saturnian longitude system based on kilometric radio emissions. *Journal of Geophysical Research: Space Physics*, 113(A5):n/a–n/a.

Kurth, W. S., Lecacheux, A., Averkamp, T. F., Groene, J. B., and Gurnett, D. A. (2007). A saturnian longitude system based on a variable kilometric radiation period. *Geophysical Research Letters*, 34(2).

Luz, D., Berry, D. L., Piccioni, G., Drossart, P., Politi, R., Wilson, C. F., Erard, S., and Nuccilli, F. (2011). Venus's southern polar vortex reveals precessing circulation. *Science*, 332(6029):577–580.

Mitchell, D. M., Montabone, L., Thomson, S., and Read, P. L. (2014). Polar vortices on earth and mars: A comparative study of the climatology and variability from reanalyses. *Quarterly Journal of the Royal Meteorological Society*, 141(687):550–562.

Morales-Juberías, R., Sayanagi, K. M., Dowling, T. E., and Ingersoll, A. P. (2011). Emergence of polar-jet polygons from jet instabilities in a Saturn model. *Icarus*, 211(2):1284–1293.

Morales-Juberías, R., Sayanagi, K. M., Simon, A. A., Fletcher, L. N., and Cosentino, R. G. (2015). Meandering Shallow Atmospheric Jet as a Model of Saturn's North-Polar Hexagon. *Astrophysical Journal Letters*, 806(1):L18.

Northrop, T. G., Opp, A. G., and Wolfe, J. H. (1980). Pioneer 11 saturn encounter. *Journal of Geophysical Research*, 85(A11):5651.

O'Neill, M. E., Emanuel, K. A., and Flierl, G. R. (2015). Polar vortex formation in giant-planet atmospheres due to moist convection. *Nature Geoscience*, 8(7):523–526.

Orton, G. S. and Yanamandra-Fisher, P. A. (2005). Saturn's temperature field from high-resolution middle-infrared imaging. *Science*, 307(5710):696–698.

Pedlosky, J. (1987). *Geophysical Fluid Dynamics*. Springer.

Pérez-Hoyos, S., Sánchez-Lavega, A., French, R., and Rojas, J. F. (2005). Saturn's cloud structure and temporal evolution from ten years of hubble space telescope images (1994-2003). *Icarus*, 176(1):155–174.

Piccioni, G., Drossart, P., Sanchez-Lavega, A., Hueso, R., Taylor, F. W., Wilson, C. F., Grassi, D., Zasova, L., Moriconi, M., Adriani, A., Lebonnois, S., Coradini, A., Bézard, B., Angrilli, F., Arnold, G., Baines, K. H., Bellucci, G., Benkhoff, J., Bibring, J. P., Blanco, A., Blecka, M. I., Carlson, R. W., Lellis, A. D., Encrenaz, T., Erard, S., Fonti, S., Formisano, V., Fouchet, T., Garcia, R., Haus, R., Helbert, J., Ignatiev, N. I., Irwin, P. G. J., Langevin, Y., Lopez-Valverde, M. A., Luz, D., Marinangeli, L., Orofino, V., Rodin, A. V., Roos-Serote, M. C., Saggin, B., Stam, D. M., Titov, D., Visconti, G., Zambelli, M., Ammannito, E., Barbis, A., Berlin, R., Bettanini, C., Boccaccini, A., Bonnello, G., Bouye, M., Capaccioni, F., Moinelo, A. C., Carraro, F., Cherubini, G., Cosi, M., Dami, M., Nino, M. D., Vento, D. D., Giampietro, M. D., Donati, A., Dupuis, O., Espinasse, S., Fabbri, A., Fave, A., Veltroni, I. F., Filacchione, G., Garceran, K., Ghomchi, Y., Giustini, M., Gondet, B., Hello, Y., Henry, F., Hofer, S., Huntzinger, G., Kachlicki, J., Knoll, R., Driss, K., Mazzoni, A., Melchiorri, R., Mondello, G., Monti, F., Neumann, C., Nuccilli, F., Parisot, J., Pasqui, C., Perferi, S., Peter, G., Piacentino, A., Pompei, C., Reess, J.-M., Rivet, J.-P., Romano, A., Russ, N., Santoni, M., Scarpelli, A., Semery, A., Soufflot, A., Stefanovitch, D., Suetta, E., Tarchi, F., Tonetti, N., Tosi, F., and Ulmer, B. (2007). South-polar features on venus similar to those near the north pole. *Nature*, 450(7170):637–640.

Porco, C. C., Baker, E., Barbara, J., Beurle, K., Brahic, A., Burns, J. A., Charnoz, S., Cooper, N., Dawson, D. D., Genio, A. D. D., Denk, T., Dones, L., Dyudina, U., Evans, M. W., Giese, B., Grazier, K., Helfenstein, P., Ingersoll, A. P., Jacobson, R. A., Johnson, T. V., McEwen, A., Murray, C. D., Neukum, G., Owen, W. M., Perry, J., Roatsch, T., Spitale, J., Squyres, S., Thomas, P., Tiscareno, M., Turtle, E., Vasavada, A. R., Veverka, J., Wagner, R., and West, R. (2005). Cassini imaging science: Initial results on saturn's atmosphere. *Science*, 307(5713):1243–1247.

Porco, C. C., West, R. A., Squyres, S., McEwen, A., Thomas, P., Murray, C. D., Delgenio, A., Ingersoll, A. P., Johnson, T. V., Neukum, G., Veverka, J., Dones, L., Brahic, A., Burns, J. A., Haemmerle, V., Knowles, B., Dawson, D., Roatsch, T., Beurle, K., and Owen, W. (2004). Cassini imaging science: Instrument characteristics and anticipated scientific investigations at saturn. *Space Sci. Rev.*, pages 363–497.

Read, P., Conrath, B., Fletcher, L., Gierasch, P., Simon-Miller, A., and Zuchowski, L. (2009a). Mapping potential vorticity dynamics on saturn: Zonal mean circulation from cassini and voyager data. *Planetary and Space Science*, 57(14-15):1682–1698.

Read, P. L., Dowling, T. E., and Schubert, G. (2009b). Saturn's rotation period from its atmospheric planetary-wave configuration. *Nature*, 460(7255):608–610.

Rogers, J. H. (1995). *The Giant Planet Jupiter (Practical Astronomy Handbooks)*. Cambridge University Press.

Sánchez-Lavega, A. (1994). Saturn's great white spots. *Chaos*, 4(2):341–353.

Sánchez-Lavega, A. (2002a). No hexagonal wave around saturn's southern pole. *Icarus*, 160(1):216–219.

Sánchez-Lavega, A. (2002b). Observations of saturn's ribbon wave 14 years after its discovery. *Icarus*, 158(1):272–275.

Sánchez-Lavega, A. (2011). *An Introduction to Planetary Atmospheres*. Taylor & Francis, CRC Press.

Sánchez-Lavega, A., del Río-Gaztelurrutia, T., Delcroix, M., Legarreta, J. J., Gómez-Forrellad, J. M., Hueso, R., García-Melendo, E., Pérez-Hoyos, S., Barrado-Navascués, D., and Lillo, J. (2012). Ground-based observations of the long-term evolution and death of saturn's 2010 great white spot. *Icarus*, 220(2):561–576.

Sánchez-Lavega, A., del Río-Gaztelurrutia, T., Hueso, R., Gómez-Forrellad, J. M., Sanz-Requena, J. F., Legarreta, J., García-Melendo, E., Colas, F., Lecacheux, J., Fletcher, L. N., Barrado-Navascués, D., Parker, D., Akutsu, T., Barry, T., Beltran, J., Buda, S., Combs, B., Carvalho, F., Casquinha, P., Delcroix, M., Ghomizadeh, S., Go, C., Hotershall, J., Ikemura, T., Jolly, G., Kazemoto, A., Kumamori, T., Lecompte, M., Maxson, P., Melillo, F. J., Milika, D. P., Morales, E., Peach, D., Phillips, J., Poupeau, J. J., Sussenbach, J., Walker, G., Walker, S., Tranter, T., Wesley, A., Wilson, T., and Yunoki, K. (2011). Deep winds beneath saturn's upper clouds from a seasonal long-lived planetary-scale storm. *Nature*, 475(7354):71–74.

Sánchez-Lavega, A., del Río-Gaztelurrutia, T., Hueso, R., Pérez-Hoyos, S., García-Melendo, E., Antuñano, A., Mendikoa, I., Rojas, J. F., Lillo, J., Barrado-Navascués, D., Gomez-Forrellad, J. M., Go, C., Peach, D., Barry, T., Milika,

D. P., Nicholas, P., and Wesley, A. (2014). The long-term steady motion of saturn's hexagon and the stability of its enclosed jet stream under seasonal changes. *Geophysical Research Letters*, 41(5):1425–1431.

Sánchez-Lavega, A., Fischer, G., Fletcher, L. N., García-Melendo, E., Hesman, B., Pérez-Hoyos, S., Sayanagi, K. M., and Sromovsky, L. A. (2016a). The great saturn storm of 2010-2011. In *Saturn in the 21st Century*, chapter 13.

Sánchez-Lavega, A., García-Melendo, E., Pérez-Hoyos, S., Hueso, R., Wong, M. H., Simon, A., Sanz-Requena, J. F., Antuñano, A., Barrado-Izagirre, N., Garate-Lopez, I., Rojas, J. F., del Río-Gaztelurrutia, T., Gómez-Forrellad, J. M., de Pater, I., Li, L., and Barry, T. (2016b). An enduring rapidly moving storm as a guide to saturn's equatorial jet's complex structure. *Nature Communications*, 7:13262.

Sánchez-Lavega, A., Hueso, R., and Acarreta, J. R. (1998). A system of circumpolar waves in jupiter's stratosphere. *Geophysical Research Letters*, 25(21):4043–4046.

Sánchez-Lavega, A., Hueso, R., and Pérez-Hoyos, S. (2007). The three-dimensional structure of saturn's equatorial jet at cloud level. *Icarus*, 187(2):510–519.

Sánchez-Lavega, A., Hueso, R., Pérez-Hoyos, S., and Rojas, J. F. (2006). A strong vortex in saturn's south pole. *Icarus*, 184(2):524–531.

Sánchez-Lavega, A., Lecacheux, J., Colas, F., and Laques, P. (1993). Ground-based observations of saturn's north polar spot and hexagon. *Science*, 260(5106):329–332.

Sánchez-Lavega, A., Lecacheux, J., Colas, F., and Laques, P. (1993). Temporal behavior of cloud morphologies and motions in saturn's atmosphere. *Journal of Geophysical Research*, 98(E10):18857.

Sánchez-Lavega, A., Lecacheux, J., Gomez, J. M., Colas, F., Laques, P., Noll, K., Gilmore, D., Miyazaki, I., and Parker, D. (1996). Large-scale storms in saturn's atmosphere during 1994. *Science*, 271(5249):631–634.

Sánchez-Lavega, A., Orton, G. S., Morales, R., Lecacheux, J., Colas, F., Fisher, B., Fukumura-Sawada, P., Golischf, W., Griepf, D., Kaminski, C., Baines, K., Rages, K., and West, R. (2001). The merger of two giant anticyclones in the atmosphere of jupiter. *Icarus*, 149(2):491–495.

Sánchez-Lavega, A., Pérez-Hoyos, S., and Hueso, R. (2004). Clouds in planetary atmospheres: A useful application of the clausius-clapeyron equation. *American Journal of Physics*, 72(6):767–774.

Sánchez-Lavega, A., Pérez-Hoyos, S., Rojas, J. F., Hueso, R., and French, R. G. (2003). A strong decrease in saturn's equatorial jet at cloud level. *Nature*, 423(6940):623–625.

Sánchez-Lavega, A., Rojas, J. F., Acarreta, J. R., Lecacheux, J., Colas, F., and Sada, P. V. (1997). New observations and studies of saturn's long-lived north polar spot. *Icarus*, 128(2):322–334.

Sánchez-Lavega, A., Rojas, J. F., and Sada, P. V. (2000). Saturn's zonal winds at cloud level. *Icarus*, 147(2):405–420.

Sánchez-Lavega, A., Sromovsky, L., Showman, A., Genio, A. D., Young, R., Hueso, R., Melendo, E. G., Kaspi, Y., Orton, G. S., Barrado-Izagirre, N., Choi, D., and Barbara, J. (2017). Zonal jets in gas giants. In *Zonal Jets*. Cambridge University Press. (In press).

Sandel, B. R. and Broadfoot, A. L. (1981). Morphology of saturn's aurora. *Nature*, 292(5825):679–682.

Sanz-Requena, J. F., Pérez-Hoyos, S., Sánchez-Lavega, A., Antuñano, A., and Irwin, P. G. J. (2017). Haze and cloud structure of saturn's north pole and hexagon from cassini/iss imaging. (Under review in Icarus).

Sayanagi, K. M., Baines, K. H., Dyudina, U. A., Fletcher, L. N., Sánchez-Lavega, A., and West, R. A. (2016). Saturn's polar atmosphere. *ArXiv:1609.0962v2 [Astro-Ph.EP]*.

Sayanagi, K. M., Blalock, J. J., Dyudina, U. A., Ewald, S. P., and Ingersoll, A. P. (2017). Cassini ISS observation of saturn's north polar vortex and comparison to the south polar vortex. *Icarus*, 285:68–82.

Sayanagi, K. M., Dyudina, U. A., Ewald, S. P., Fischer, G., Ingersoll, A. P., Kurth, W. S., Muro, G. D., Porco, C. C., and West, R. A. (2013a). Dynamics of saturn's great storm of 2010-2011 from cassini ISS and RPWS. *Icarus*, 223(1):460–478.

Sayanagi, K. M., Dyudina, U. A., Ewald, S. P., Muro, G. D., and Ingersoll, A. P. (2014). Cassini ISS observation of saturn's string of pearls. *Icarus*, 229:170–180.

Sayanagi, K. M., Ewald, S. P., Dyudina, U. A., and Ingersoll, A. P. (2013b). Cassini iss analysis of saturns northern high-latitudes and the aftermath of the 2010 great storm. In *American Astronomical Society, DPS meeting*, volume #45, page #509.06.10.

Sayanagi, K. M., Morales-Juberías, R., and Ingersoll, A. P. (2010). Saturn's northern hemisphere ribbon: Simulations and comparison with the meandering gulf stream. *Journal of the Atmospheric Sciences*, 67(8):2658–2678.

Seidelmann, P. K., Archinal, B. A., A'hearn, M. F., Conrad, A., Consolmagno, G. J., Hestroffer, D., Hilton, J. L., Krasinsky, G. A., Neumann, G., Oberst, J., Stooke, P., Tedesco, E. F., Tholen, D. J., Thomas, P. C., and Williams, I. P. (2007). Report of the IAU/IAG working group on cartographic coordinates and rotational elements: 2006. *Celestial Mechanics and Dynamical Astronomy*, 98(3):155–180.

Showman, A. P., Gierasch, P. J., and Lian, Y. (2006). Deep zonal winds can result from shallow driving in a giant-planet atmosphere. *Icarus*, 182(2):513–526.

Smith, B. A., Soderblom, L., Batson, R., Bridges, P., Inge, J., Masursky, H., Shoemaker, E., Beebe, R., Boyce, J., Briggs, G., Bunker, A., Collins, S. A., Hansen,

C. J., Johnson, T. V., Mitchell, J. L., Terrile, R. J., Cook, A. F., Cuzzi, J., Pollack, J. B., Danielson, G. E., Ingersoll, A. P., Davies, M. E., Hunt, G. E., Morrison, D., Owen, T., Sagan, C., Veverka, J., Strom, R., and Suomi, V. E. (1982). A new look at the saturn system: The voyager 2 images. *Science*, 215(4532):504–537.

Smith, B. A., Soderblom, L., Beebe, R., Boyce, J., Briggs, G., Bunker, A., Collins, S. A., Hansen, C. J., Johnson, T. V., Mitchell, J. L., Terrile, R. J., Carr, M., Cook, A. F., Cuzzi, J., Pollack, J. B., Danielson, G. E., Iingersoll, A., Davies, M. E., Hunt, G. E., Masursky, H., Shoemaker, E., Morrison, D., Owen, T., Sagan, C., Veverka, J., Strom, R., and Suomi, V. E. (1981). Encounter with saturn: Voyager 1 imaging science results. *Science*, 212(4491):163–191.

Smith, E. J., Davis, L., Jones, D. E., Coleman, P. J., Colburn, D. S., Dyal, P., and Sonett, C. P. (1980a). Saturn's magnetic field and magnetosphere. *Science*, 207(4429):407–410.

Smith, E. J., Davis, L., Jones, D. E., Coleman, P. J., Colburn, D. S., Dyal, P., and Sonett, C. P. (1980b). Saturn's magnetosphere and its interaction with the solar wind. *Journal of Geophysical Research*, 85(A11):5655.

Snyder, J. P. (1987). *Map Projections - A Working Manual*. Books Express Publishing.

Srama, R., Ahrens, T. J., Altobelli, N., Auer, S., Bradley, J. G., Burton, M., Dikarev, V. V., Economou, T., Fechtig, H., Grlich, M., Grande, M., Graps, A., Grn, E., Havnes, O., Helfert, S., Horanyi, M., Igenbergs, E., Jessberger, E. K., Johnson, T. V., Kempf, S., Krivov, A. V., Krger, H., Mocker-Ahlreep, A., Moragas-Klostermeyer, G., Lamy, P., Landgraf, M., Linkert, D., Linkert, G., Lura, F., McDonnell, J. A. M., Mhlmann, D., Morfill, G. E., Mller, M., Roy, M., Schfer, G., Schlotzhauer, G., Schwehm, G. H., Spahn, F., Stbig, M., Svestka, J., Tschernjawski, V., Tuzzolino, A. J., Wsch, R., and Zook, H. A. (2004). The cassini cosmic dust analyzer. *Space Science Reviews*, 114(1-4):465–518.

Sromovsky, L., Baines, K., and Fry, P. (2013). Saturn's great storm of 2010-2011: Evidence for ammonia and water ices from analysis of VIMS spectra. *Icarus*, 226(1):402–418.

Sromovsky, L. A., Revercomb, H. E., Krauss, R. J., and Suomi, V. E. (1983). Voyager 2 observations of saturn's northern mid-latitude cloud features: Morphology, motions, and evolution. *Journal of Geophysical Research: Space Physics*, 88(A11):8650–8666.

Taylor, G. I. (1923). Experiments on the motion of solid bodies in rotating fluids. *Proceedings of the Royal Society A: Mathematical, Physical and Engineering Sciences*, 104(725):213–218.

Teanby, N. A., Irwin, P. G. J., de Kok, R., and Nixon, C. A. (2010). Seasonal Changes In titan's Polar Trace Gas Abundance Observed by Cassini. *The Astrophysical Journal*, 724(1):L84–L89.

Trammell, H. J., Li, L., Jiang, X., Smith, M., Hrst, S., and Vasavada, A. (2014). The global vortex analysis of jupiter and saturn based on cassini imaging science subsystem. *Icarus*, 242:122–129.

Vallis, G. K. (2006). *Atmospheric and Oceanic Fluid Dynamics*. Cambridge University Press.

Vasavada, A. R., Hrst, S. M., Kennedy, M. R., Ingersoll, A. P., Porco, C. C., Genio, A. D. D., and West, R. A. (2006). Cassini imaging of saturn: Southern hemisphere winds and vortices. *Journal of Geophysical Research*, 111(E5).

Vasavada, A. R. and Showman, A. P. (2005). Jovian atmospheric dynamics: an update after galileo and cassini. *Reports on Progress in Physics*, 68(8):1935–1996.

Waite, J. H., Lewis, W. S., Kasprzak, W. T., Anicich, V. G., Block, B. P., Cravens, T. E., Fletcher, G. G., Ip, W.-H., Luhmann, J. G., Mcnutt, R. L., Niemann, H. B., Parejko, J. K., Richards, J. E., Thorpe, R. L., Walter, E. M., and Yelle, R. V. (2004). The cassini ion and neutral mass spectrometer (INMS) investigation. *Space Science Reviews*, 114(1-4):113–231.

West, R., Knowles, B., Birath, E., Charnoz, S., Nino, D. D., Hedman, M., Helfenstein, P., McEwen, A., Perry, J., Porco, C., Salmon, J., Throop, H., and Wilson, D. (2010). In-flight calibration of the cassini imaging science sub-system cameras. *Planetary and Space Science*, 58(11):1475–1488.

West, R. A., Baines, K. H., Karkoschka, E., and Sánchez-Lavega, A. (2009). Clouds and aerosols in saturn's atmosphere. In *Saturn from Cassini-Huygens*, pages 161–179. Springer Nature.

Westphal, J. A., Baum, W. A., Ingersoll, A. P., Barnet, C. D., Jong, E. M. D., Danielson, G., and Caldwell, J. (1992). Hubble space telescope observations of the 1990 equatorial disturbance on saturn: Images, albedos, and limb darkening. *Icarus*, 100(2):485–498.

Young, D. T., Berthelier, J. J., Blanc, M., Burch, J. L., Coates, A. J., Goldstein, R., Grande, M., Hill, T. W., Johnson, R. E., Kelha, V., Mccomas, D. J., Sittler, E. C., Svenes, K. R., Szeg, K., Tanskanen, P., Ahola, K., Anderson, D., Bakshi, S., Baragiola, R. A., Barraclough, B. L., Black, R. K., Bolton, S., Booker, T., Bowman, R., Casey, P., Crary, F. J., Delapp, D., Dirks, G., Eaker, N., Funsten, H., Furman, J. D., Gosling, J. T., Hannula, H., Holmlund, C., Huomo, H., Illiano, J. M., Jensen, P., Johnson, M. A., Linder, D. R., Luntama, T., Maurice, S., Mccabe, K. P., Mursula, K., Narheim, B. T., Nordholt, J. E., Preece, A., Rudzki, J., Ruitberg, A., Smith, K., Szalai, S., Thomsen, M. F., Viherkanto, K., Vilppola, J., Vollmer, T., Wahl, T. E., West, M., Ylikorpi, T., and Zinsmeyer, C. (2004). Cassini plasma spectrometer investigation. *Space Science Reviews*, 114(1-4):1–112.